

Supporting Information

Tuning the Coordination Properties of Chiral Pseudopeptide Bis(2-picolyl)amine and Iminodiacetamide Ligands in Zn(II) and Cu(II) Complexes

Natalija Pantalon Juraj,^{a,#,*} Tana Tandarić,^{b,#} Vanja Tadić,^{c,#} Berislav Perić,^a Dominik Moreth,^d
Ulrich Schatzschneider,^d Anamaria Brozovic,^c Robert Vianello,^{b,*} Srećko I. Kirin^{a,*}

equal contribution

^aLaboratory for Solid State and Complex Compounds Chemistry, Ruđer Bošković Institute, Bijenička c. 54, HR-10000 Zagreb, Croatia

^bLaboratory for the Computational Design and Synthesis of Functional Materials, Ruđer Bošković Institute, Bijenička c. 54, HR-10000 Zagreb, Croatia

^cLaboratory for Cell Biology and Signaling, Ruđer Bošković Institute, Bijenička c. 54, HR-10000 Zagreb, Croatia

^dInstitut für Anorganische Chemie, Julius-Maximilians-Universität Würzburg, Am Hubland, D-97074 Würzburg, Germany

E-mail: Srecko.Kirin@irb.hr, Robert.Vianello@irb.hr, Natalija.Pantalon.Juraj@irb.hr

Contents

1	List of abbreviations.....	3
2	Synthesis	4
2.1	General procedure for the synthesis of Boc-protected precursors.....	4
2.2	Ligand synthesis	5
3	Structures of the synthesized ligands and truncated ligands used in calculations	6
4	NMR spectroscopy of free ligands	7
4.1	¹ H NMR spectra of free ligands in different solvents.....	7
4.2	Variable concentration ¹ H NMR spectra of free ligands	8
4.3	COSY NMR spectrum of b3A	11
4.4	¹ H- ¹ H NOESY spectra of free ligands	12
5	IR spectroscopy of free ligands	12
6	X-ray crystal structure determination.....	14
7	Cu(II) complexes.....	23
7.1	UV-Vis spectroscopy	23
8	NMR of Zn(II) complexes.....	32
8.1	¹ H NMR spectra with 0.5 and 1 added equivalents of Zn(CF ₃ SO ₃) ₂	32
8.2	¹³ C and 2D NMR spectra of ML complexes	34
8.3	¹ H NMR spectra of different L : M ratios at -40°C.....	37
8.4	Variable temperature ¹ H NMR spectra of complexes at a L : Zn(II) ratio of 2 L : 1.....	39
8.5	¹³ C APT NMR spectra of complexes at a L : Zn(II) ratio of 2 : 1	42

9	NMR and UV-Vis measurements in DMSO and water	44
10	Computational analysis.....	48
11	DNA cleavage	51
12	Characterization of the precursors and ligands.....	56
12.1	¹ H NMR spectra of precursors Boc2A-Boc3C:.....	56
12.2	¹ H and ¹³ C NMR spectra of ligands b1A-i3C:	59
12.3	ESI-MS spectra of ligands.....	72
13	References	74

1 List of abbreviations

Ala – Alanine

γ -Abu-OH – γ -Aminobutyric acid

HOBt – Hydroxybenzotriazole

TBTU – 2-(1H-Benzotriazole-1-yl)-1,1,3,3-tetramethylammonium tetrafluoroborate

DIPEA – *N,N*-Diisopropylethylamine

Phe – Phenylalanine

Boc – *tert*-Butyloxycarbonyl

VT NMR – variable temperature NMR

2 Synthesis

2.1 General procedure for the synthesis of Boc-protected precursors.

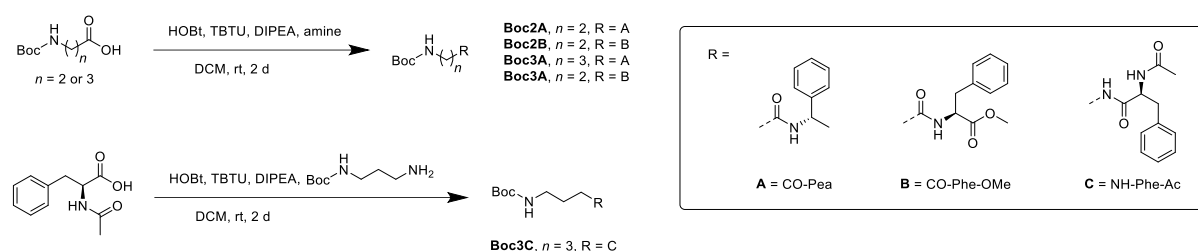


Figure S1. Synthesis of Boc-protected precursors **Boc2A-Boc3C**

A solution of the acid (1 equiv.), HOBt (1 equiv.), TBTU (1 equiv.) and DIPEA (4 equiv.) in dichloromethane (100 mL) was stirred at room temperature for 1 h. Then, the amine (1.0 or 1.5 equiv.) was added and stirring continued for 2 days. The reaction mixture was washed with aqueous sodium bicarbonate and brine, the organic layer dried over anhydrous sodium sulphate, filtered, and evaporated in a vacuum. The crude product was purified by automated flash chromatography (Teledyne Isco CombiFlash Rf) on pre-packed silica columns.

Boc2A. Boc- β -Ala-OH (700 mg, 3.7 mmol), (*S*)-(-)-1-phenylethylamine (706 μ L, 5.6 mmol), HOBt (500 mg, 3.7 mmol), TBTU (1188 mg, 3.7 mmol), DIPEA (2.5 mL, 14.8 mmol). Automated flash chromatography (silica gel) 50% \rightarrow 100% ethyl acetate in *n*-hexane, $R_f = 0.27$, 1:1 ethyl acetate: *n*-hexane. Yield: 70% (754 mg, 2.6 mmol), white powder. $^1\text{H NMR}$ (300.13 MHz, CDCl_3) δ 7.38 – 7.26 (m, 5H, Ph), 5.94 (s, 1H, NH), 5.16 – 5.07 (m, 2H, CH, NH), 3.44 – 3.36 (m, 2H, CH_2), 2.48 – 2.34 (m, 2H, CH_2), 1.48 (d, $J = 6.9$ Hz, 3H, CH_3), 1.42 (s, 9H, Boc).

Boc2B. Boc- β -Ala-OH (600 mg, 3.2 mmol), L-Phe-OMe-HCl (1026 mg, 4.8 mmol), HOBt (428 mg, 3.2 mmol), TBTU (1018 mg, 3.2 mmol), DIPEA (2.1 mL, 12.7 mmol). Automated flash chromatography (silica gel) 20% \rightarrow 60% ethyl acetate in *n*-hexane, $R_f = 0.45$, 1:1 ethyl acetate: *n*-hexane. Yield: 76% (841 mg, 2.4 mmol), white powder. $^1\text{H NMR}$ (300.13 MHz, CDCl_3) δ 7.32 – 7.26 (m, 3H, Ph), 7.14 – 7.04 (m, 2H, Ph), 5.97 (s, 1H, NH), 5.07 (s, 1H, NH), 4.87 (m, 1H, CH), 3.74 (s, 3H, CH_3), 3.44 – 3.30 (m, 2H, CH_2), 3.20 – 3.03 (m, 2H, $\text{CH}_2(\text{Ph})$), 2.43 – 2.31 (m, 2H, CH_2), 1.43 (s, 9H, Boc).

Boc3A. Boc- γ -Abu-OH (500 mg, 2.5 mmol), (*S*)-(-)-1-phenylethylamine (470 μ L, 3.7 mmol), HOBt (332 mg, 2.5 mmol), TBTU (790 mg, 2.5 mmol), DIPEA (1.6 mL, 9.8 mmol). Automated flash chromatography (silica gel) 30% \rightarrow 70% ethyl acetate in *n*-hexane, $R_f = 0.17$, 1:1 ethyl acetate: *n*-hexane. Yield: 94% (705 mg, 2.3 mmol), white solid. $^1\text{H NMR}$ (600.13 MHz, CDCl_3) δ 7.39 – 7.30 (m, 3H, Ph), 6.40 (s, 1H, NH), 5.16 – 5.08 (m, 1H, CH), 4.72 (s, 1H, NH), 3.23 – 3.10 (m, 2H, CH_2), 2.21 (t, $J = 7.0$ Hz, 2H, CH_2), 1.88 – 1.73 (m, 2H, CH_2), 1.49 (d, $J = 6.9$ Hz, 3H, CH_3), 1.44 (s, 9H, Boc).

Boc3B. Boc- γ -Abu-OH (500 mg, 2.5 mmol), L-Phe-OMe-HCl (796 mg, 3.7 mmol), HOBt (332 mg, 2.5 mmol), TBTU (790 mg, 2.5 mmol), DIPEA (1.6 mL, 9.8 mmol). Automated flash chromatography (silica gel) 20% \rightarrow 60% ethyl acetate in *n*-hexane, $R_f = 0.28$, 1:1 ethyl acetate: *n*-hexane. Yield: 96% (858 mg, 2.4 mmol), white solid. $^1\text{H NMR}$ (600.13 MHz, CDCl_3) δ 7.33 – 7.27 (m, 2H, Ph), 7.26 – 7.22 (m, 1H, Ph), 7.21 – 7.17 (m, 1H, Ph), 7.13 (d, $J = 7.0$ Hz, 1H, Ph), 6.41 (s, 1H, NH), 4.90 – 4.82 (m, 1H, CH), 4.69 (s, 1H, NH), 3.73 (m, 3H, CH_3), 3.24 – 3.13 (m, 2H, CH_2), 3.13 – 3.03 (m, 2H, CH_2), 2.25 – 2.14 (m, 2H, CH_2), 1.81 – 1.71 (m, 2H, CH_2), 1.44 (s, 9H, Boc).

Boc3C. *N*-Acetyl-L-phenylalanine (595 mg, 2.9 mmol), *N*-Boc-1,3-propanediamine (501 μ L, 2.9 mmol), HOBt (388 mg, 2.9 mmol), TBTU (922 mg, 2.9 mmol), DIPEA (1.9 mL, 11.5 mmol). Automated flash

chromatography (silica gel) 0% → 5% methanol in dichloromethane, $R_f = 0.24$, 5% methanol in dichloromethane. Yield: 87% (903 mg, 2.5 mmol), white solid. $^1\text{H NMR}$ (300.13 MHz, CDCl_3) δ 7.35 – 7.27 (m, 2H, Ph), 7.24 – 7.17 (m, 3H, Ph), 6.49 (s, 1H, NH), 6.13 (d, $J = 7.2$ Hz, 1H, NH), 4.73 (s, 1H, NH), 4.69 – 4.56 (m, 1H, CH), 3.23 – 3.09 (m, 3H, CH_2), 3.04 – 2.89 (m, 3H, CH_2), 2.00 (s, 3H, CH_3), 1.49 – 1.44 (m, 2H, CH_2), 1.42 (s, 9H, Boc).

2.2 Ligand synthesis

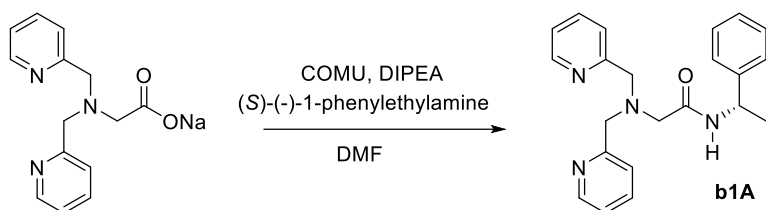


Figure S2. Synthesis of ligand **b1A**

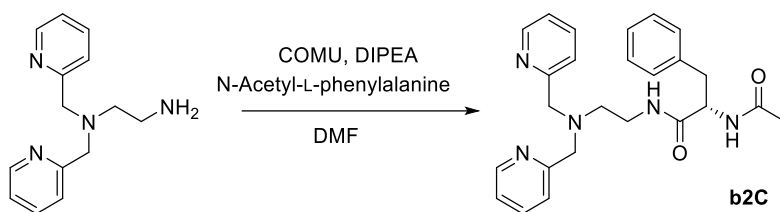


Figure S3. Synthesis of ligand **b2C**

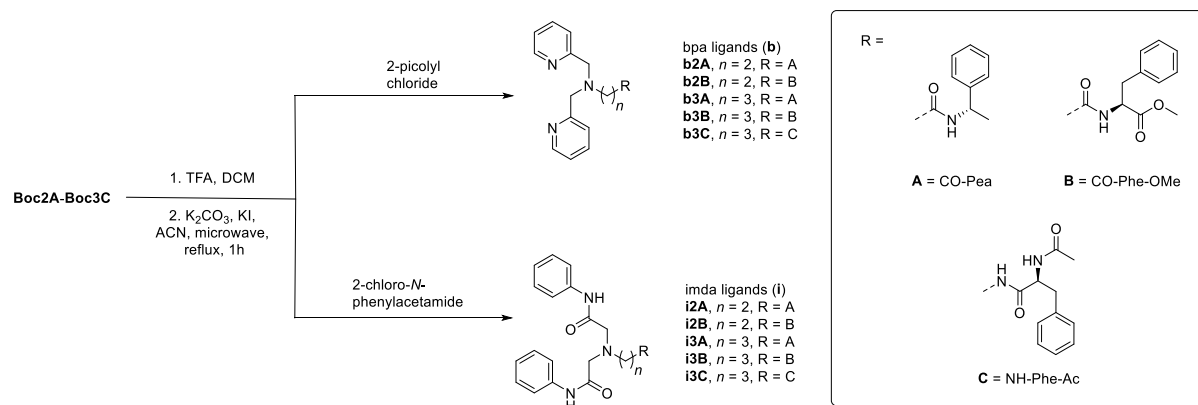


Figure S4. Synthesis of ligands **b2A-i3C**

3 Structures of the synthesized ligands and truncated ligands used in calculations

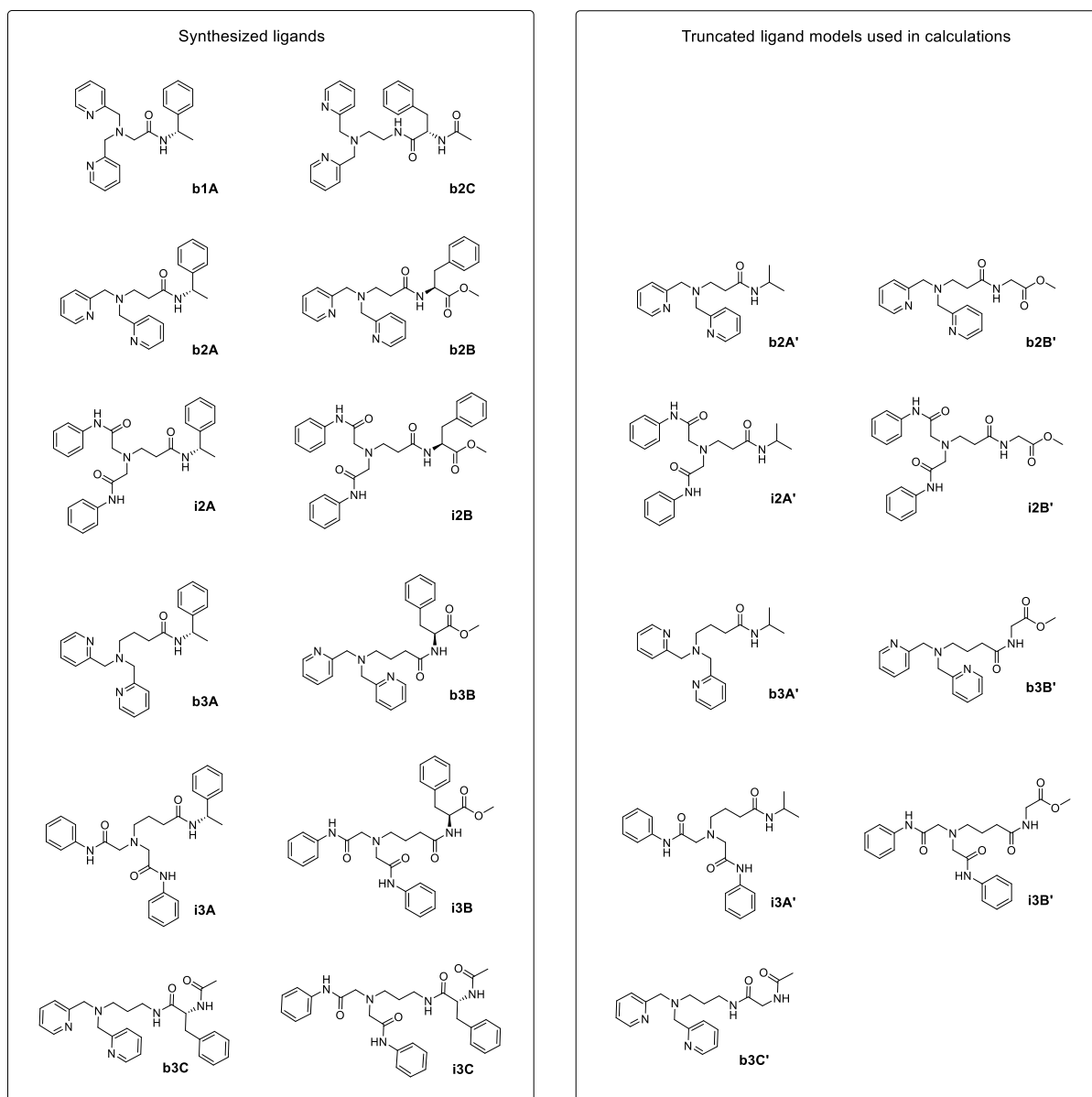


Figure S5. Structures of twelve synthesized ligands and nine truncated ligand models used in calculations.

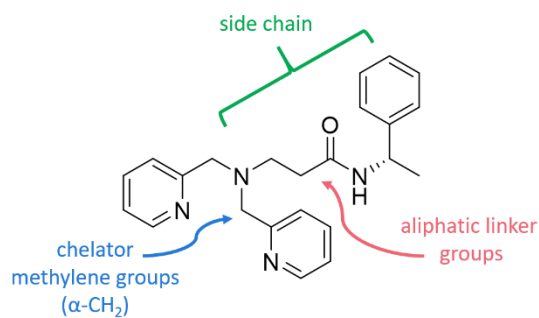


Figure S6. Nomenclature for the ligand structure used throughout the text.

4 NMR spectroscopy of free ligands

4.1 ^1H NMR spectra of free ligands in different solvents

The extent of hydrogen bonding can be inferred from the comparison of amide proton ^1H NMR chemical shifts in DMSO and chloroform using the hydrogen bond acidity value, A (Table S1).¹ Large A values indicate that the side chain amide protons of **i2A** and **i3A** are not significantly hydrogen-bonded in chloroform. A weak hydrogen bond is likely in **b3A**, as the amide proton is shifted 0.5 ppm more downfield than in **i3A** with an isostructural side chain. Hydrogen bonding of the side chain amide is less likely in the imda derivatives, as the chelator amides compete for hydrogen bonding by forming 5-membered rings. In **b1A** and **b2A** the amide peak is shifted downfield in chloroform compared to DMSO due to strong hydrogen bonding in chloroform.

Table S1. ^1H NMR peaks of the side chain amide protons in different solvents at 6 - 8 mM concentrations.

Ligand	$\delta(\text{DMSO})$ /ppm	$\delta(\text{CDCl}_3)$ /ppm	$\Delta\delta^a$	A^b	$\delta(\text{CD}_3\text{CN})$ /ppm
b1A	8.95	9.24	-0.29	-0.03	9.12
b2A	8.39	8.51	-0.12	-0.01	7.93
b3A	8.18	6.43	1.75	0.24	6.83
i2A	8.49	5.92	2.57	0.35	7.17 ^c
i3A	8.22	5.96	2.26	0.31	6.93
lit. ^d	7.73	5.42	2.31	0.31	6.23

^a $\Delta\delta = \delta(\text{DMSO}) - \delta(\text{CDCl}_3)$, ^b $A = 0.0065 + 0.133\Delta\delta$, ^cthe side chain NH peak of **i2A** in CD_3CN is overlapped with the phenyl peaks, ^dlit. = N-methylacetamide as an example of a non-hydrogen bonded amide from ref.^{1,2}

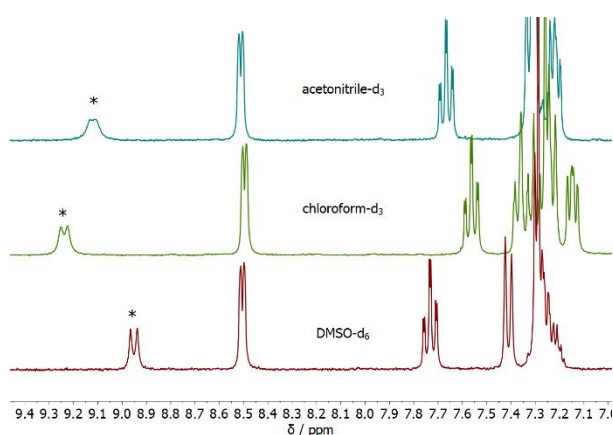


Figure S7. ^1H NMR spectra (aromatic region) of ligand **b1A** in $\text{DMSO}-d_6$ (7.9 mM), $\text{chloroform}-d_3$ (7.9 mM), and $\text{acetonitrile}-d_3$ (7.7 mM). Side chain amide NH protons (*) are accented.

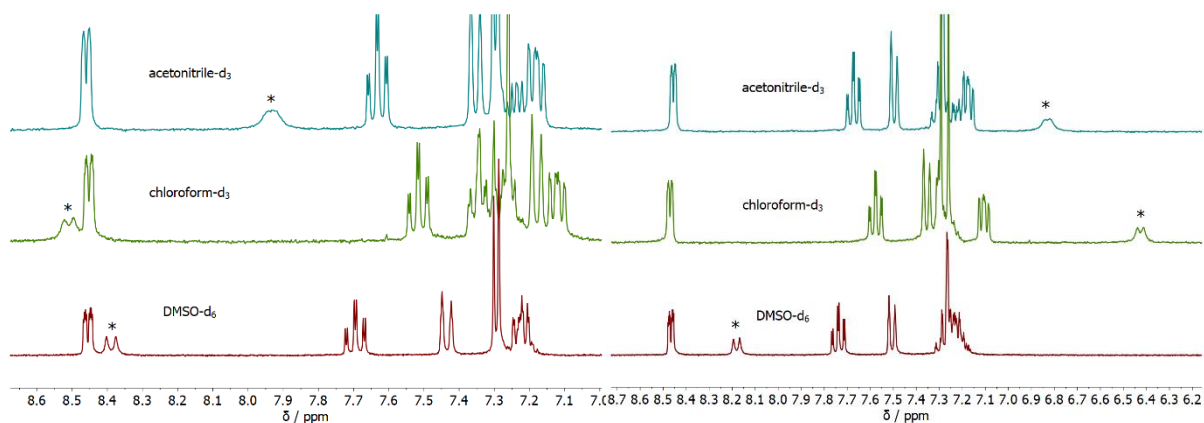


Figure S8. ¹H NMR spectra (aromatic region) of ligand **b2A** (left) in DMSO-*d*₆ (5.8 mM), chloroform-*d*₃ (6.1 mM), and acetonitrile-*d*₃ (6.1 mM), and ligand **b3A** (right) in DMSO-*d*₆ (7.0 mM), chloroform-*d*₃ (6.8 mM), and acetonitrile-*d*₃ (7.0 mM). Side chain amide NH protons (*) are accented.

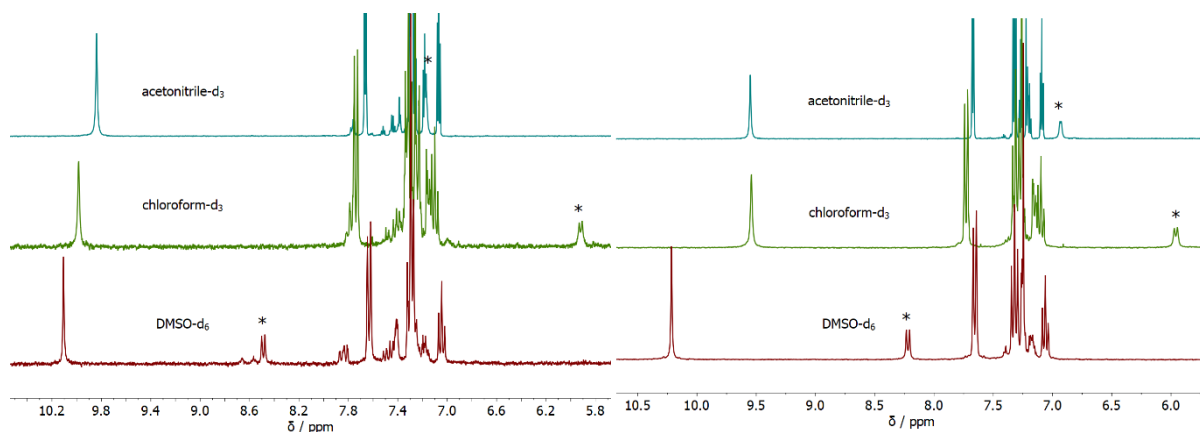


Figure S9. ¹H NMR spectra (aromatic region) of ligand **i2A** (left) in DMSO-*d*₆ (6.0 mM), chloroform-*d*₃ (6.0 mM), and acetonitrile-*d*₃ (6.2 mM). The NH peak in acetonitrile solution is overlapping with the aromatic signals. ¹H NMR spectra (aromatic region) of ligand **i3A** (right) in DMSO-*d*₆ (8.0 mM), chloroform-*d*₃ (7.7 mM), and acetonitrile-*d*₃ (8.0 mM). Side chain amide NH protons (*) are accented.

4.2 Variable concentration ¹H NMR spectra of free ligands

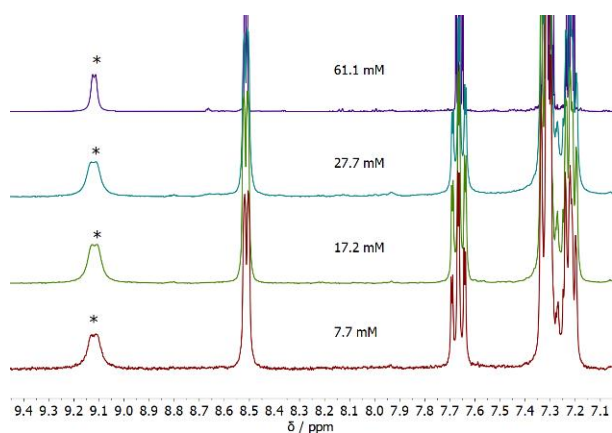


Figure S10. Variable concentration ¹H NMR spectra (aromatic region) of ligand **b1A** in acetonitrile-*d*₃. Side chain amide NH protons (*) are accented.

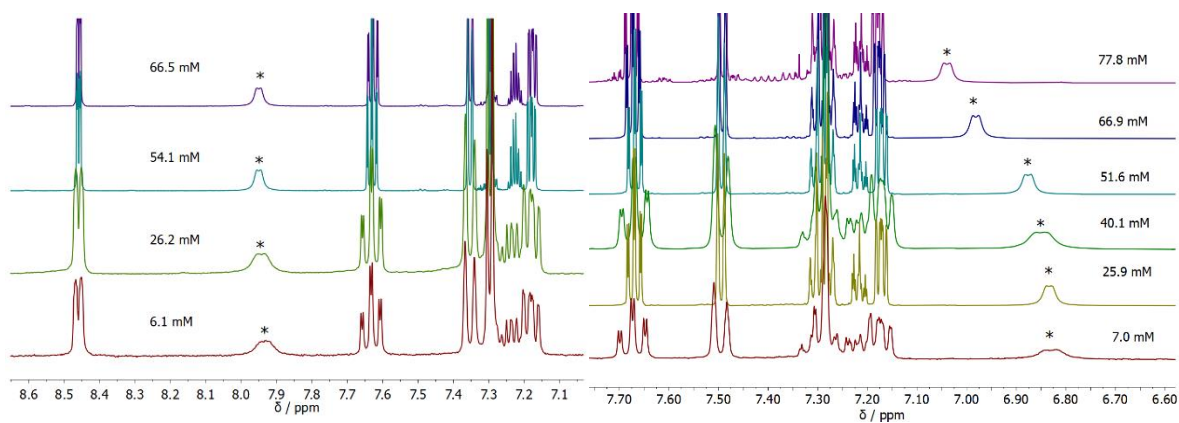


Figure S11. Variable concentration ^1H NMR spectra (aromatic region) of ligand **b2A** (left) and ligand **b3A** (right) in acetonitrile- d_3 . Side chain amide NH protons (*) are accented.

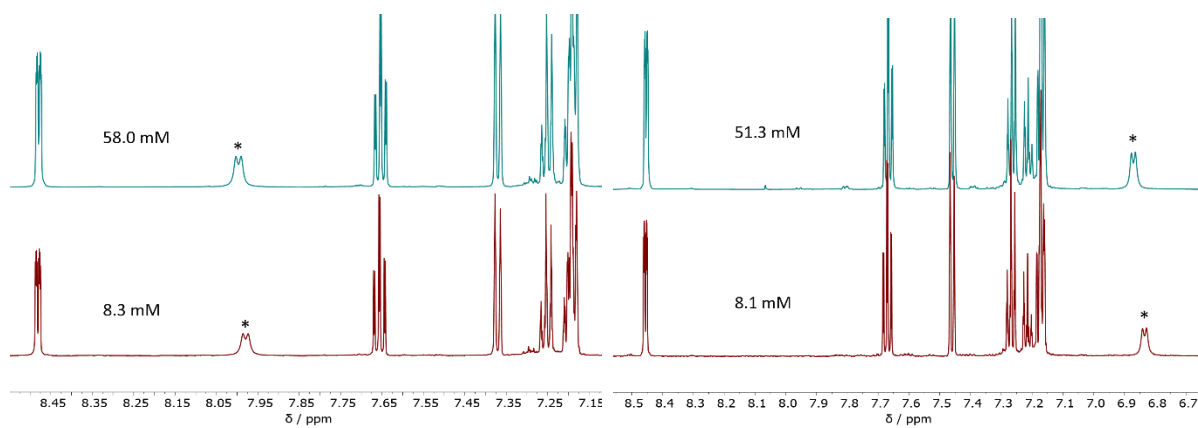


Figure S12. Variable concentration ^1H NMR spectra (aromatic region) of ligand **b2B** (left) and ligand **b3B** (right) in acetonitrile- d_3 . Side chain amide NH protons (*) are accented.

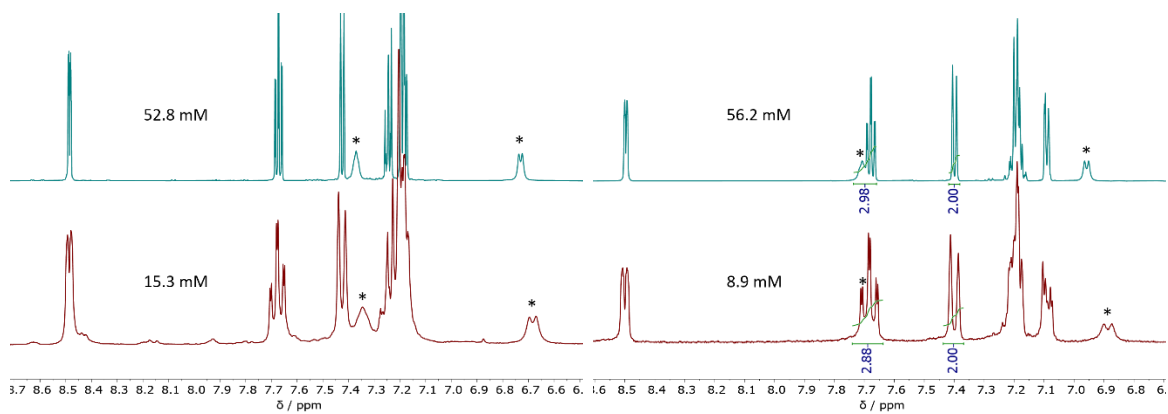


Figure S13. Variable concentration ^1H NMR spectra (aromatic region) of ligand **b2C** (left) and ligand **b3C** (right) in acetonitrile- d_3 . Side chain amide NH protons (*) are accented.

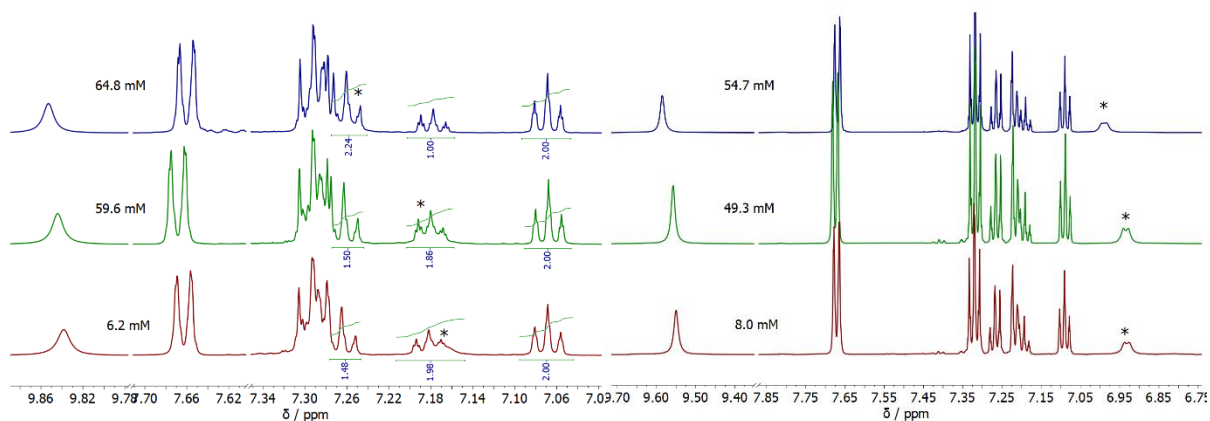


Figure S14. Variable concentration ^1H NMR spectra (aromatic region, the NH peak is overlapping with the aromatic signals) of ligand **i2A** (left) and ligand **i3A** (right) in acetonitrile- d_3 . Side chain amide NH protons (*) are accented.

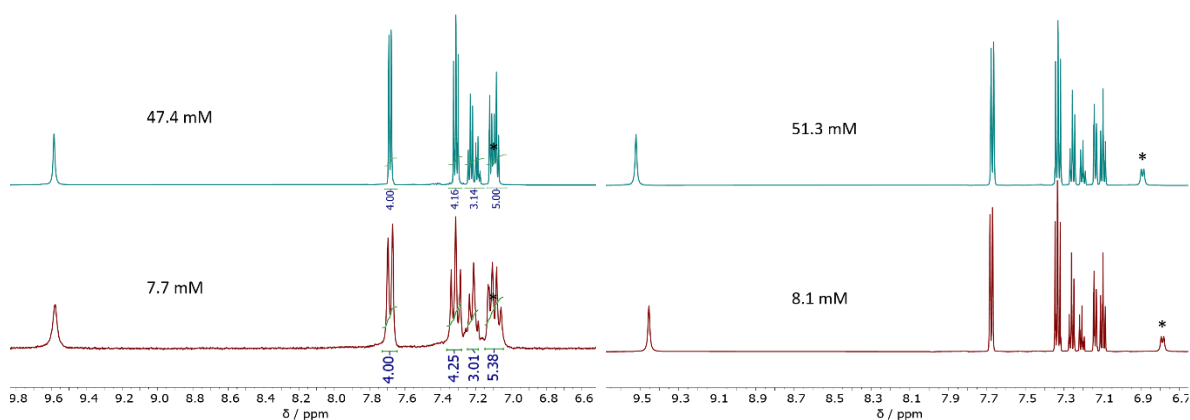


Figure S15. Variable concentration ^1H NMR spectra (aromatic region, the NH peak is overlapping with the aromatic signals) of ligand **i2B** (left) and ligand **i3B** (right) in acetonitrile- d_3 . Side chain amide NH protons (*) are accented.

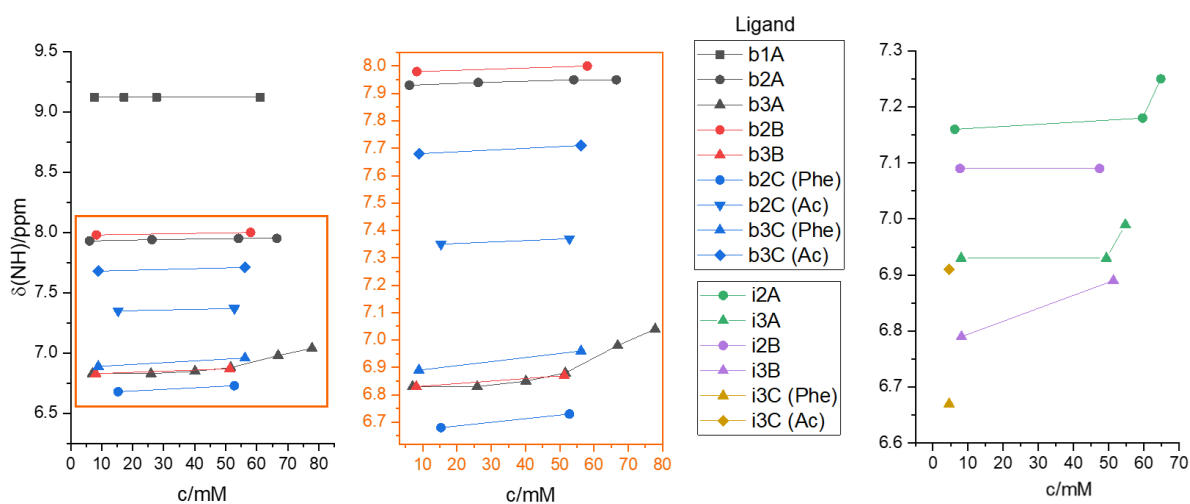


Figure S16. Concentration dependence of side chain NH peak shifts in acetonitrile- d_3 . ^1H NMR of Ligand **i3C** was measured only at a lower concentration due to poor solubility.

4.3 COSY NMR spectrum of b3A

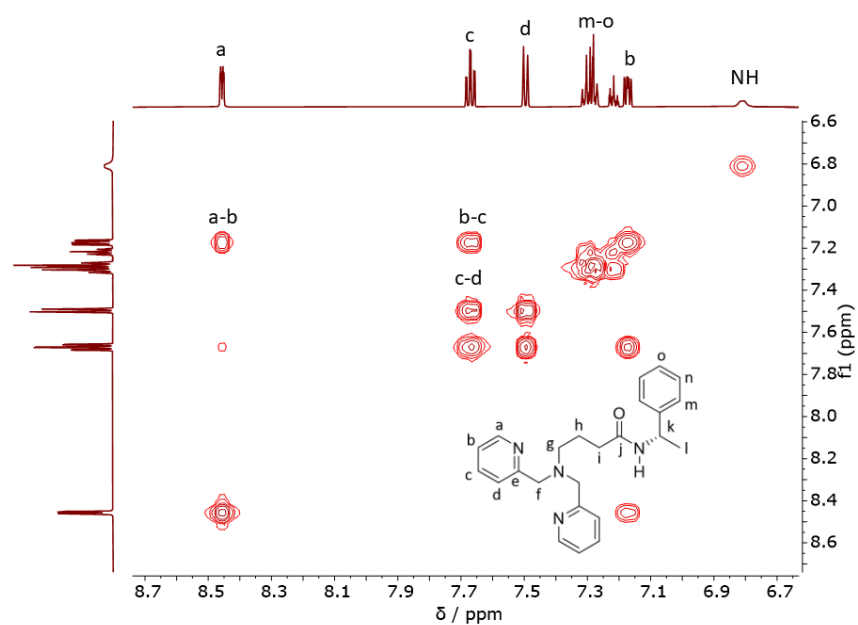


Figure S17. COSY spectrum of ligand **b3A** (7.4 mM, aromatic region) in acetonitrile-*d*₃.

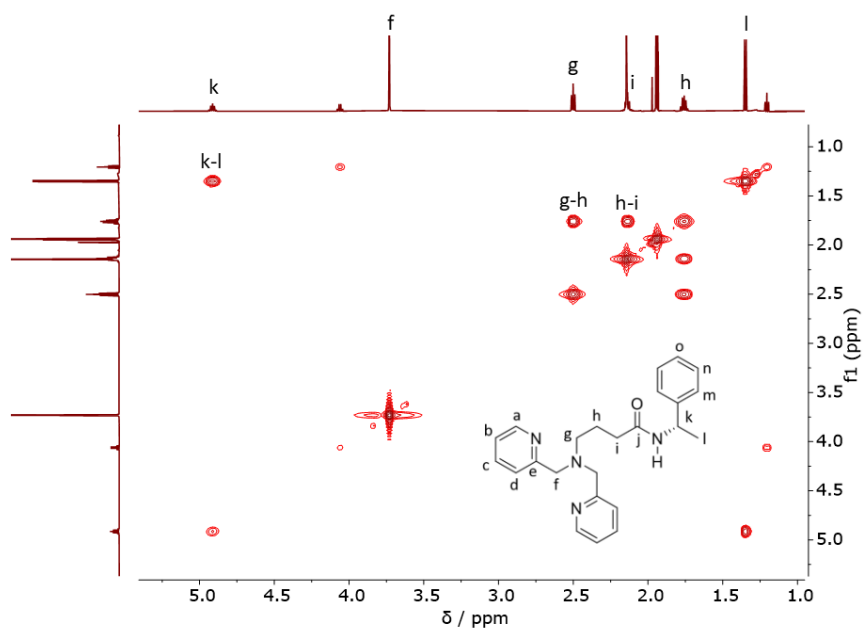


Figure S18. COSY spectrum of ligand **b3A** (7.4 mM, aliphatic region) in acetonitrile-*d*₃.

4.4 ^1H - ^1H NOESY spectra of free ligands

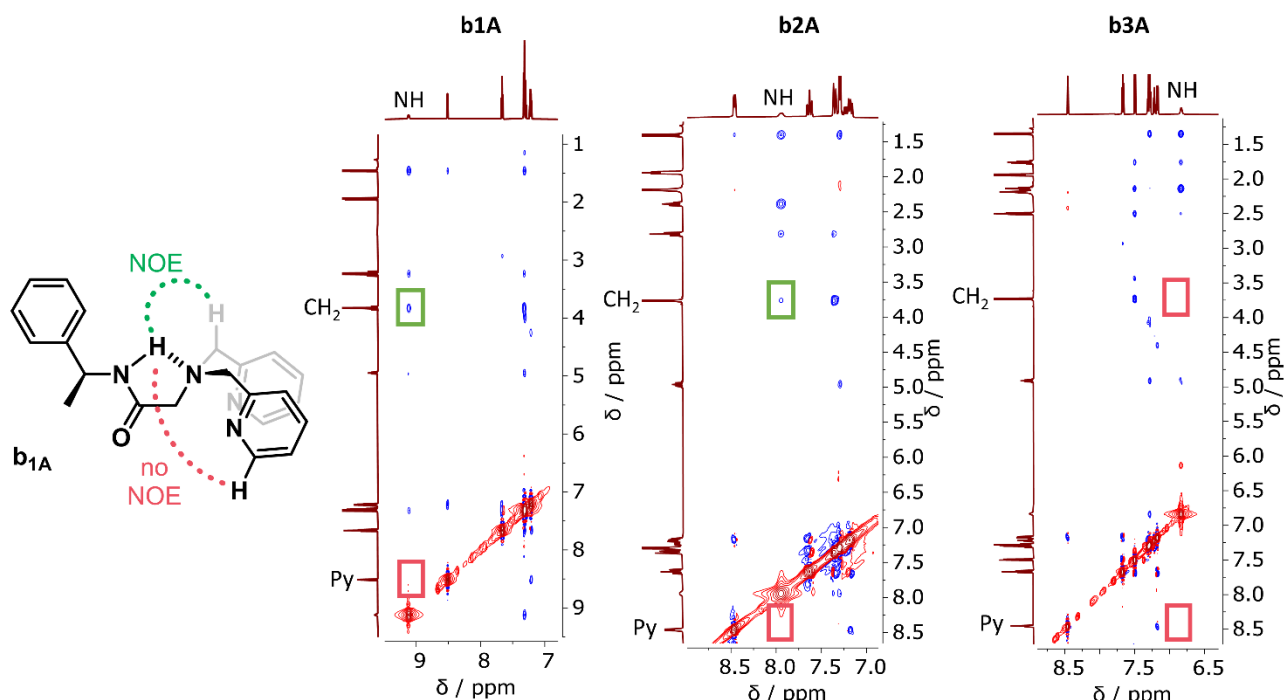


Figure S19. NOESY interactions of side chain amide NH peaks in ligands **b1A**, **b2A**, and **b3A**.

5 IR spectroscopy of free ligands

IR spectra in dichloromethane (Figure S16) show a significantly higher ratio of bonded amides with N-H vibrations below 3400 cm^{-1} for **b2A** than **b3A**, in agreement with the strong and weak hydrogen bonds observed in NMR for **b2A** and **b3A**, respectively.³ The situation is different for **i2A** and **i3A**, where the aliphatic linker length had no effect on the ratio of free and bonded amides, indicating that the side chain amides in **i2A** and **i3A** are not significantly hydrogen bonded due to competition with the chelator amides. Variable concentration IR spectra (Figures S17-S18) show no change for **b2A**, suggesting intramolecular hydrogen bonding, while **b3A**, **i2A** and **i3A** with amide groups available for aggregation show an increase of the bonded N-H peak at higher concentrations.

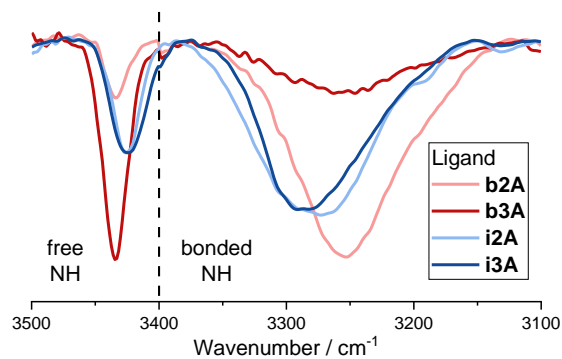


Figure S20. IR spectra in dichloromethane solution at $c \approx 10\text{ mM}$

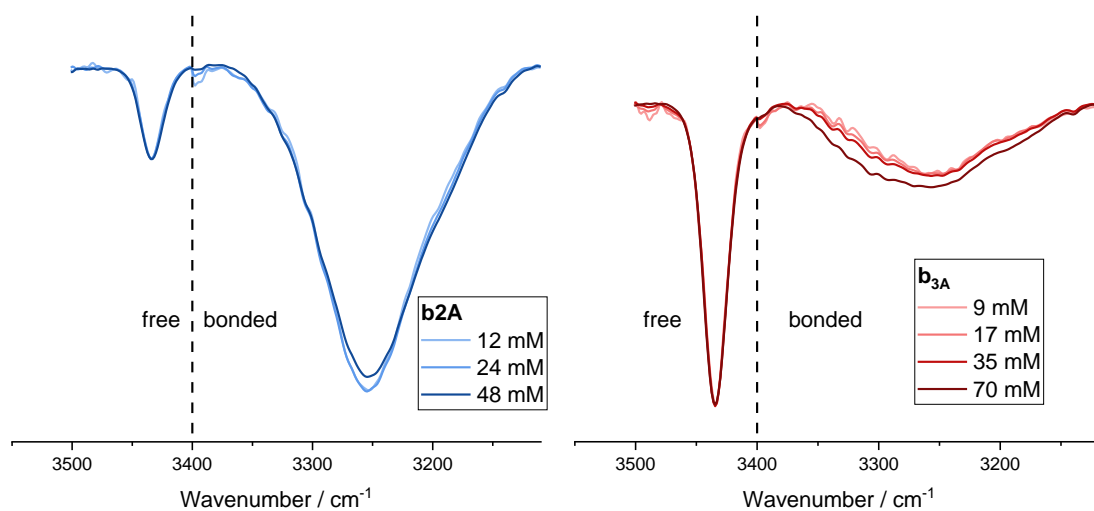


Figure S21. Variable concentration IR spectra of **b2A** (left) and of **b3A** (right) corrected for concentration in dichloromethane.

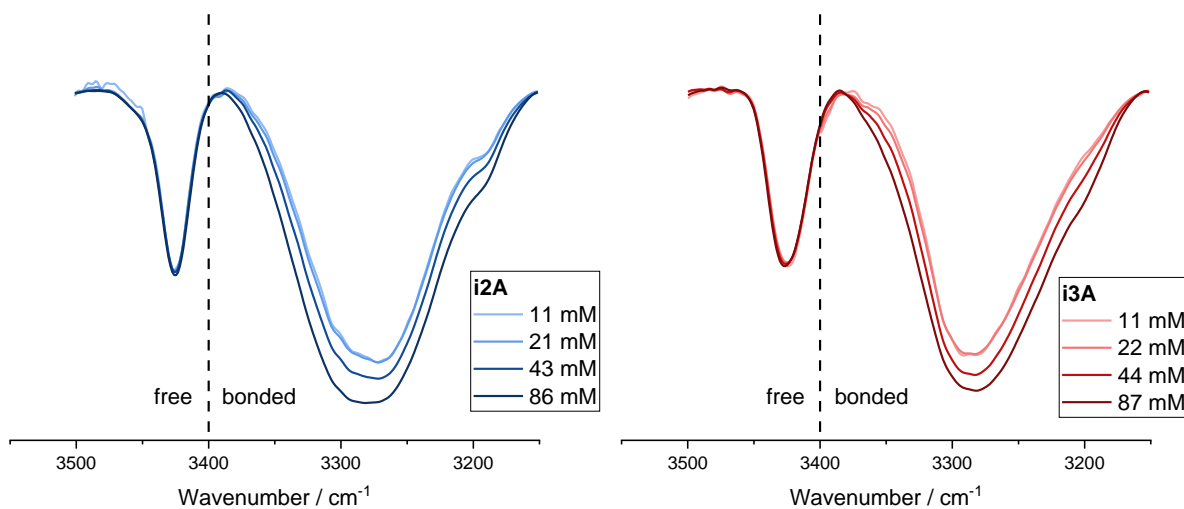
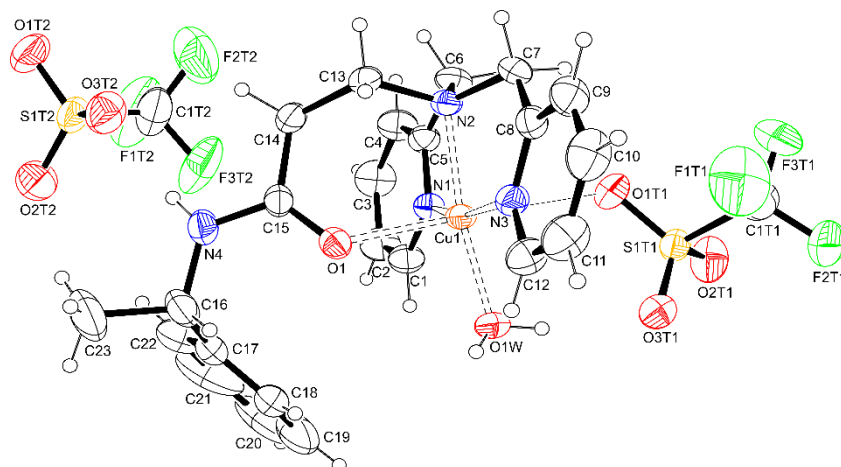
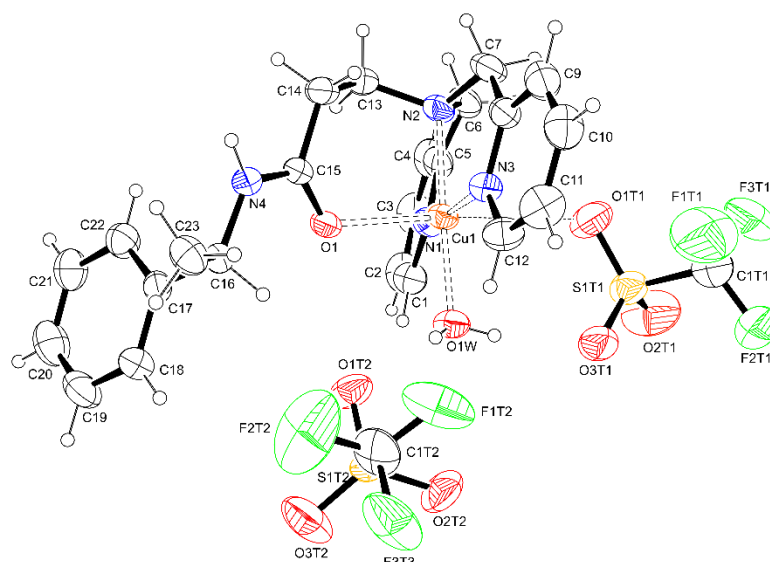


Figure S22. Variable concentration IR spectra of **i2A** (left) and of **i3A** (right) corrected for concentration in dichloromethane.

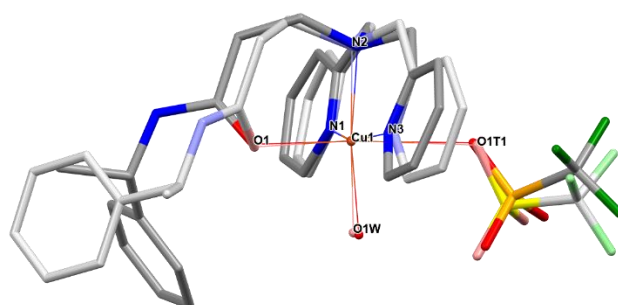
6 X-ray crystal structure determination



(a)



(b)



(c)

Figure S23. Molecular structures of **b2A-Cu-o** (a) and **b2A-Cu-t** (b) with thermal ellipsoids drawn at the 30% probability level. (c) Molecular overlap representation showing differences in conformation of $[\text{Cu}(\text{b2A})(\text{H}_2\text{O})(\text{CF}_3\text{SO}_3)]^+$ cations in orthorhombic (dark colours) and triclinic forms (light colours).

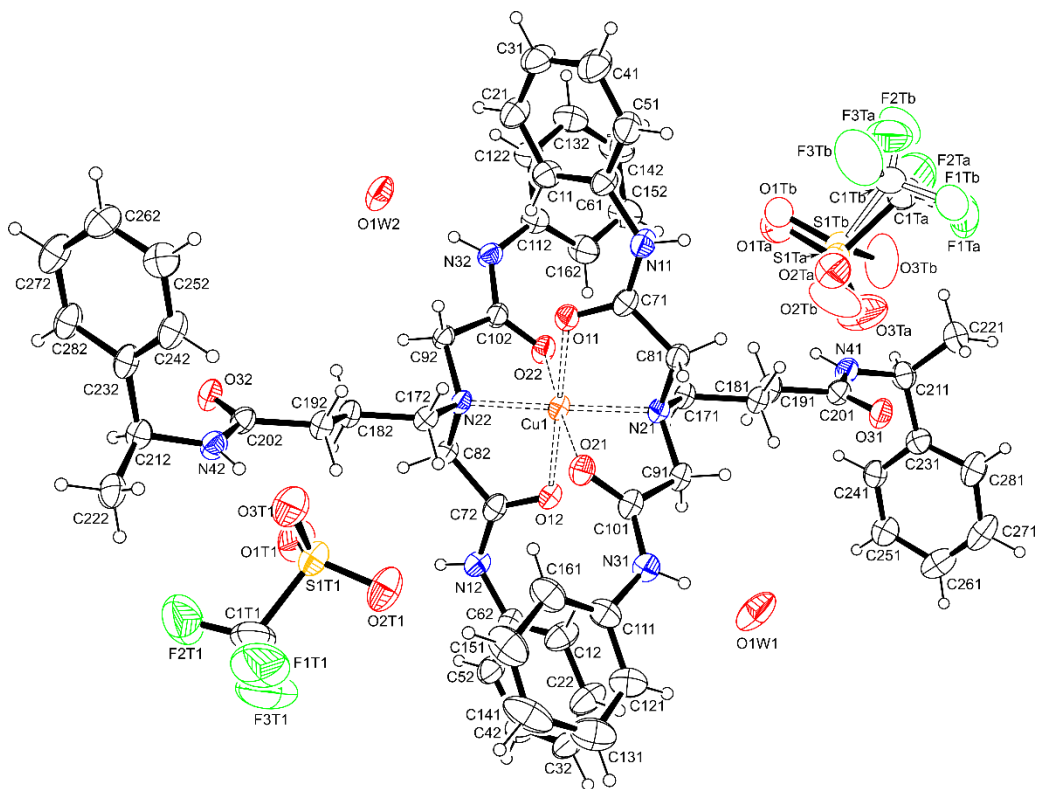


Figure S24. Molecular structure of **i3A-Cu** with thermal ellipsoids drawn at the 30% probability level. Atoms from the disordered triflate anion with site occupancies lower than 0.5 are shown with empty ellipsoids (disorder part b).

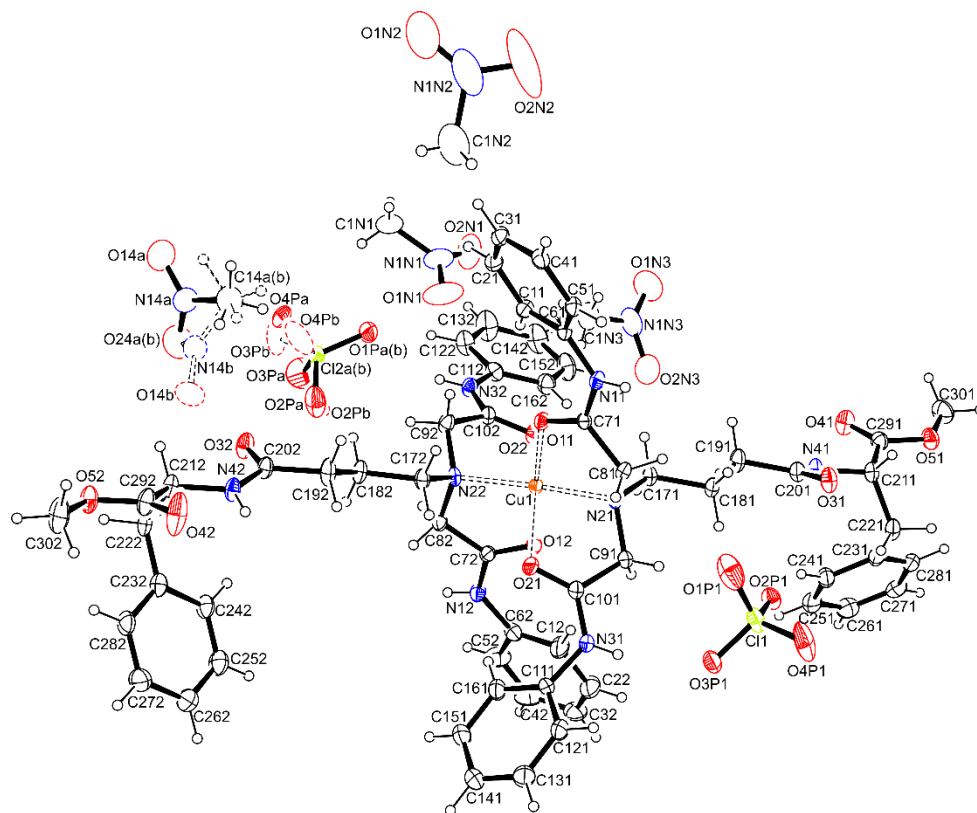


Figure S25. Molecular structure of **i3B-Cu** with thermal ellipsoids drawn at the 30% probability level. Atoms from the disordered perchlorate anion and a nitromethane solvent molecule with site occupancies lower than 0.5 are shown with dashed empty ellipsoids (disorder parts b), other atoms from nitromethane solvent molecules are shown as empty ellipsoids.

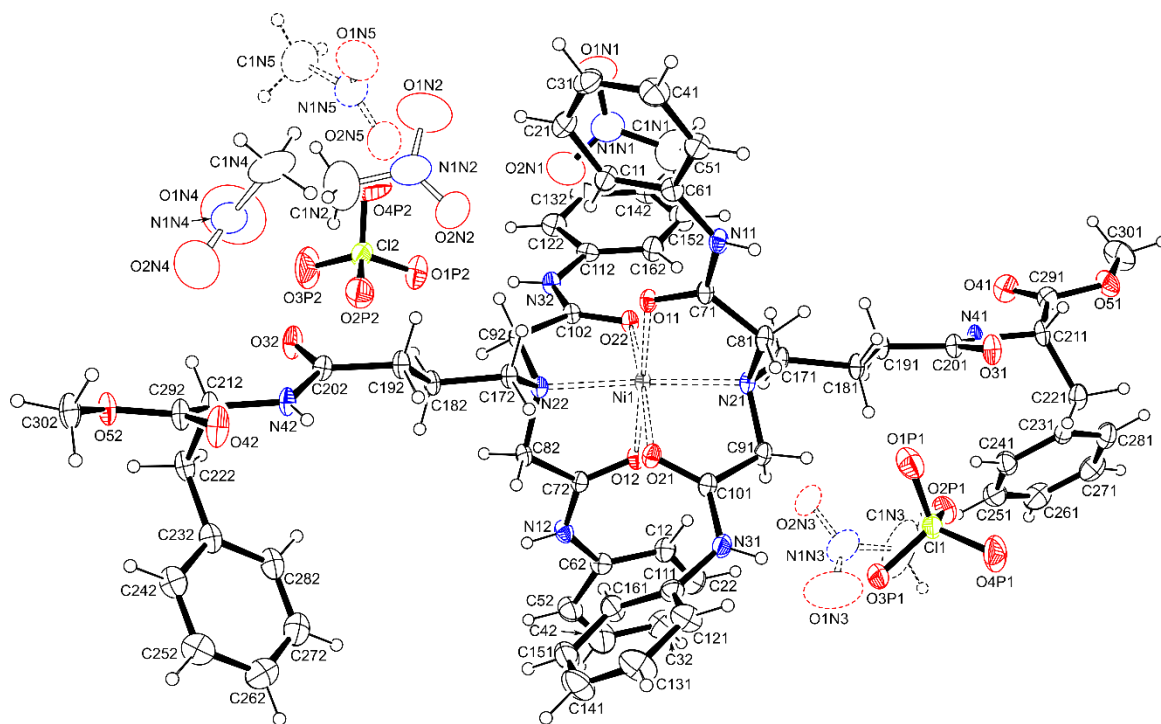


Figure S26. Molecular structure of **i3B-Ni** with thermal ellipsoids drawn at the 30% probability level. Atoms from the nitromethane solvent molecule with site occupancies lower than 0.5 are shown with dashed empty ellipsoids, other atoms from nitromethane solvent molecules are shown as empty ellipsoids.

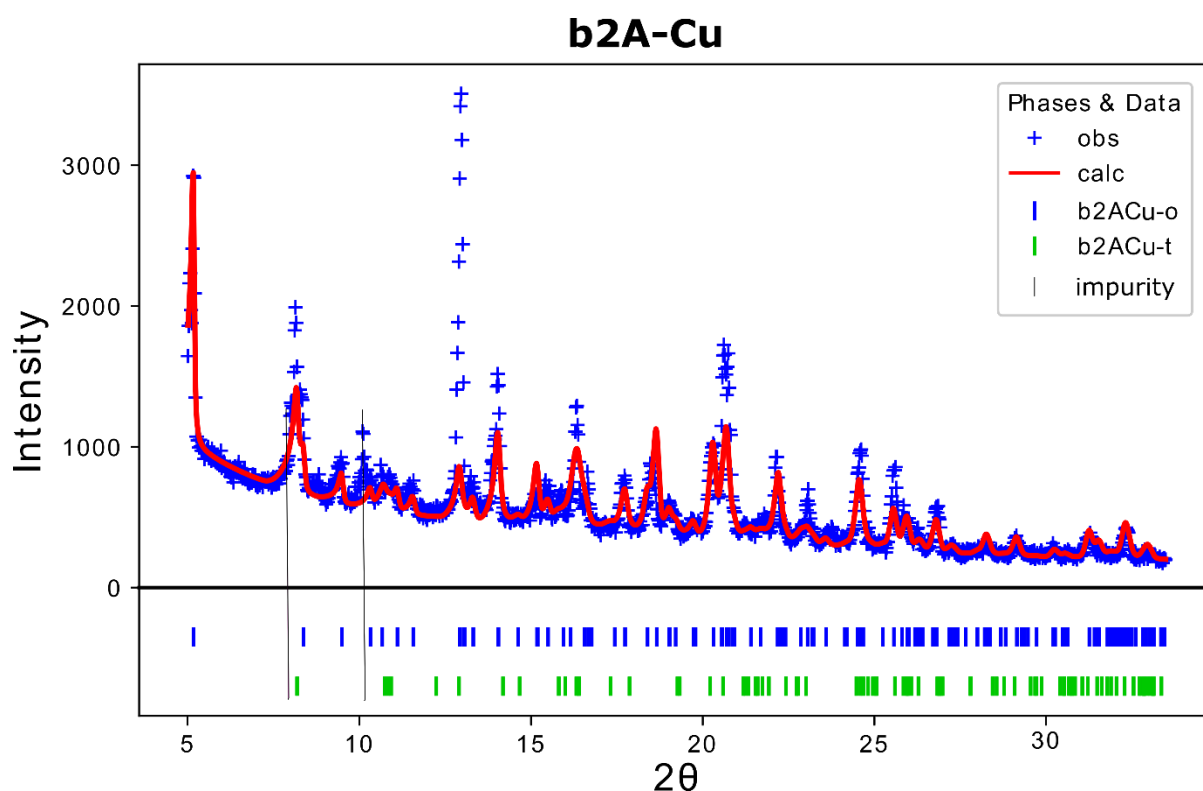


Figure S27. X-ray powder diffractogram of **b2A-Cu**. Red curve is the calculated diffractogram based on Rietveld refinement considering both phases obtained from the single crystal X-ray diffraction (**b2A-Cu-o** and **b2A-Cu-t**). The majority of observed peaks agreed with **b2A-Cu-o** or **b2A-Cu-t** phases, additional peaks (thin black lines) show contribution of an additional unknown crystalline phase in the sample. Refined values for phase fractions of **b2A-Cu-o** and **b2A-Cu-t** phases were 0.47(3) and 0.53(3), respectively ($R_{wp} = 19.41\%$). Refinement was performed with the GSAS-II program.⁴

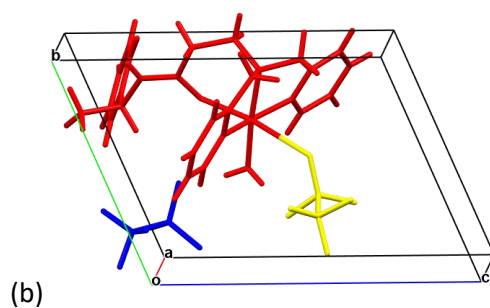
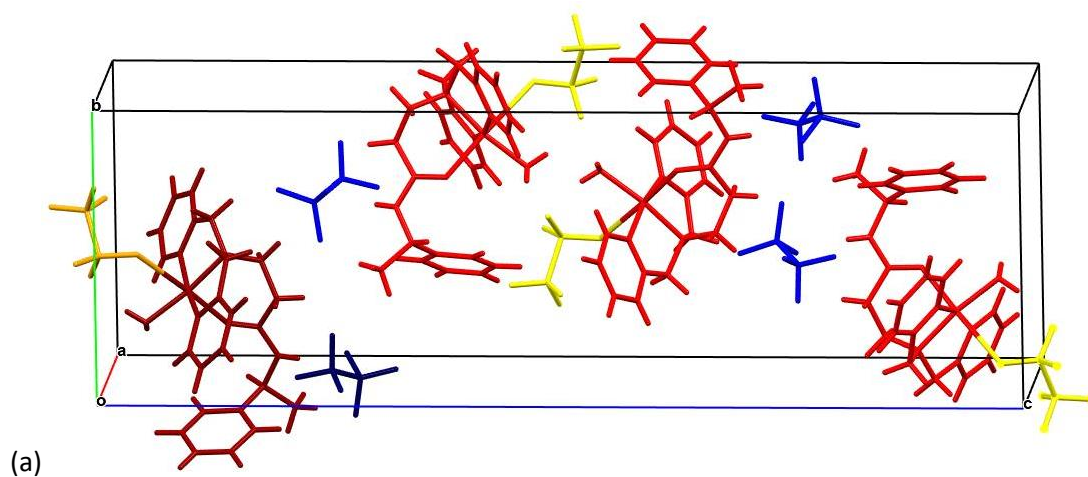


Figure S28. Crystal packing diagram of **b2A-Cu-o** (a) and **b2A-Cu-t** (b). Complex cations are shown in red, coordinated triflate anions in yellow, and free triflate anions in blue. Contents of the original asymmetric unit of **b2A-Cu-o** are shown in dark red, yellow, and blue.

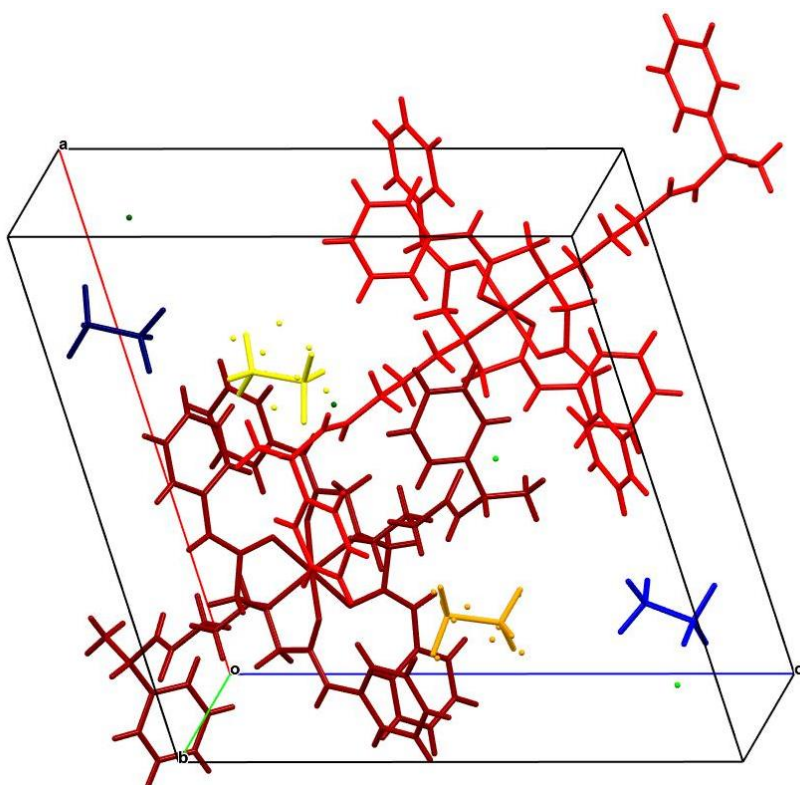


Figure S29. Crystal packing diagram of **i3A-Cu**. Complex cations are shown in red, disordered triflate anions in yellow, regular triflate anions in blue and positions of oxygen atoms from solvent water are coloured green. Contents of the original asymmetric unit are shown in dark red, yellow, blue, and green.

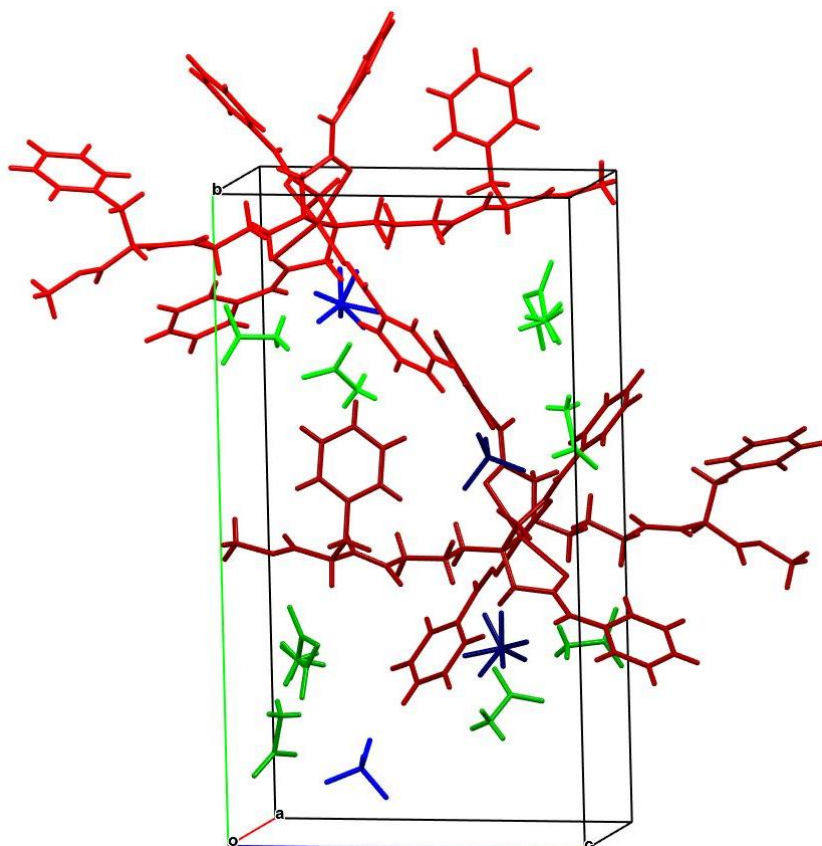


Figure S30. Crystal packing diagram of **i3B-Cu**. Complex cations are shown in red, perchlorate anions in blue and, nitromethane solvent molecules in green. Contents of the original asymmetric unit are shown in dark red, blue, and green.

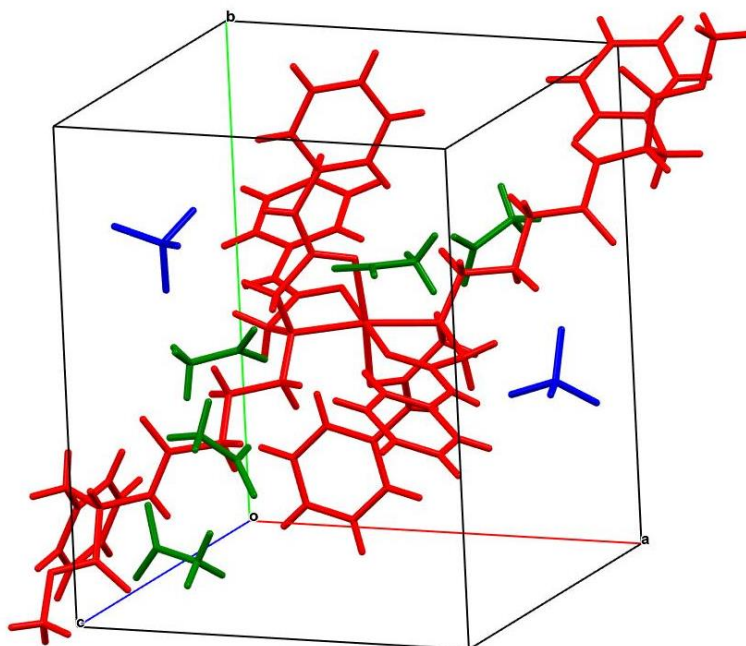


Figure S31. Crystal packing diagram of **i3B-Ni**. Complex cations are shown in red, perchlorate anions in blue, and nitromethane solvent molecules in green.

Table S2. Experimental data for the X-ray diffraction studies.

Compound	b2A-Cu-o	b2A-Cu-t	i3A-Cu	i3B-Cu	i3B-Ni
Formula	C ₂₅ H ₂₈ CuF ₆ N ₄ O ₈ S ₂	C ₂₅ H ₂₈ CuF ₆ N ₄ O ₈ S ₂	C ₅₈ H ₆₈ CuF ₆ N ₈ O ₁₄ S ₂ + solvent	C ₆₄ H ₈₀ Cl ₂ CuN ₁₂ O ₂₆	C _{64.35} H _{81.05} Cl ₂ N _{12.35} NiO _{26.70}
<i>F_w</i> (g mol ⁻¹)	754.17	754.17	1342.87	1567.84	1584.37
Crystal system	Orthorhombic	Triclinic	Monoclinic	Monoclinic	Triclinic
Space group	<i>P</i> 2 ₁ 2 ₁ 2 ₁	<i>P</i> 1	<i>P</i> 2	<i>P</i> 2 ₁	<i>P</i> 1
<i>a</i> (Å)	8.5476(1)	8.61725(19)	19.2084(4)	10.6841(2)	10.8136(3)
<i>b</i> (Å)	11.1184(1)	9.0624(2)	10.2197(3)	24.5941(5)	14.3149(4)
<i>c</i> (Å)	34.2531(4)	11.6675(3)	19.4085(6)	14.2949(3)	14.8173(5)
α (°)	90	109.288(2)	90	90	114.840(3)
β (°)	90	95.2123(17)	104.758(3)	100.679(2)	110.408(3)
γ (°)	90	103.5763(19)	90	90	95.136(2)
<i>V</i> (Å ³)	3255.26(6)	821.78(3)	3684.28(18)	3691.16(13)	1874.20(11)
<i>Z</i>	4	1	2	2	1
<i>D_{calc}</i> (g cm ⁻³)	1.539	1.524	1.2069(1)	1.411	1.404
<i>F</i> (000)	1540	385	1390.0	1638	829
Radiation (Å), instrument	1.54184 Xcalibur	1.54184 Dualflex	1.54184 Xcalibur	1.54184 Xcalibur	1.54184 Xcalibur
Temperature (K)	293(2)	293(2)	150.0(2)	113(3)	136(11)
Reflections collected	10312	9619	41089	22123	18687
Independent reflections	5766	4439	14307	12247	9207
<i>R_{init}</i>	0.0328	0.0327	0.0707	0.0571	0.0260
Reflections observed	5630	4284	12262	11668	9000
Parameters	428	429	824	1024	1010
Flack parameter	-0.003(19)	-0.06(3)	0.041(19)	0.00(3)	-0.008(16)
<i>R₁</i> [<i>I</i> > 2σ(<i>I</i>)] ^[a]	0.0385	0.0531	0.0974	0.0773	0.0520
<i>wR₂</i> (all data) ^[b]	0.1135	0.1472	0.2806	0.2077	0.1437
Goof, <i>S</i> ^[c]	1.040	1.031	1.161	1.015	1.044
Maximum/minimum electron density (e Å ⁻³)	0.229/-0.282	0.931/-0.471	0.808/-0.743	1.054/-1.012	0.880/-0.575

[a] $R_1 = \sum ||F_o| - |F_c|| / \sum |F_o|$. [b] $wR_2 = \{\sum [w(F_o^2 - F_c^2)^2] / \sum [w(F_o^2)^2]\}^{1/2}$. [c] $S = \{\sum [w(F_o^2 - F_c^2)^2] / (n - p)\}^{1/2}$ where n is number of reflections and p is the total number of parameters refined.

Table S3. Selected geometrical parameters of ML and ML₂ complexes and geometry determined using FindGeo.⁵

ML Complex	N _{py} -M-N _{py} / °	Geometry (FindGeo)
b2A-Cu-o	164.26	Octahedron (regular), RMSD = 0.284
b2B-Cu-t	160.91	Octahedron (regular), RMSD = 0.321

ML ₂ Complex	carbonyl-M-carbonyl / °	N2-M-N2 / °	Geometry (FindGeo)
i3A-Cu	97.85, 98.25	177.67	Octahedron (regular), RMSD = 0.422
i3B-Cu	80.86, 105.45	173.26	Octahedron (distorted), RMSD = 0.481
i3B-Ni	86.10, 96.78	172.12	Octahedron (regular), RMSD = 0.296

Table S4. Hydrogen bond parameters

Hydrogen bond	D-H	H...A	D...A	D-H...A
b2A-Cu-o				
O1W-H1W...O2T1 ⁱ	0.79(4)	2.02(5)	2.726(5)	148(5)
O1W-H2W...O3T1	0.82(8)	1.92(9)	2.718(5)	166(9)
N4-H4N...O3T2	0.86(5)	2.05(4)	2.883(6)	166(5)
Symmetry code (i): 1/2+x, 1/2-y, -z				
b2A-Cu-t				

O1W–H1W…O1T2	0.80(2)	1.98(4)	2.675(7)	145(7)
O1W–H2W…O3T1	0.81(6)	1.90(6)	2.695(9)	166(6)
N4–H4N…O2T2 ⁱ	0.86(7)	2.01(7)	2.864(9)	174(3)

Symmetry code (i): $x, 1+y, z$

i3A-Cu

N11–H11A…O1TA[B]	0.86	1.93 [2.03]	2.79(9) [2.88(2)]	173 [169]
N12–H12A…O2T1 ⁱ	0.86	2.01	2.845(8)	165
N31–H31A…O1W1	0.86	2.02	2.841(12)	160
N31–H32A…O1W2	0.86	2.01	2.837(10)	160
N41–H41A…O2TA[B] ⁱ	0.86	2.19 [2.16]	3.02(1) [2.99(2)]	163
N42–H42A…O1T1	0.86	2.11	2.961(9)	172

Symmetry code (i): $x, 1+y, z$

i3B-Cu

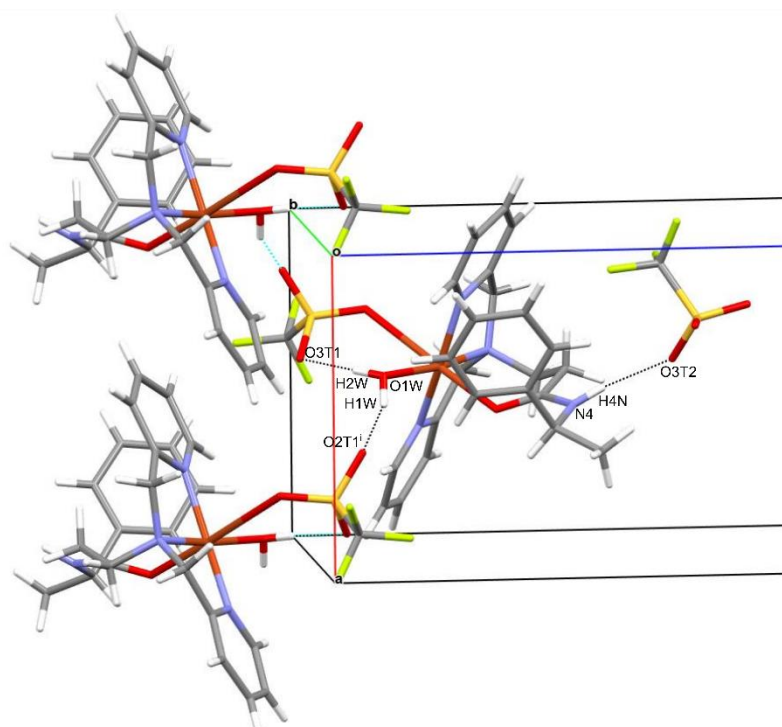
N11–H11N…O32 ⁱ	0.80(6)	2.06(8)	2.786(8)	151(8)
N12–H12N…O2P1 ⁱⁱ	0.81(4)	2.17(5)	2.913(8)	153(7)
N31–H31N…O3P1	0.80(6)	2.35(5)	3.066(8)	150(6)
N32–H32N…O1PA	0.80(5)	2.17(6)	2.930(9)	150(6)
N41–H41N…O41 (intra)	0.81(7)	2.36(7)	2.696(9)	106(6)
N42–H42N…O42 (intra)	0.80(8)	2.34(7)	2.673(8)	106(6)

Symmetry codes (i): $1+x, y, z$; (ii): $-1+x, y, z$

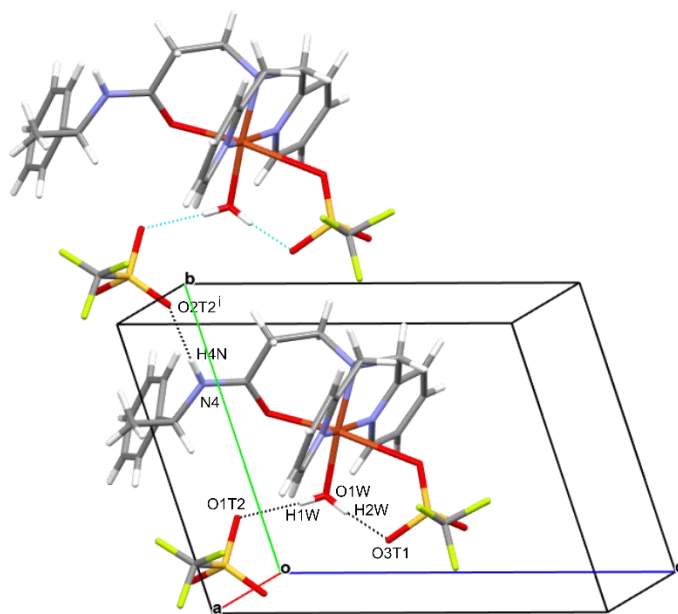
i3B-Ni

N11–H11N…O32 ⁱ	0.81(6)	1.97(6)	2.764(6)	170(6)
N12–H12N…O2P1 ⁱⁱ	0.80(4)	2.19(5)	2.989(6)	178(9)
N31–H31N…O3P1	0.81(8)	2.32(8)	3.100(6)	165(7)
N32–H32N…O1P2	0.82(5)	2.08(5)	2.898(7)	173(7)
N41–H41N…O42 ⁱⁱⁱ	0.81(6)	2.54(6)	3.301(7)	159(6)
N42–H42N…O42 (intra)	0.80(7)	2.37(7)	2.695(7)	106(6)

Symmetry codes (i): $1+x, y, z$; (ii): $-1+x, y, z$; (iii): $1+x, 1+y, z$



(a)



(b)

Figure S32. Hydrogen bonds in **b2A-Cu-o** (a) and **b2A-Cu-t** (b). Parameters and symmetry codes are given in Table S4.

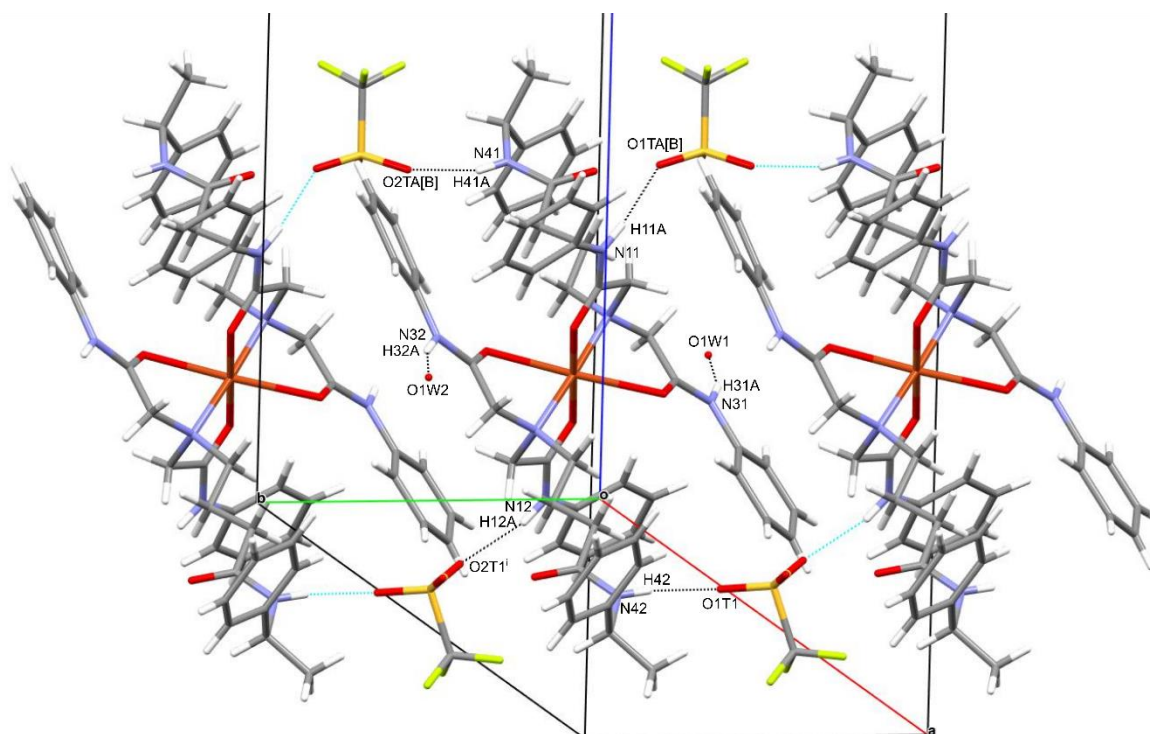


Figure S33. Hydrogen bonds in **i3A-Cu**. Parameters and symmetry codes are given in Table S4.

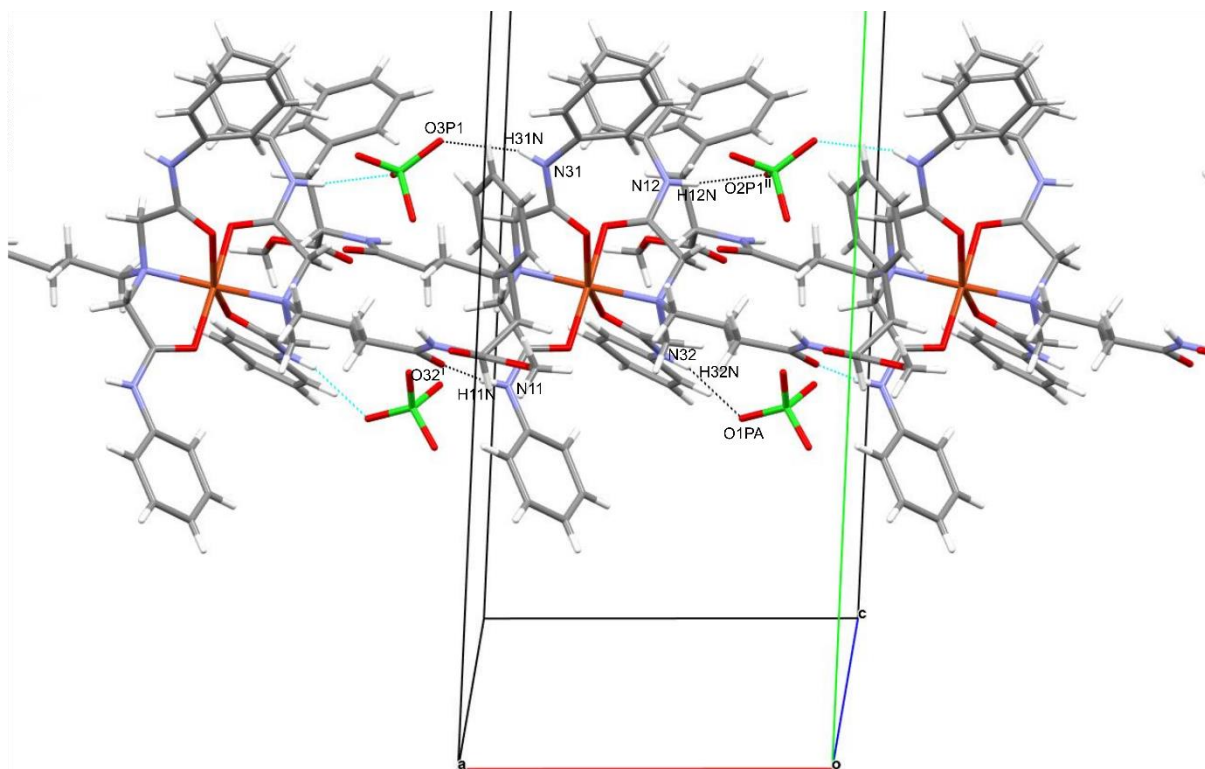


Figure S34. Intermolecular hydrogen bonds in **i3B-Cu**. Parameters and symmetry codes are given in Table S4.

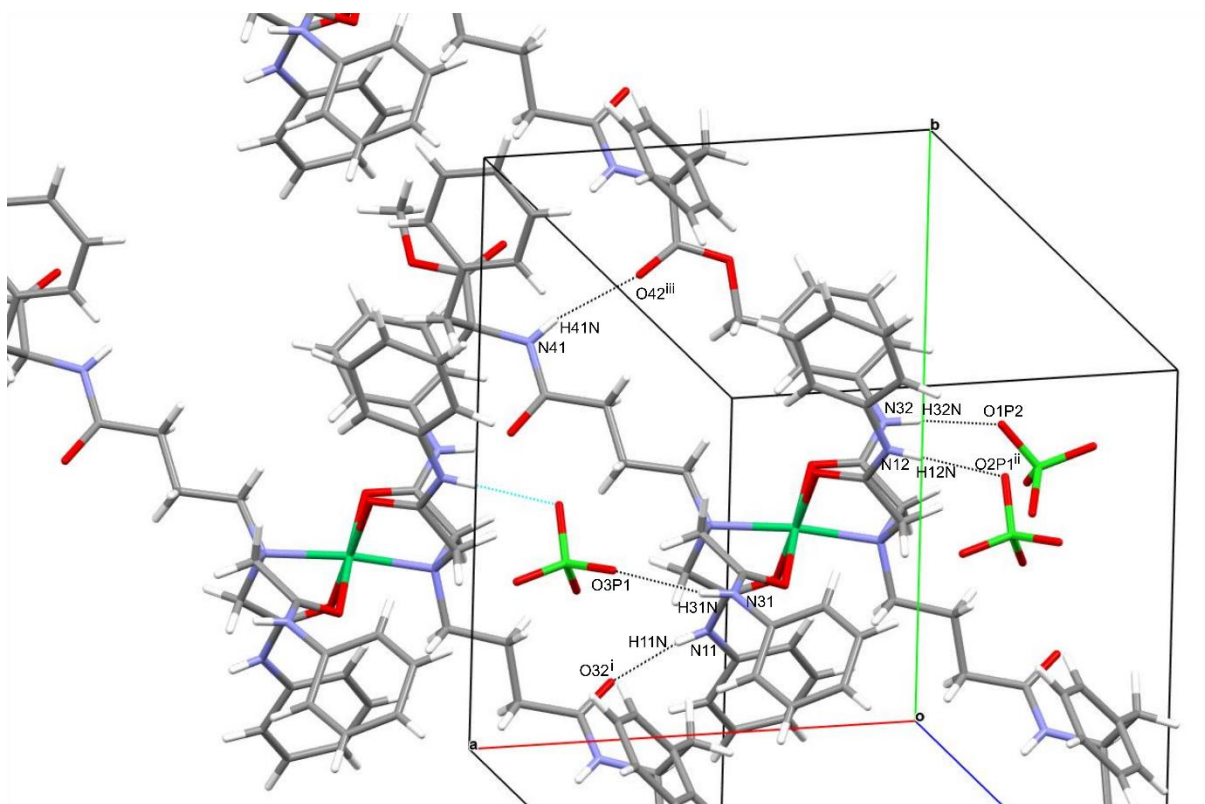


Figure S35. Intermolecular hydrogen bonds in **i3B-Ni**. Parameters and symmetry codes are given in Table S4.

7 Cu(II) complexes

7.1 UV-Vis spectroscopy

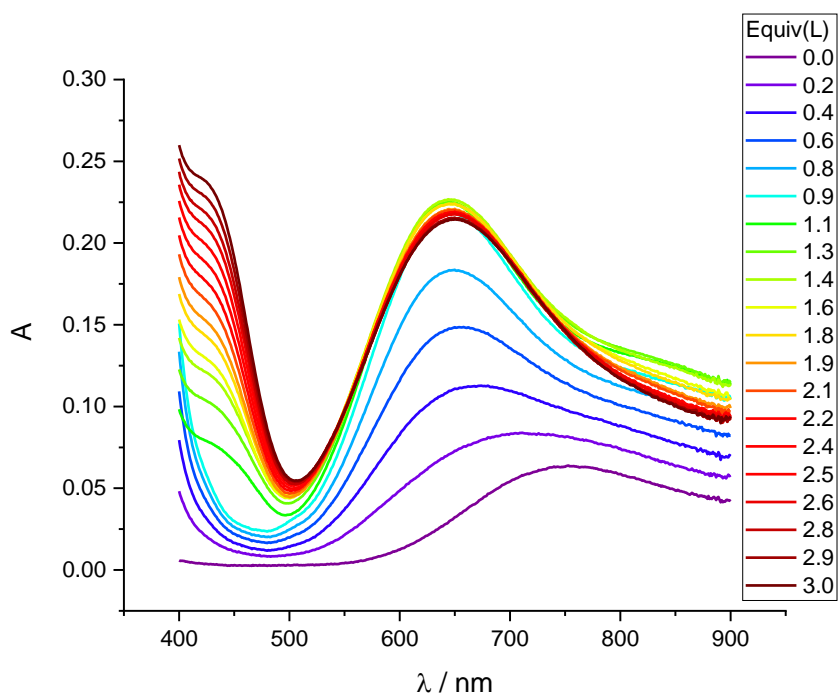


Figure S36. UV-Vis spectra for the titration of Cu(II) (3.22 mM) with ligand **b1A** in acetonitrile.

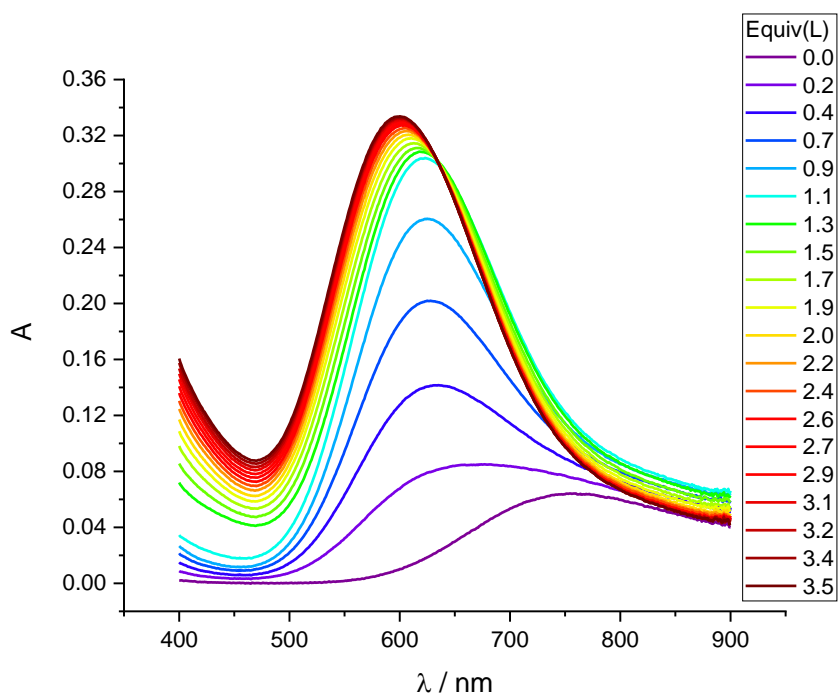


Figure S37. UV-Vis spectra for the titration of Cu(II) (3.41 mM) with ligand **b2A** in acetonitrile.

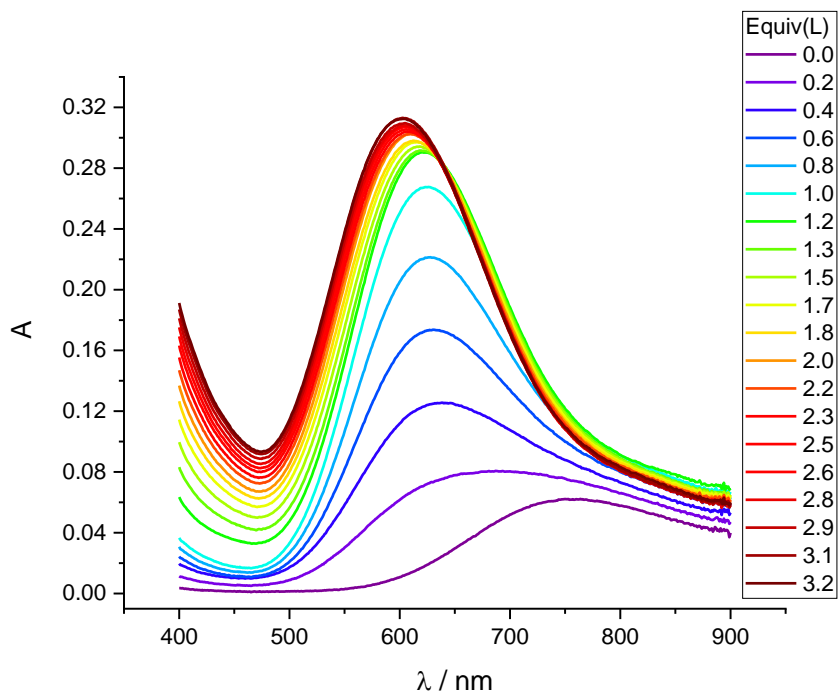


Figure S38. UV-Vis spectra for the titration of Cu(II) (3.41 mM) with ligand **b2B** in acetonitrile.

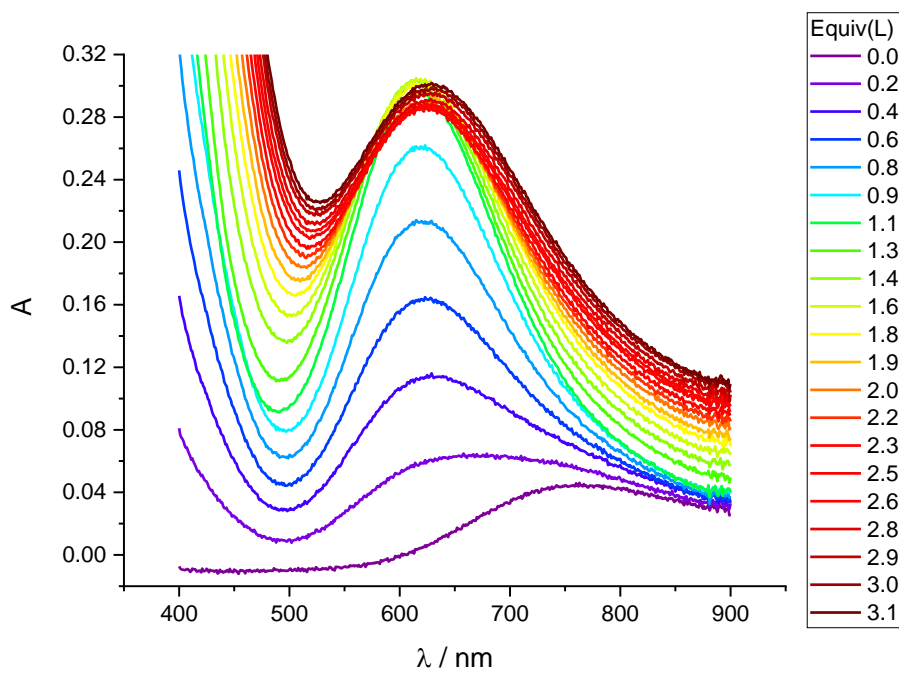


Figure S39. UV-Vis spectra for the titration of Cu(II) (3.13 mM) with ligand **b2C** in acetonitrile.

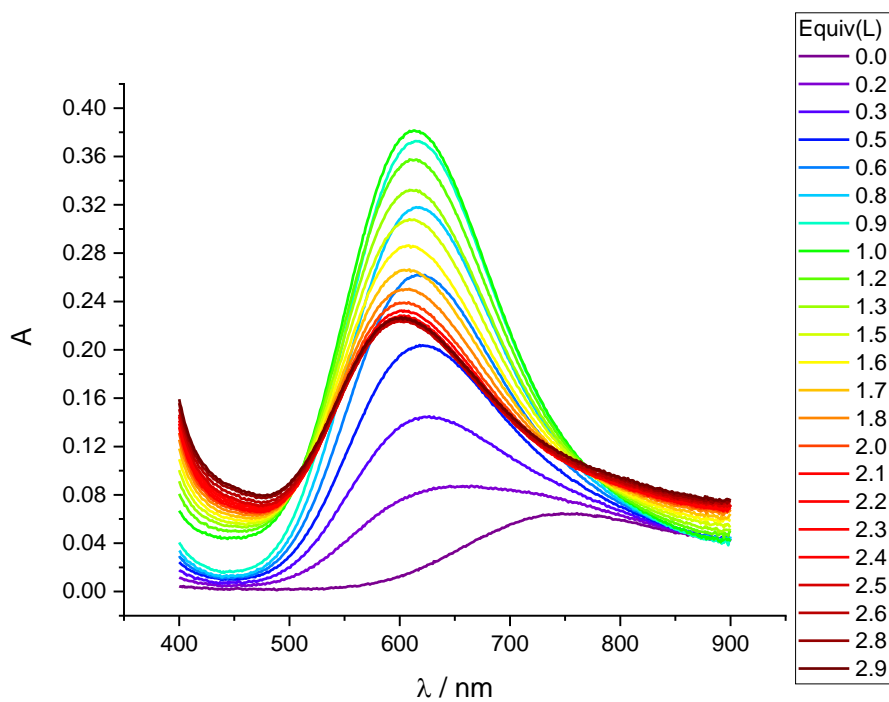


Figure S40. UV-Vis spectra and titration curve for the titration of Cu(II) (3.33 mM) with ligand **b3A** in acetonitrile.

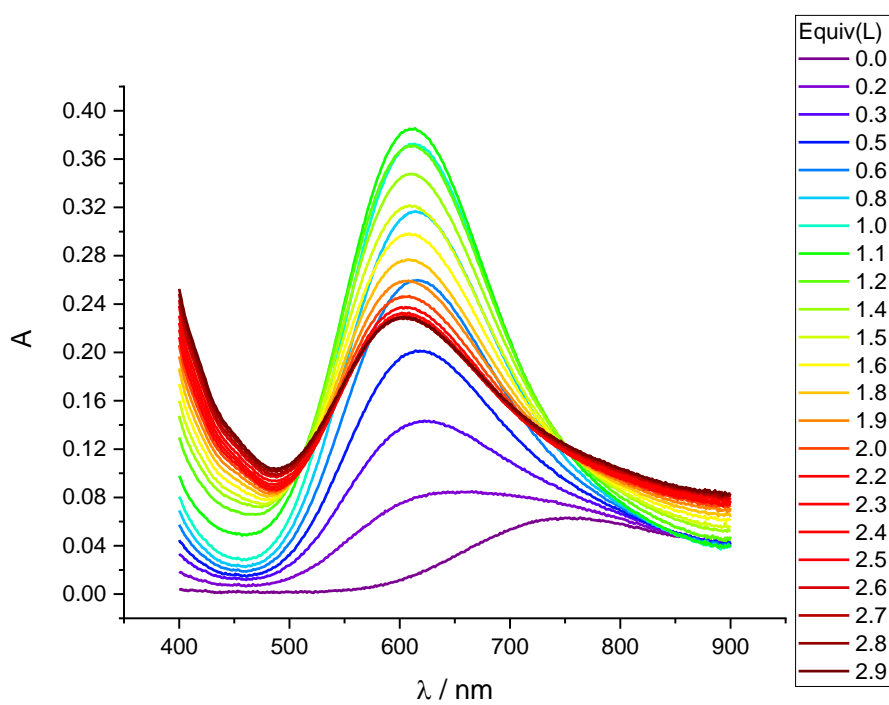


Figure S41. UV-Vis spectra for the titration of Cu(II) (3.33 mM) with ligand **b3B** in acetonitrile.

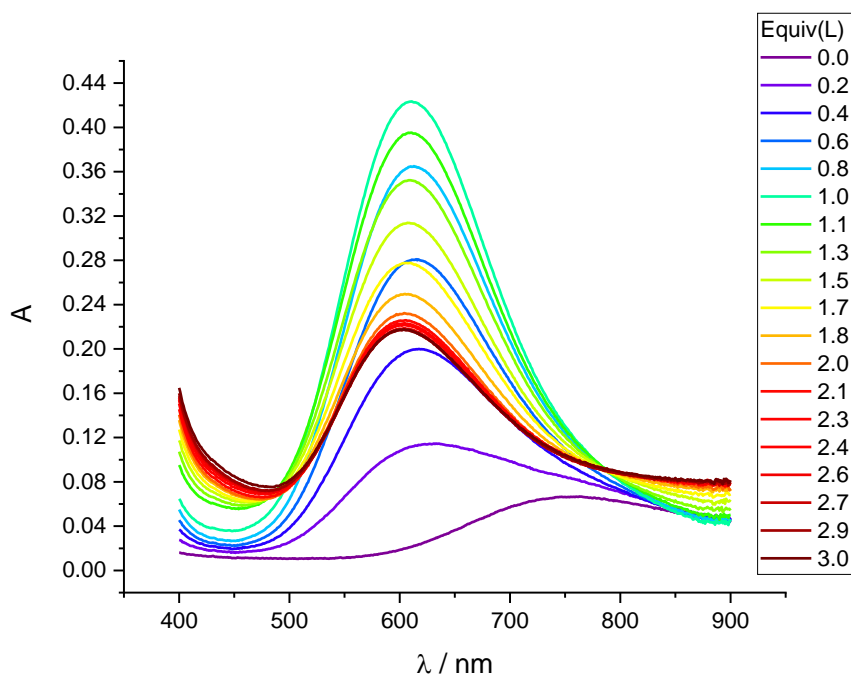


Figure S42. UV-Vis spectra for the titration of Cu(II) (3.38 mM) with ligand **b3C** in acetonitrile.

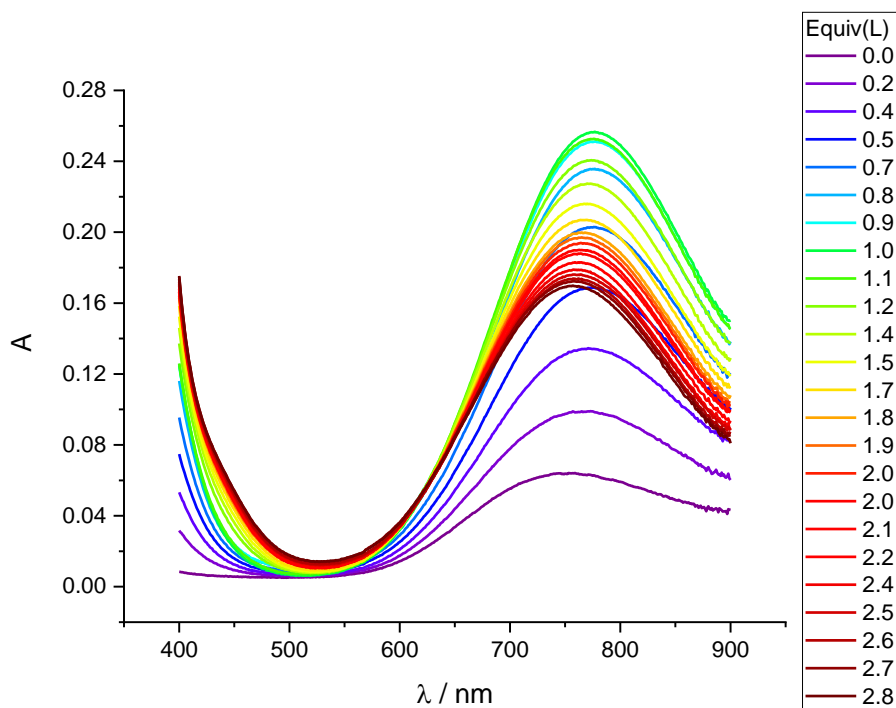


Figure S43. UV-Vis spectra for the titration of Cu(II) (3.24 mM) with ligand **i2A** in acetonitrile.

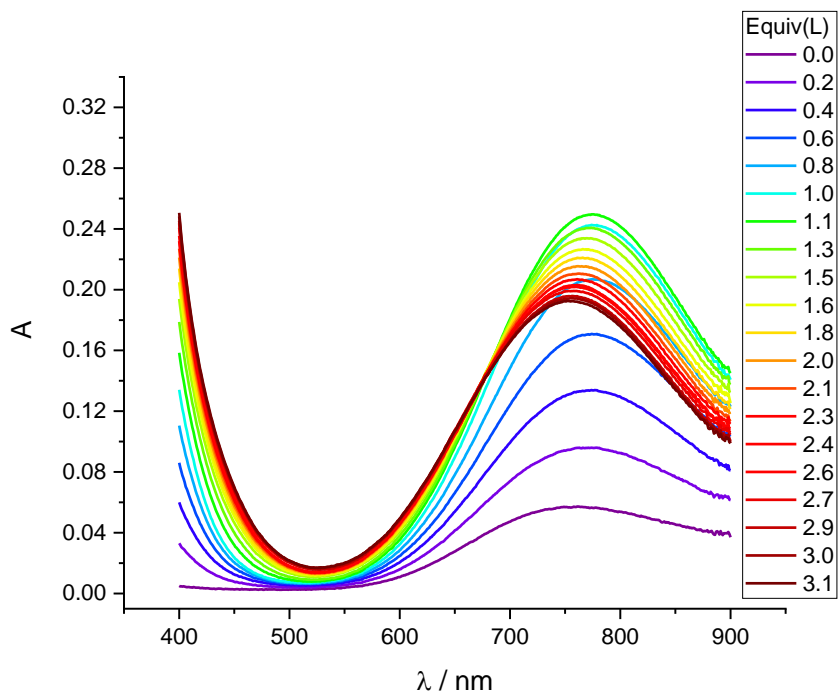


Figure S44. UV-Vis spectra for the titration of Cu(II) (3.04 mM) with ligand **i2B** in acetonitrile.

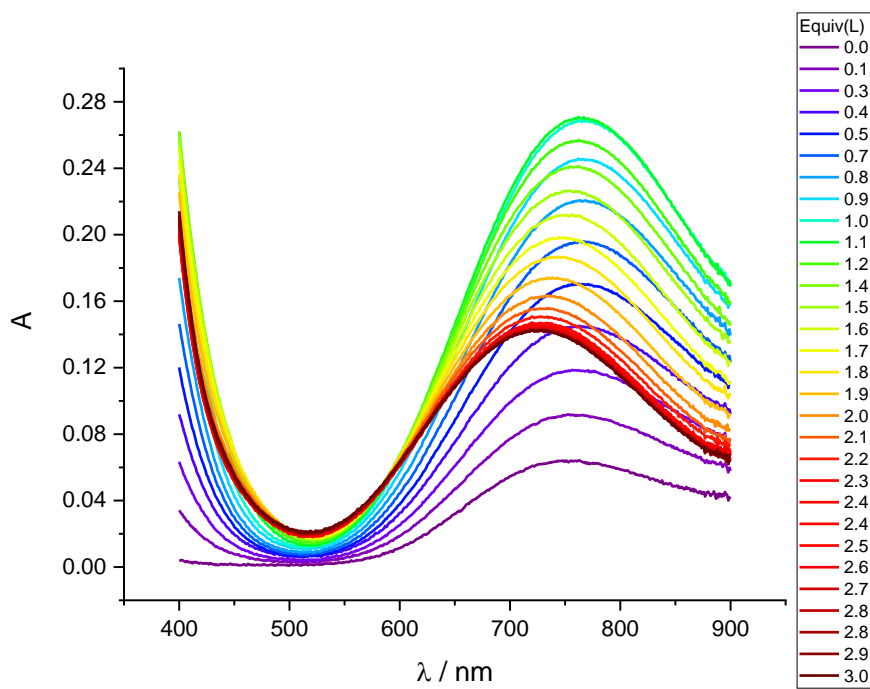


Figure S45. UV-Vis spectra for the titration of Cu(II) (3.43 mM) with ligand **i3A** in acetonitrile.

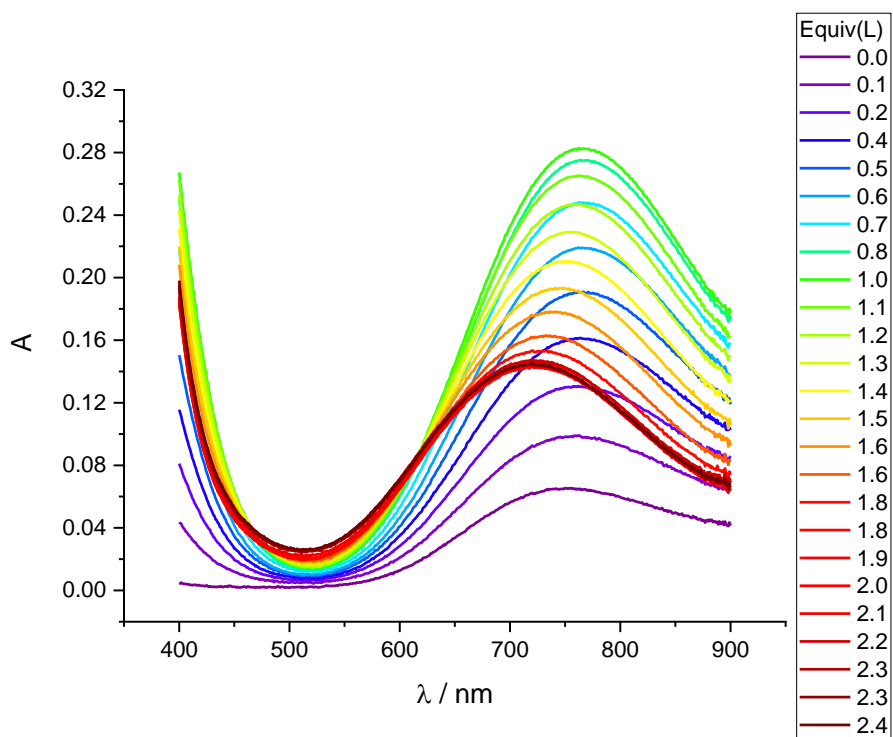


Figure S46. UV-Vis spectra for the titration of Cu(II) (3.43 mM) with ligand **i3B** in acetonitrile.

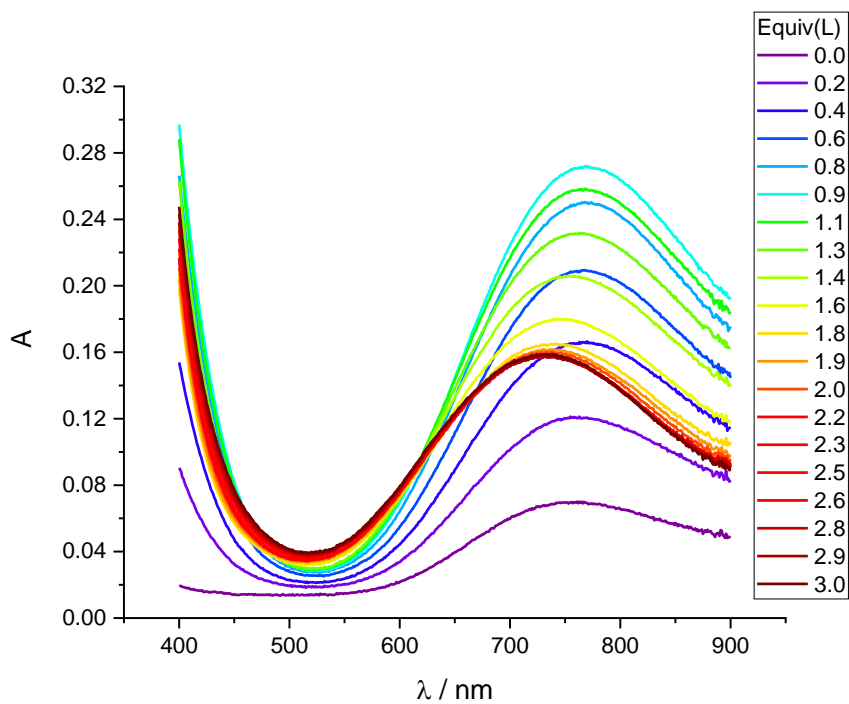


Figure S47. UV-Vis spectra for the titration of Cu(II) (3.43 mM) with ligand **i3C** in acetonitrile.

CD spectroscopic measurements of Cu(II) complexes in acetonitrile (recorded on a Jasco J-815 spectropolarimeter in a 1 cm cuvette) generally showed weak peaks in the visible region (Figures S42-S47), with the exception of **i2A** and **i3A** complexes. In general, stronger CD peaks were observed for a ligand:Cu(II) ratio of 1:1, due to the weaker absorbance of ML_2 compared to ML as observed in the UV-Vis titrations. The presence of additional donor groups in the side chain, especially in phenylalanine derivatives B and C, offers many coordination possibilities, making the interpretation of UV and CD results less straightforward.

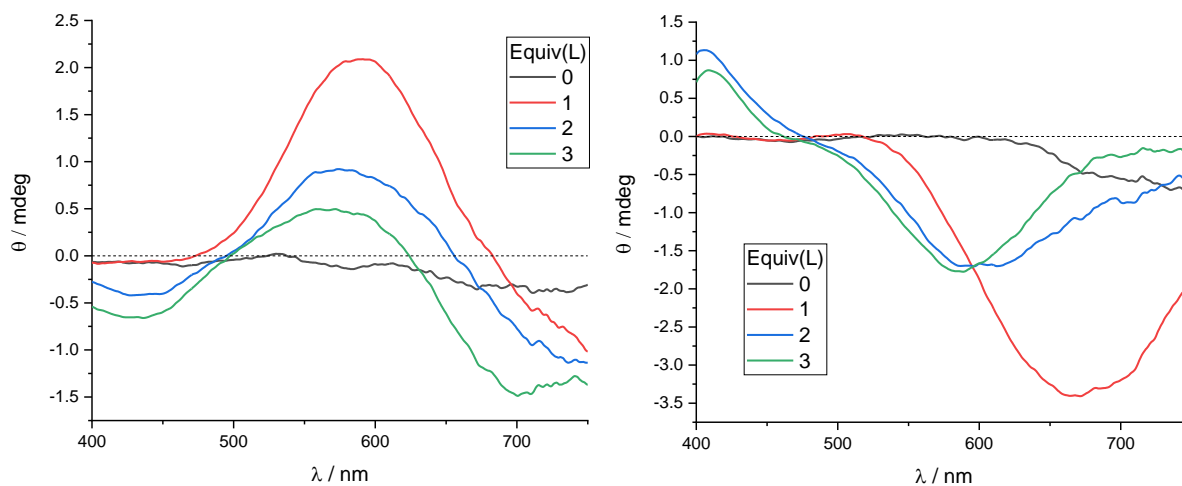


Figure S48. CD spectra of Cu(II) with different equivalents of **b1A**, $c(\text{Cu}^{II}) = 3.22 \text{ mM}$ (left) and **b2C**, $c(\text{Cu}^{II}) = 3.22 \text{ mM}$ (right) in acetonitrile.

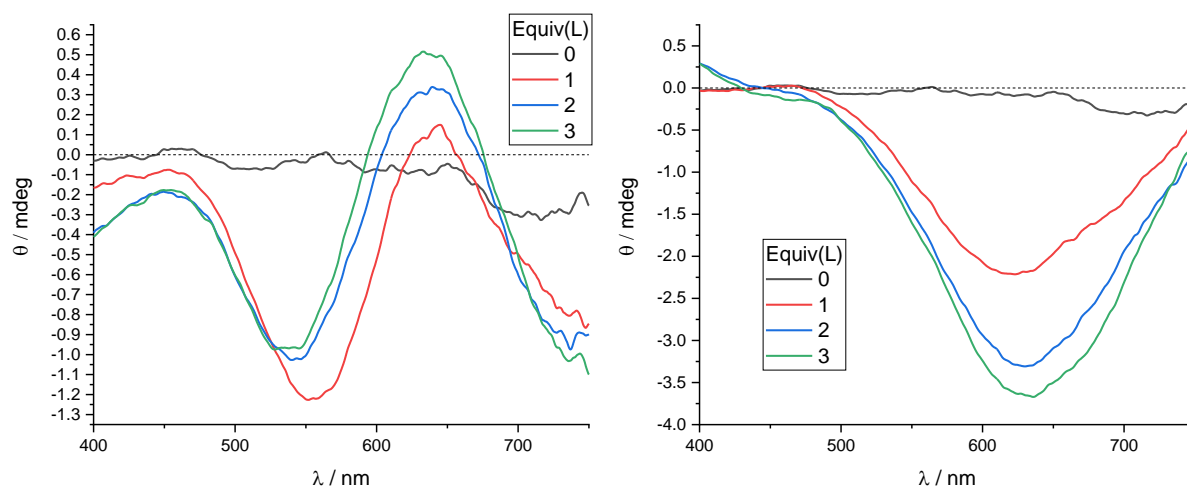


Figure S49. CD spectra of Cu(II) with different equivalents of **b2A**, $c(\text{Cu}^{II}) = 3.13 \text{ mM}$ (left) and **b2B**, $c(\text{Cu}^{II}) = 3.13 \text{ mM}$ (right) in acetonitrile.

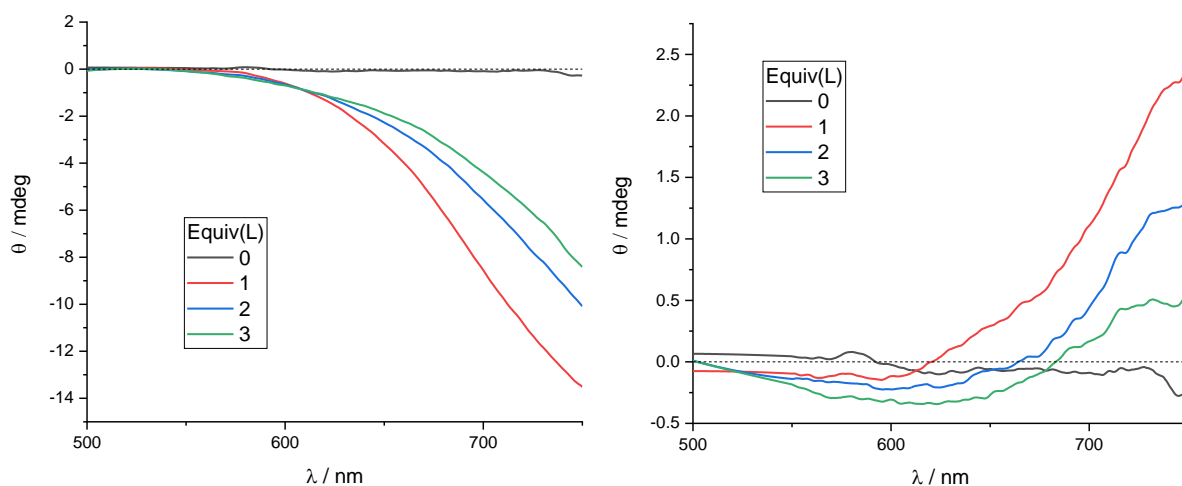


Figure S50. CD spectra of Cu(II) with different equivalents of **i2A**, $c(\text{Cu}^{\text{II}}) = 3.13 \text{ mM}$ (left) and **i2B**, $c(\text{Cu}^{\text{II}}) = 3.13 \text{ mM}$ (right) in acetonitrile. The peaks of imda complexes could not be completely observed, as the instrument does not give reliable data for wavelengths higher than 750 nm.

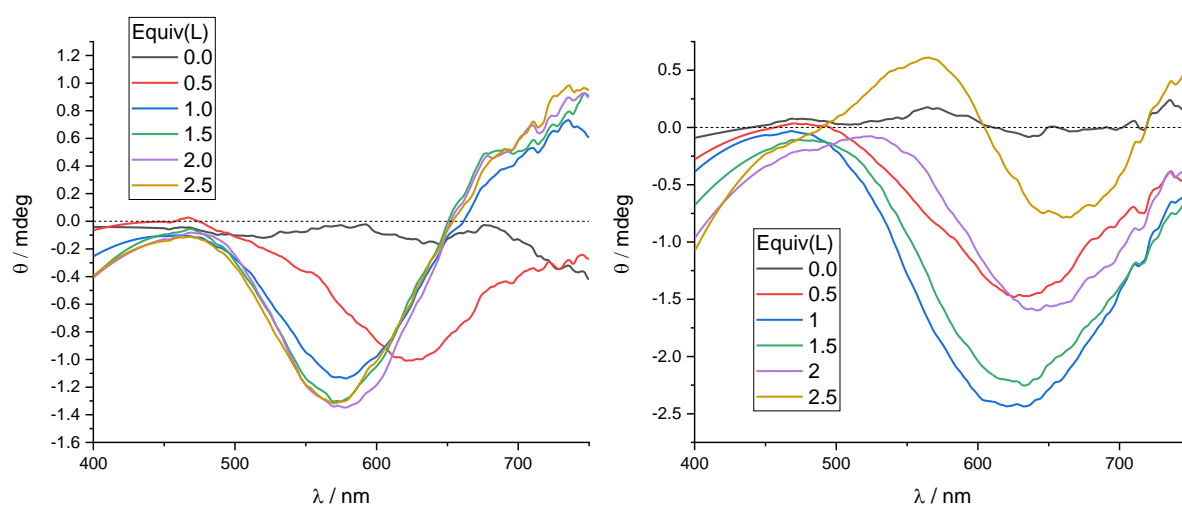


Figure S51. CD spectra of Cu(II) with different equivalents of **b3A**, $c(\text{Cu}^{\text{II}}) = 5.56 \text{ mM}$ (left) and **b3B**, $c(\text{Cu}^{\text{II}}) = 5.56 \text{ mM}$ (right) in acetonitrile.

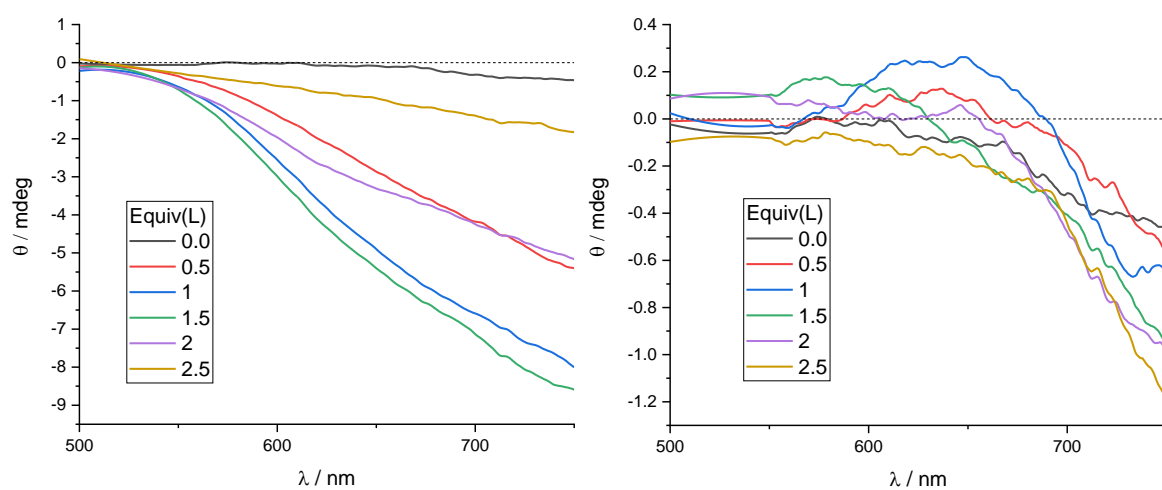


Figure S52. CD spectra of Cu(II) with different equivalents of **i3A**, $c(\text{Cu}^{\text{II}}) = 5.42 \text{ mM}$ (left) and **i3B**, $c(\text{Cu}^{\text{II}}) = 5.42 \text{ mM}$ (right) in acetonitrile.

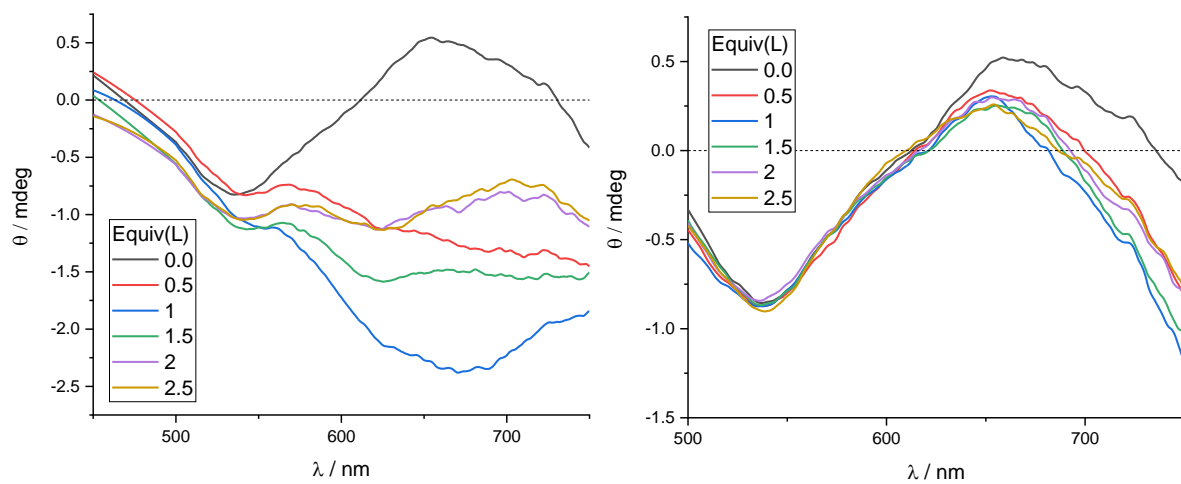


Figure S53. CD spectra of Cu(II) with different equivalents of **b3C**, $c(\text{Cu}^{\text{II}}) = 6.07 \text{ mM}$ (left) and **i3C**, $c(\text{Cu}^{\text{II}}) = 6.07 \text{ mM}$ (right) in acetonitrile.

8 NMR of Zn(II) complexes

8.1 ^1H NMR spectra with 0.5 and 1 added equivalents of $\text{Zn}(\text{CF}_3\text{SO}_3)_2$

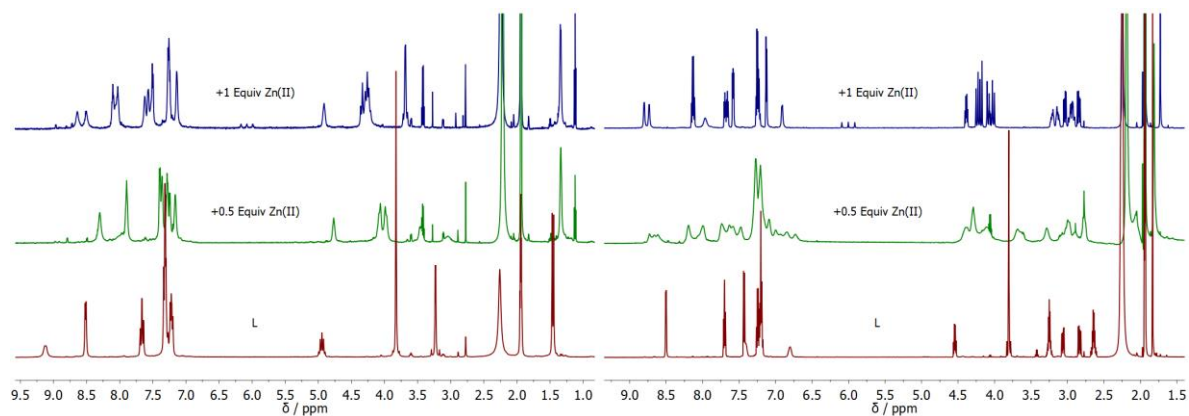


Figure S54. ^1H NMR spectra of **b1A** (left) and **b2C** (right) upon addition of $\text{Zn}(\text{CF}_3\text{SO}_3)_2$ in acetonitrile- d_3

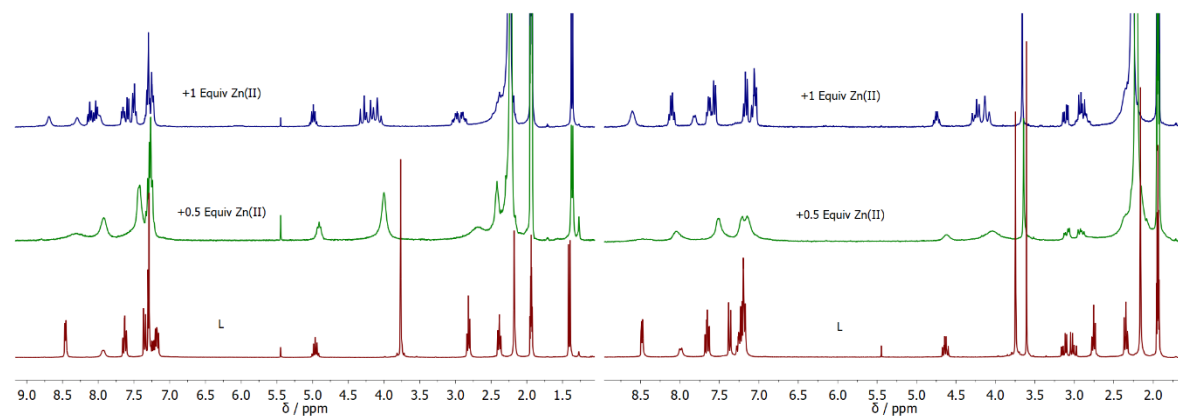


Figure S55. ^1H NMR spectra of **b2A** (left) and **b2B** (right) upon addition of $\text{Zn}(\text{CF}_3\text{SO}_3)_2$ in acetonitrile- d_3

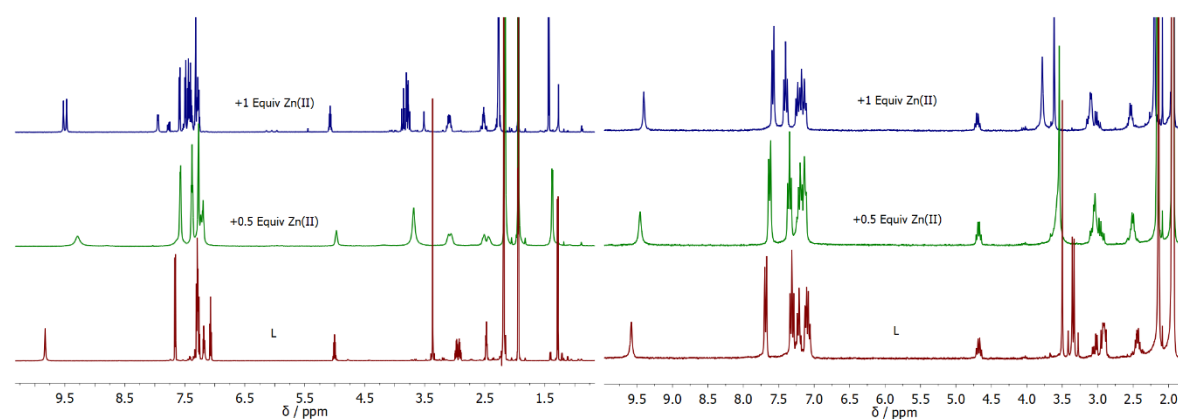


Figure S56. ^1H NMR spectra of **i2A** (left) and **i2B** (right) upon addition of $\text{Zn}(\text{CF}_3\text{SO}_3)_2$ in acetonitrile- d_3

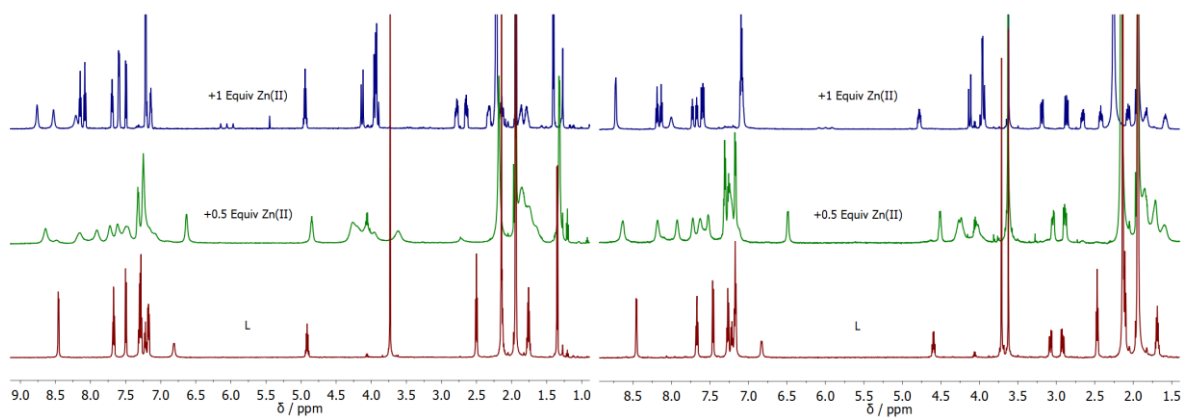


Figure S57. ^1H NMR spectra of **b3A** (left) and **b3B** (right) upon addition of $\text{Zn}(\text{CF}_3\text{SO}_3)_2$ in acetonitrile- d_3

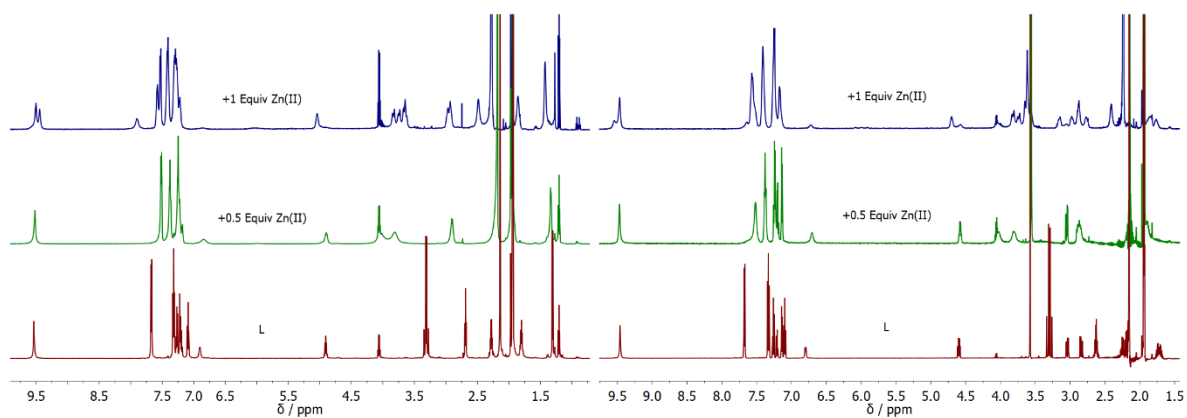


Figure S58. ^1H NMR spectra of **i3A** (left) and **i3B** (right) upon addition of $\text{Zn}(\text{CF}_3\text{SO}_3)_2$ in acetonitrile- d_3

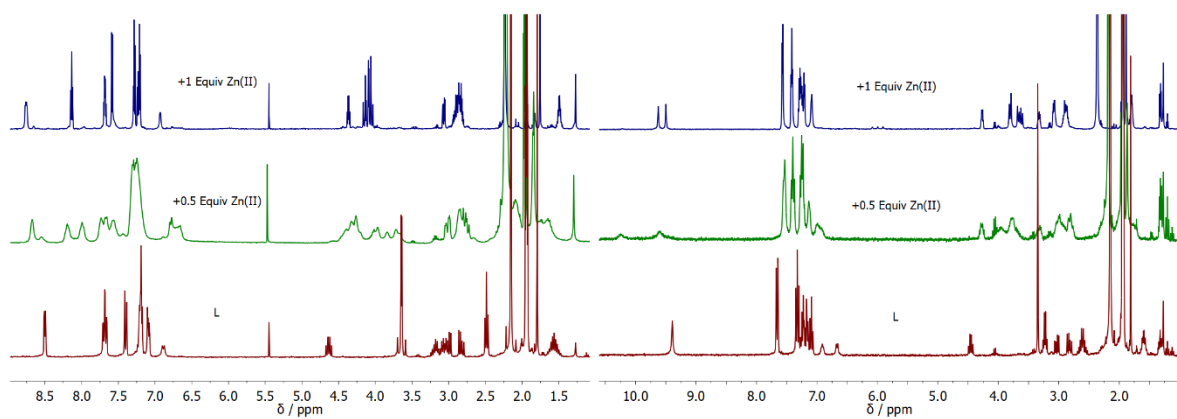


Figure S59. ^1H NMR spectra of **b3C** (left) and **i3C** (right) upon addition of $\text{Zn}(\text{CF}_3\text{SO}_3)_2$ in acetonitrile- d_3

8.2 ^{13}C and 2D NMR spectra of ML complexes

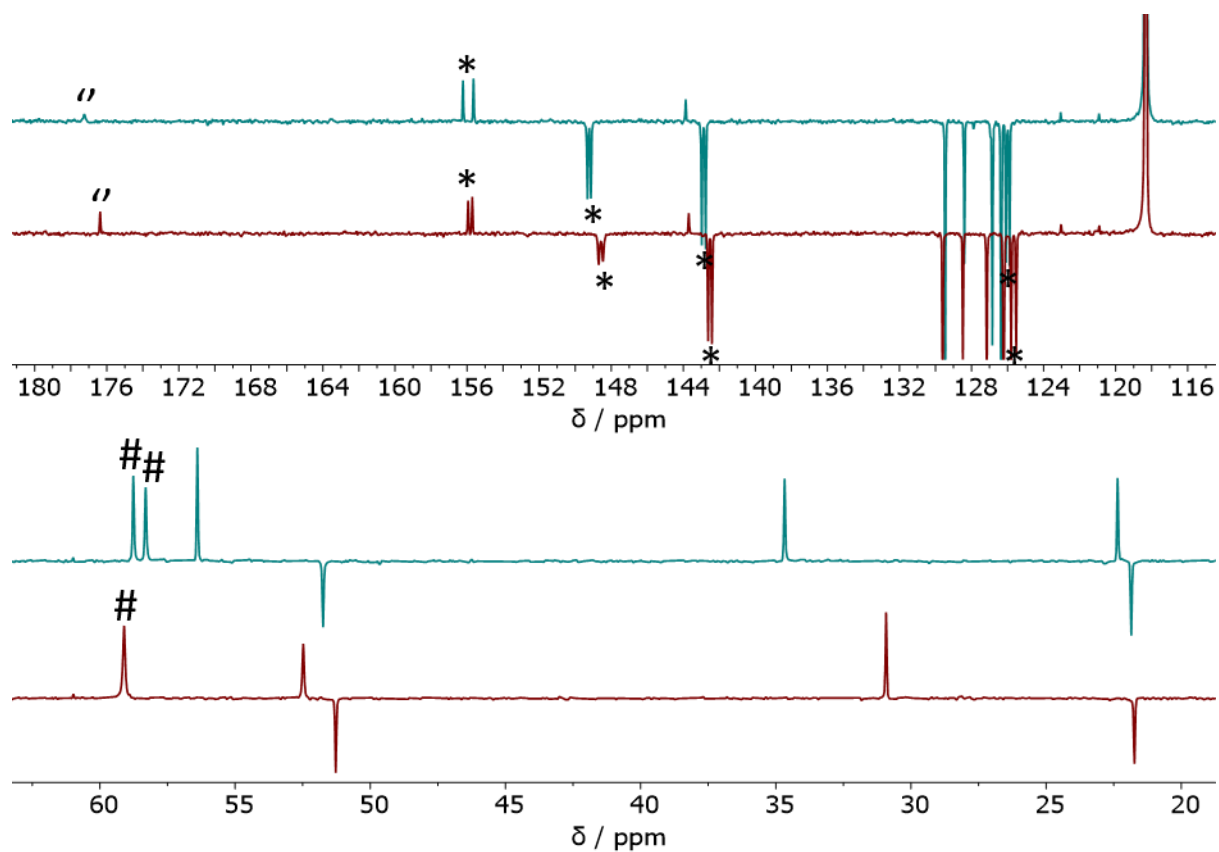


Figure S60. ^{13}C APT NMR of $[\text{Zn}(\text{b2A})]^{2+}$ (red) and $[\text{Zn}(\text{b3A})]^{2+}$ (blue) in acetonitrile- d_3 . Carbonyl ("), pyridine (*) and chelator methylene carbons (#) are accented.

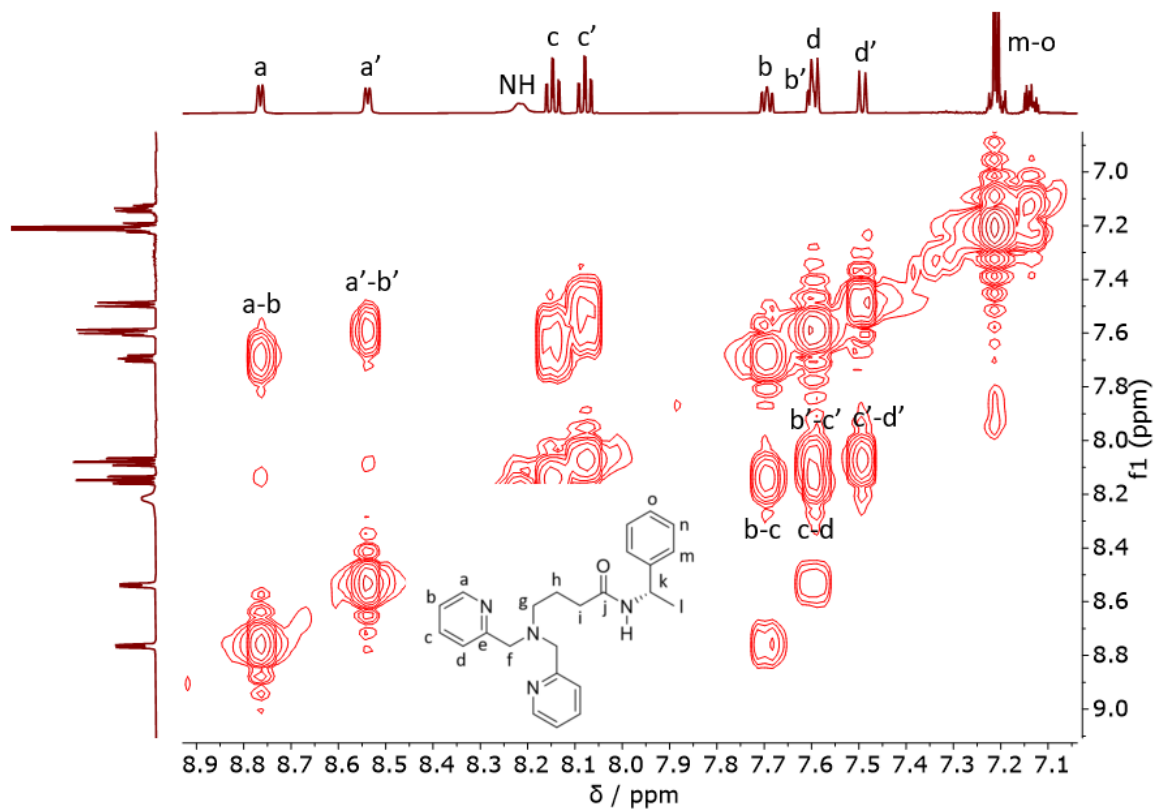


Figure S61. COSY NMR of $[\text{Zn}(\text{b3A})]^{2+}$ (acetonitrile- d_3), aromatic region.

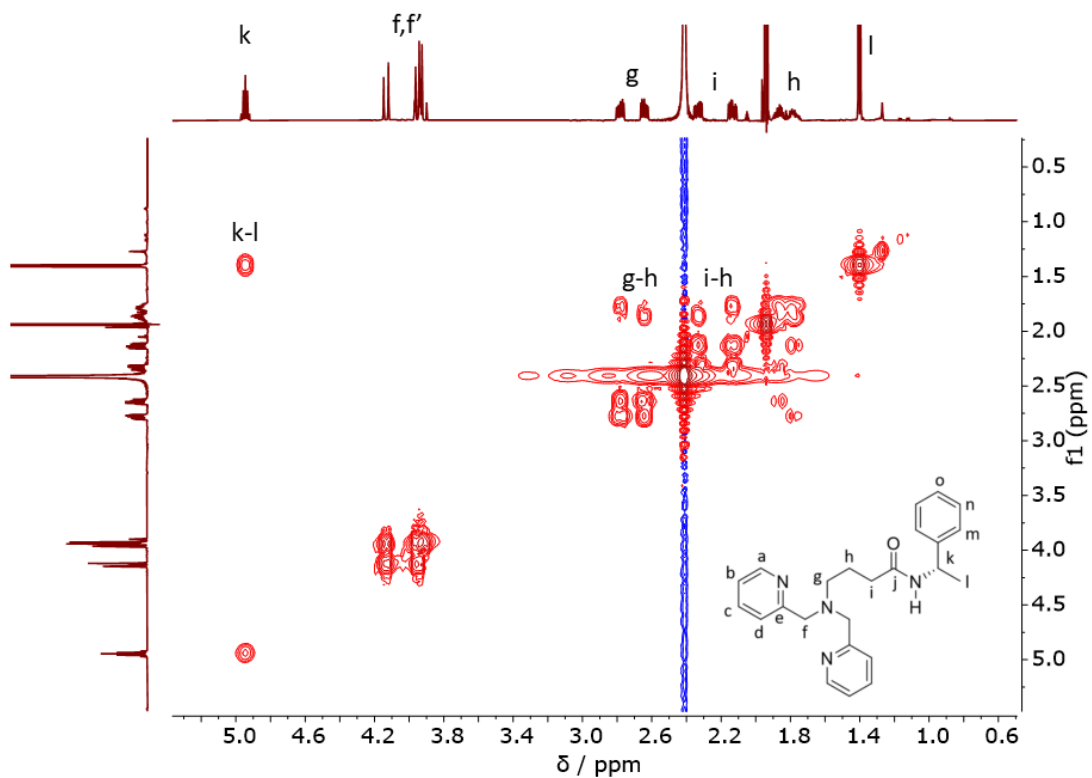


Figure S62. COSY NMR of $[\text{Zn}(\text{b3A})]^{2+}$ (acetonitrile- d_3), aliphatic region.

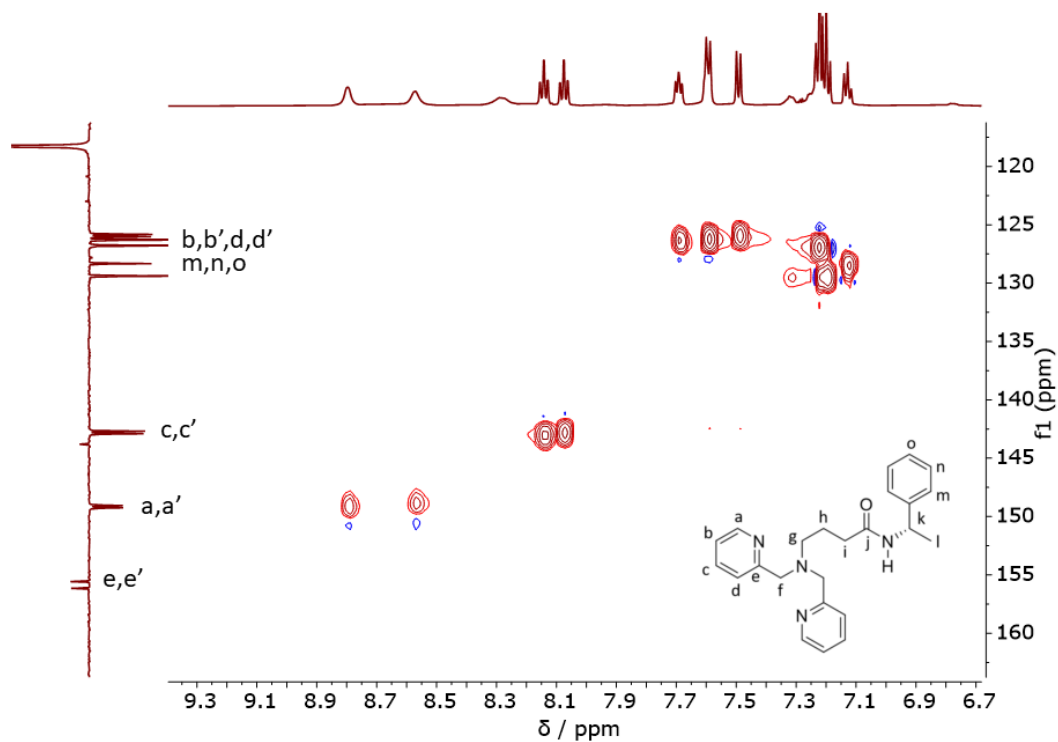


Figure S63. HSQC NMR of $[\text{Zn}(\text{b3A})]^{2+}$ (acetonitrile- d_3), aromatic region.

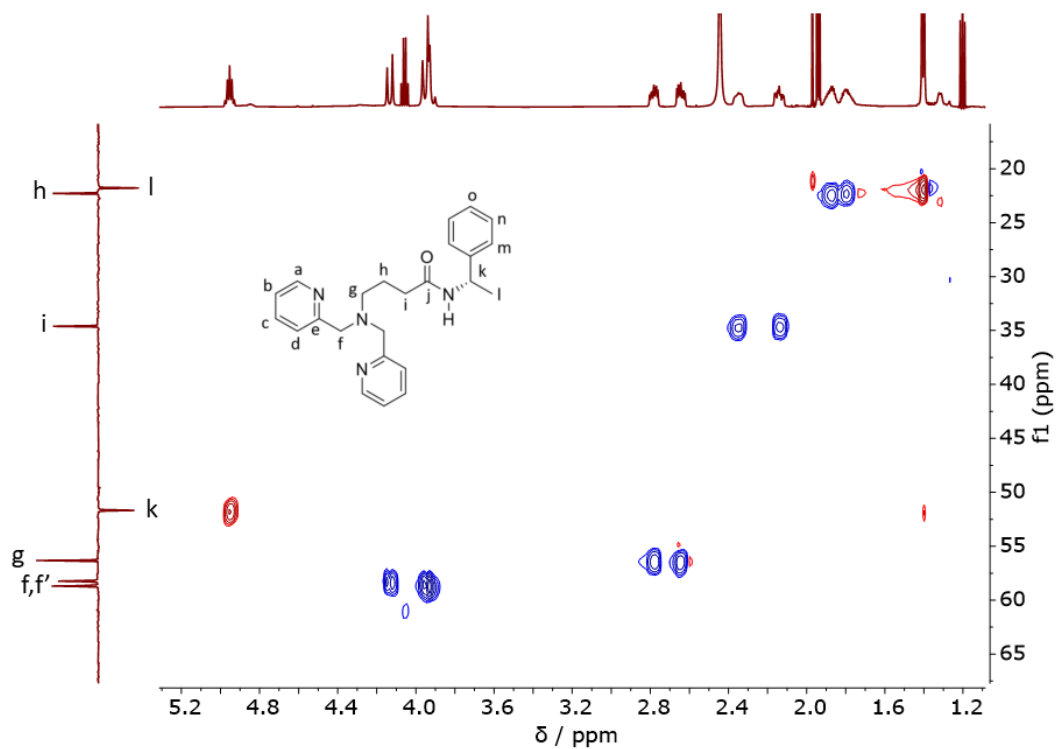


Figure S64. HSQC NMR of $[\text{Zn}(\text{b3A})]^{2+}$ (acetonitrile- d_3), aliphatic region.

8.3 ^1H NMR spectra of different L : M ratios at -40°C

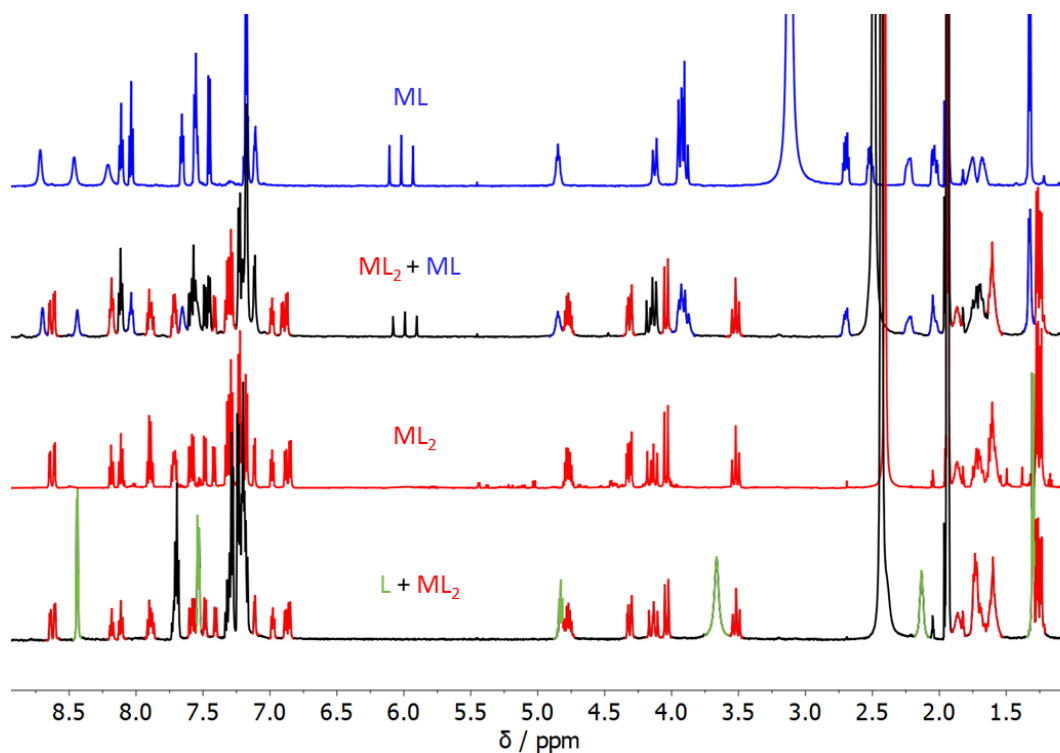


Figure S65. ^1H NMR ($\text{acetonitrile-}d_3$) spectra at -40°C of **b3A** with different equiv. of $\text{Zn}(\text{CF}_3\text{SO}_3)_2$. From bottom to top: 0.25, 0.5, 0.75, and 2 equiv $\text{Zn}(\text{II})$. When larger amounts of $\text{Zn}(\text{CF}_3\text{SO}_3)_2$ are added, NH_4^+ appears as a triplet ($J = 53\text{ Hz}$) around 6.0 ppm.⁶

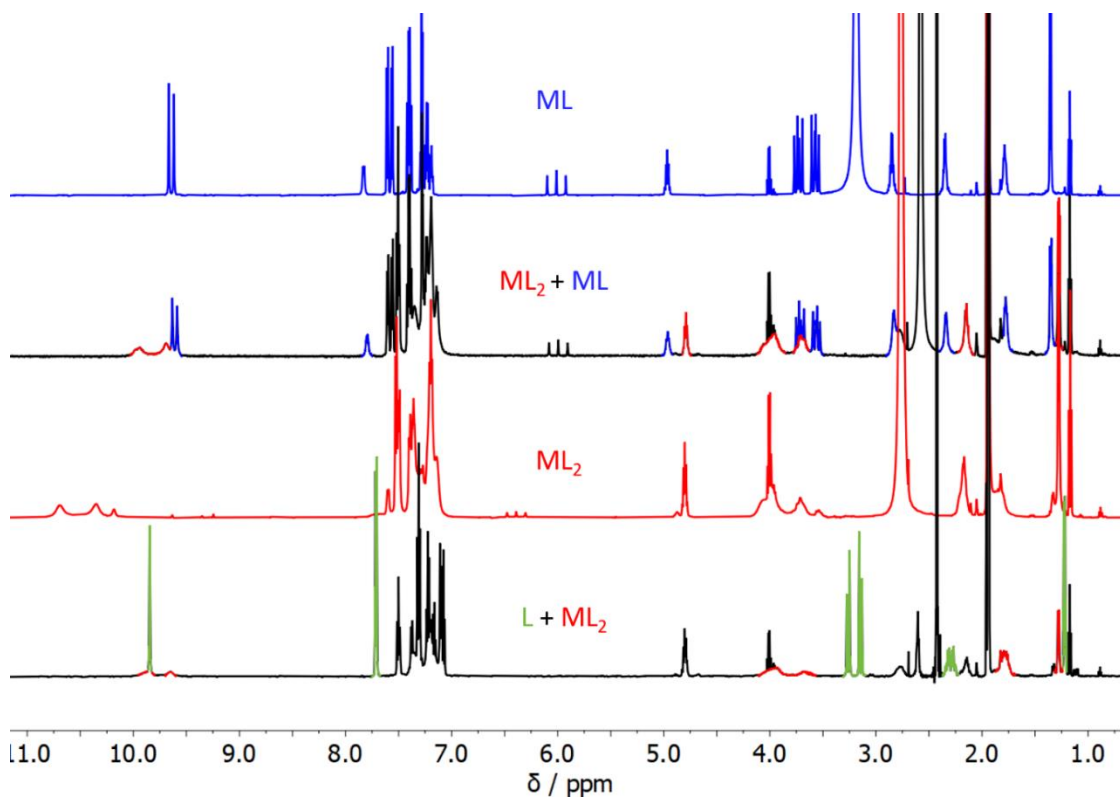


Figure S66. ^1H NMR ($\text{acetonitrile-}d_3$) spectra at -40°C of **i3A** with different equiv. of $\text{Zn}(\text{CF}_3\text{SO}_3)_2$. From bottom to top: 0.25, 0.5, 0.75, and 2 equiv $\text{Zn}(\text{II})$.

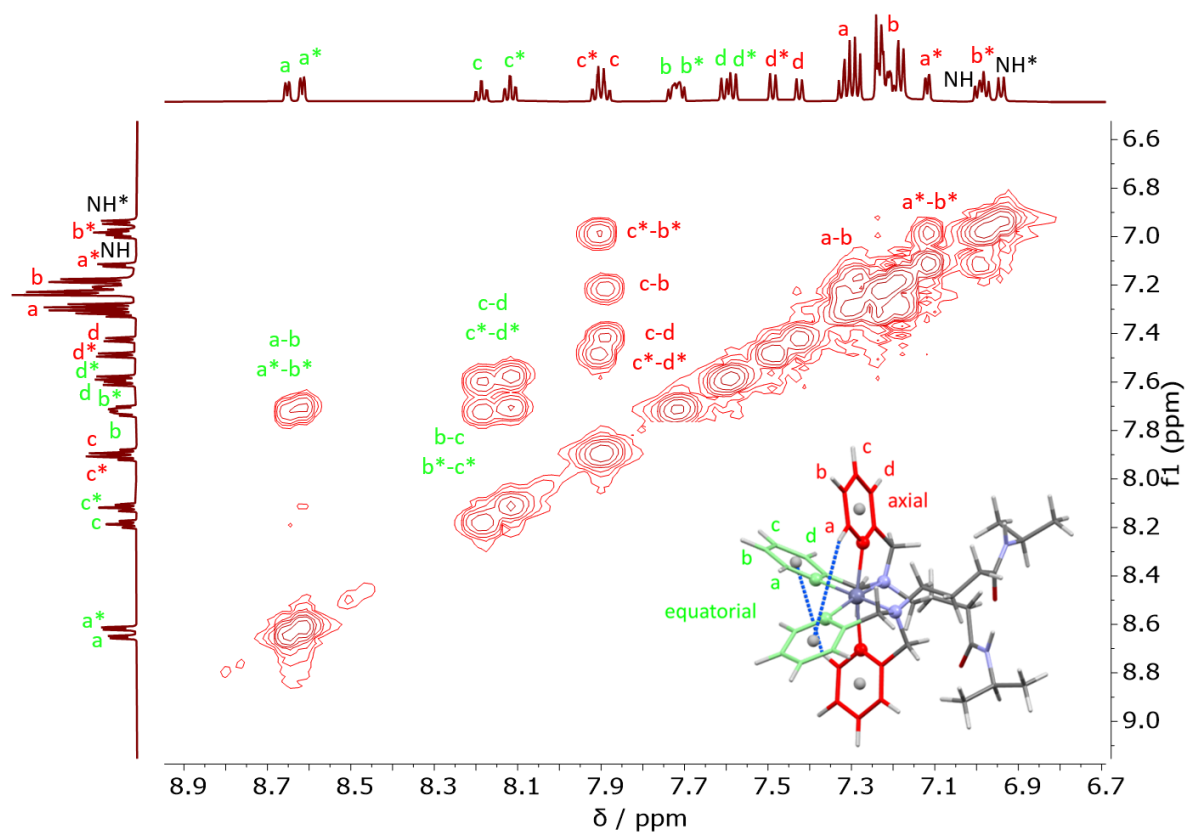


Figure S67. COSY NMR of $[\text{Zn}(\text{b3A})_2]^{2+}$ (acetonitrile- d_3) at $-40\text{ }^\circ\text{C}$ (aromatic region). The second diastereomer is denoted (*)

8.4 Variable temperature ^1H NMR spectra of complexes at a L : Zn(II) ratio of 2 L : 1

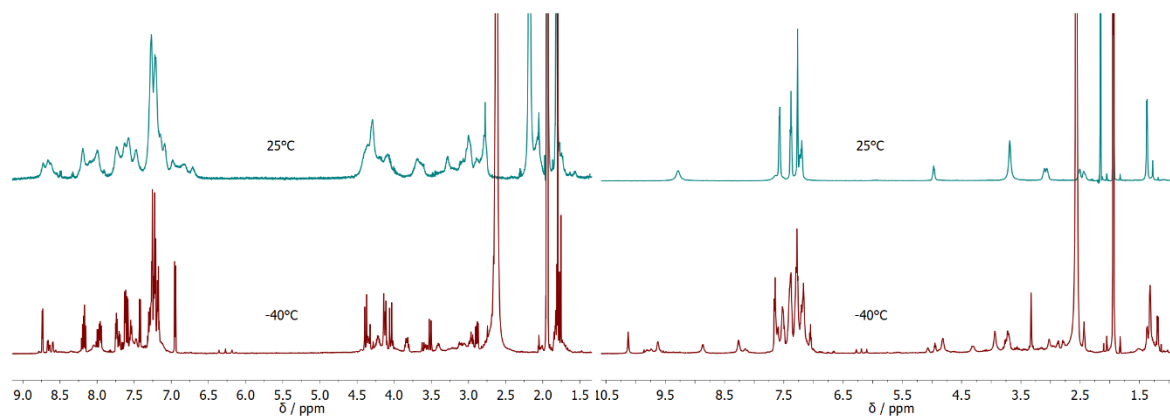


Figure S68. VT ^1H NMR (acetonitrile- d_3) of \mathbf{b}_{2c} (left) and \mathbf{i}_{2a} (right) with 0.5 equiv. Zn(II)

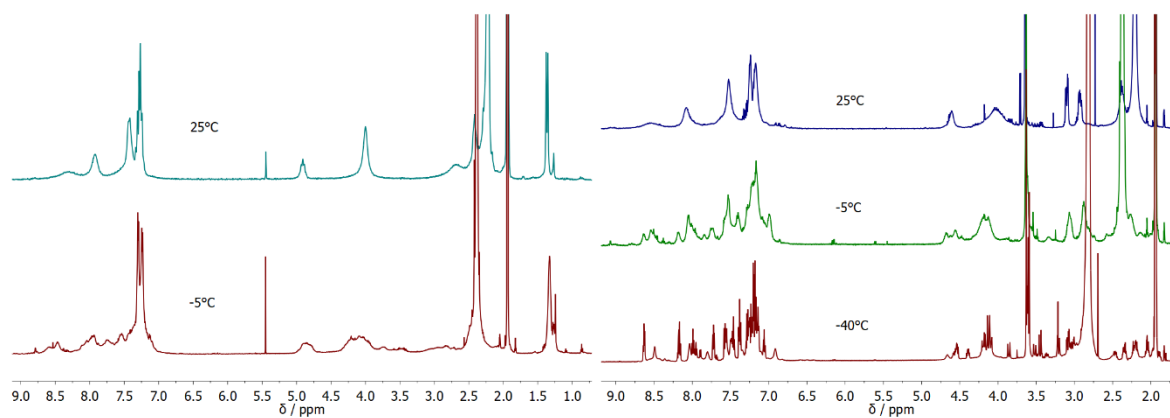


Figure S69. VT ^1H NMR (acetonitrile- d_3) of \mathbf{b}_{2a} (left) and \mathbf{b}_{2b} (right) with 0.5 equiv. Zn(II)

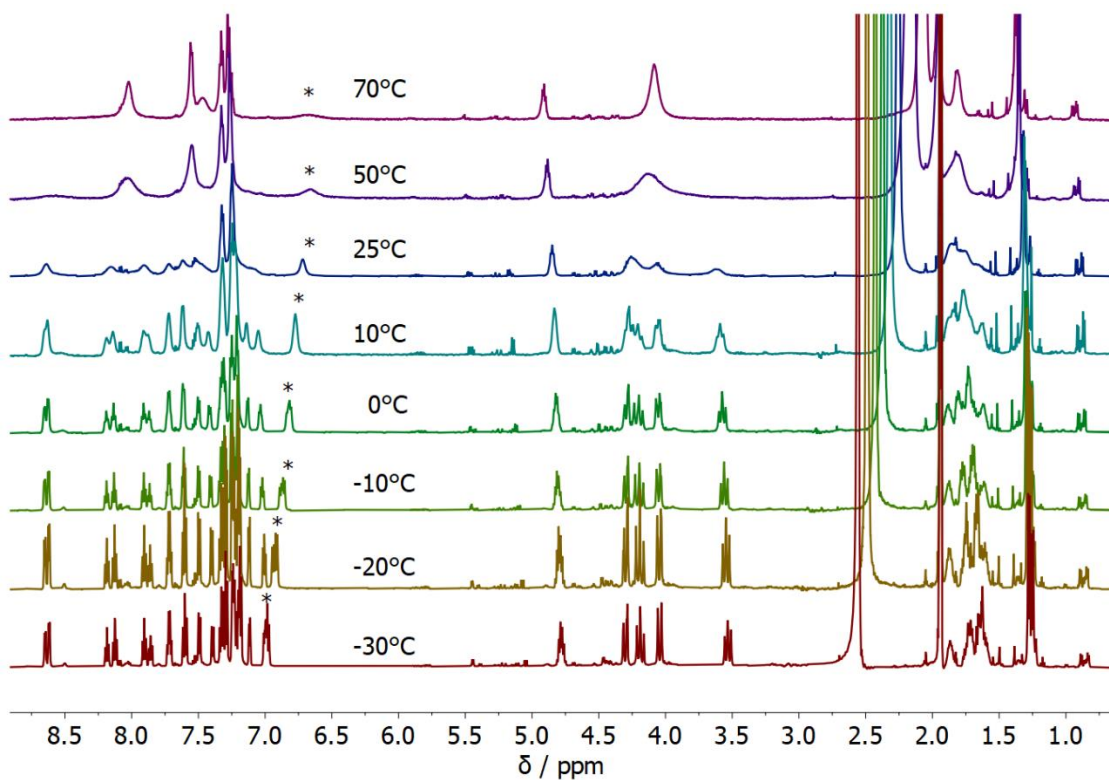


Figure S70. VT ^1H NMR (acetonitrile- d_3) of **b3A** with 0.5 equiv. Zn(II), $c(\text{L}) = 10.9$ mM. Side chain amide NH protons (*) are accented. A small amount of free ligand is observed with a pyridine peak at 8.50 ppm.

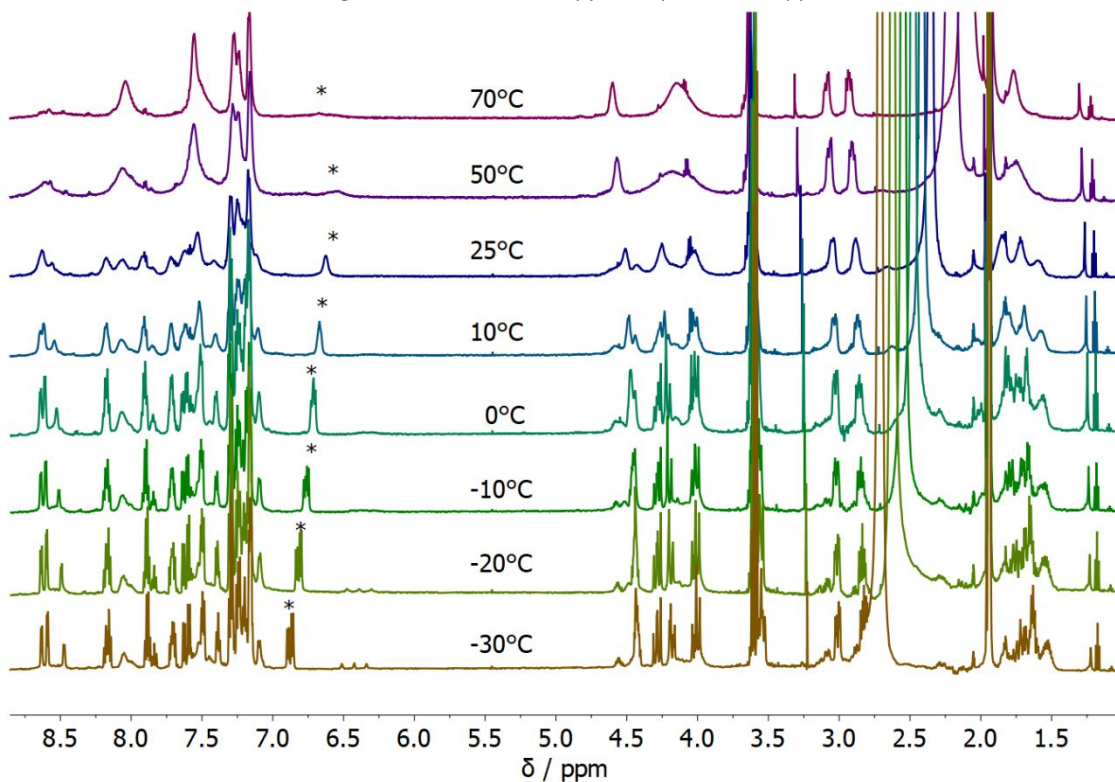


Figure S71. VT ^1H NMR (acetonitrile- d_3) of **b3B** with 0.5 equiv. Zn(II), $c(\text{L}) = 11.6$ mM. Side chain amide NH protons (*) are accented. A small amount of free ligand is observed with a pyridine peak at 8.47 ppm.

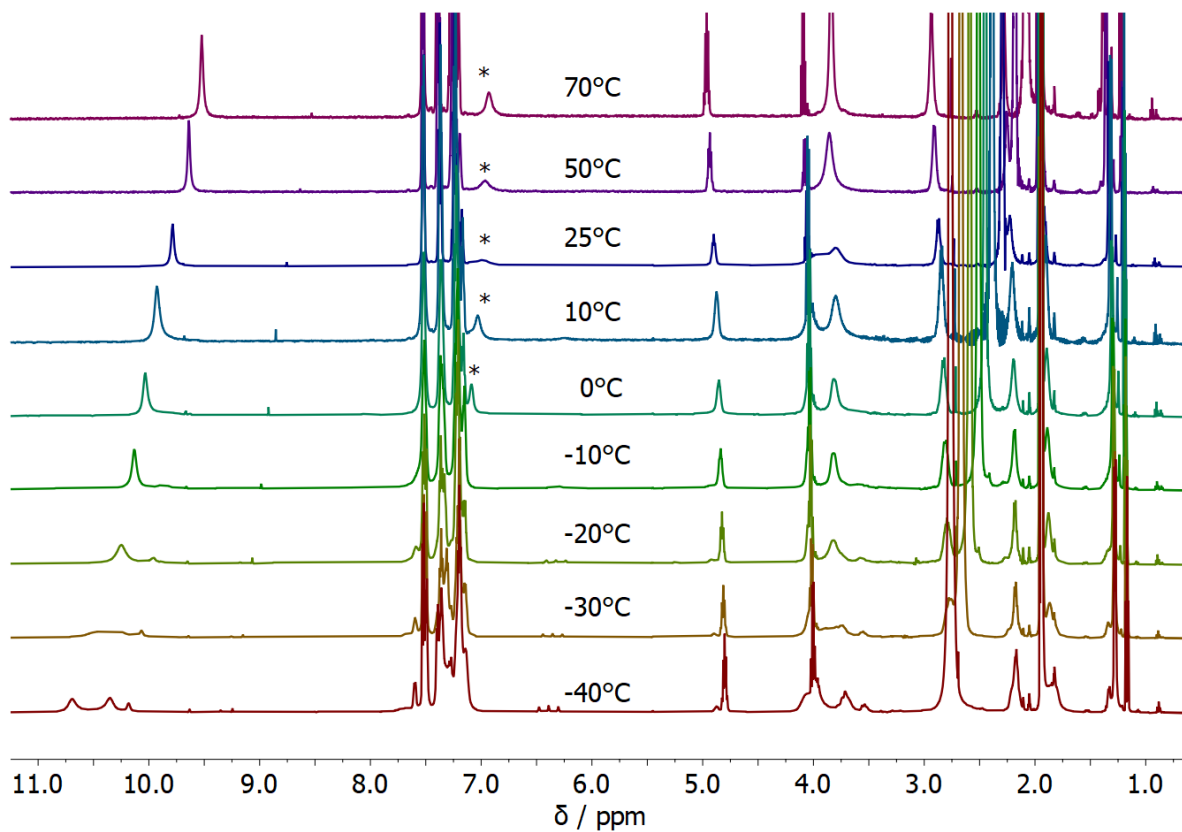


Figure S72. VT ^1H NMR (acetonitrile- d_3) of **i3A** with 0.5 equiv. Zn(II), $c(\text{L}) = 14.6$ mM. Side chain amide NH protons (*) are accented.

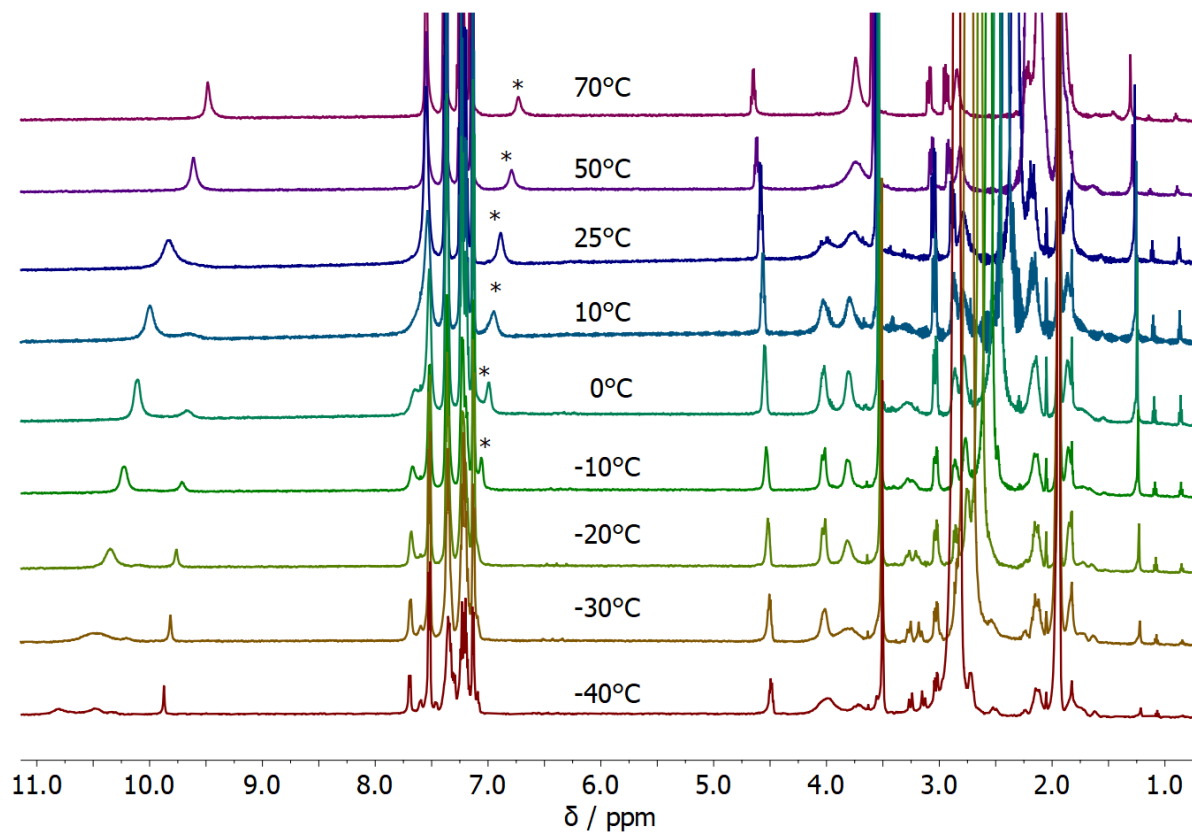


Figure S73. VT ^1H NMR (acetonitrile- d_3) of **i3B** with 0.5 equiv. Zn(II), $c(\text{L}) = 5.0$ mM. Side chain amide NH protons (*) are accented.

8.5 ^{13}C APT NMR spectra of complexes at a L : Zn(II) ratio of 2 : 1

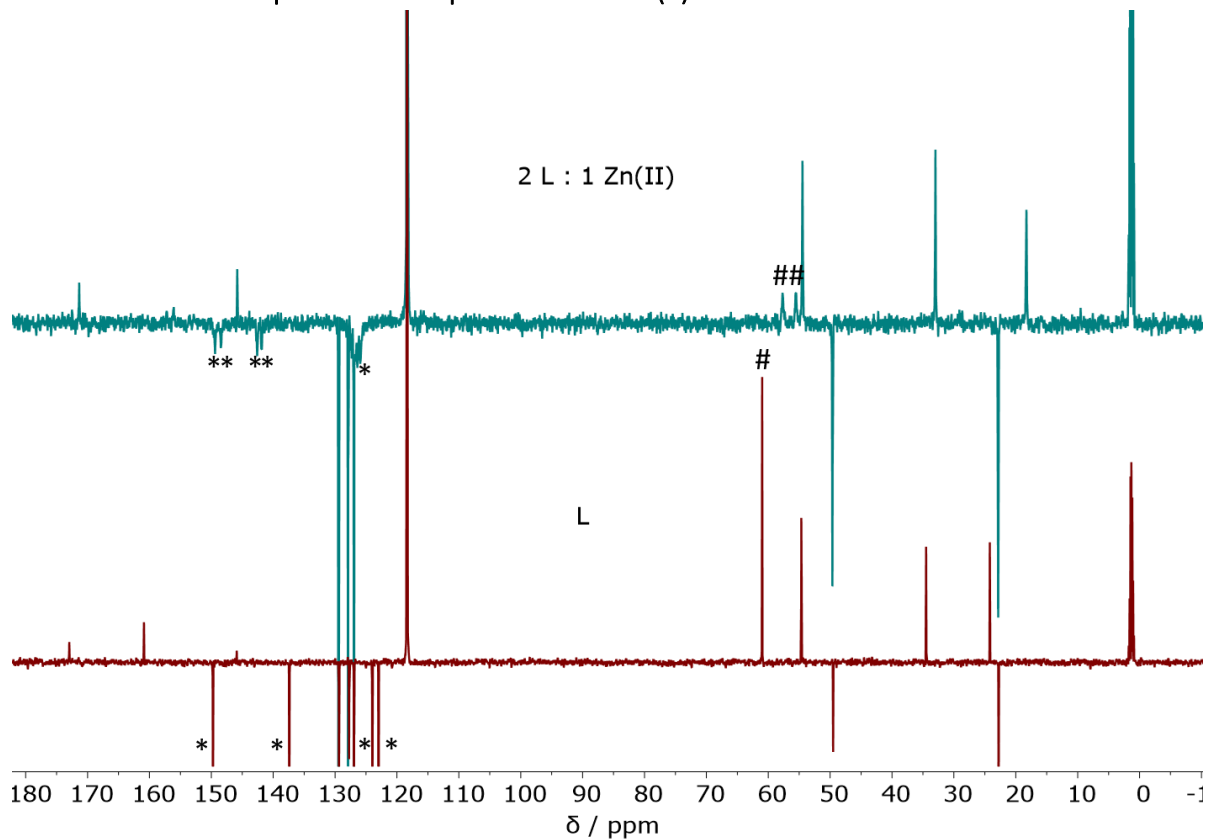


Figure S74. ^{13}C APT (acetonitrile- d_3) spectra of L and ML_2 for ligand **b3A**. Pyridyl (*) and chelator methylene (#) carbons are accented.

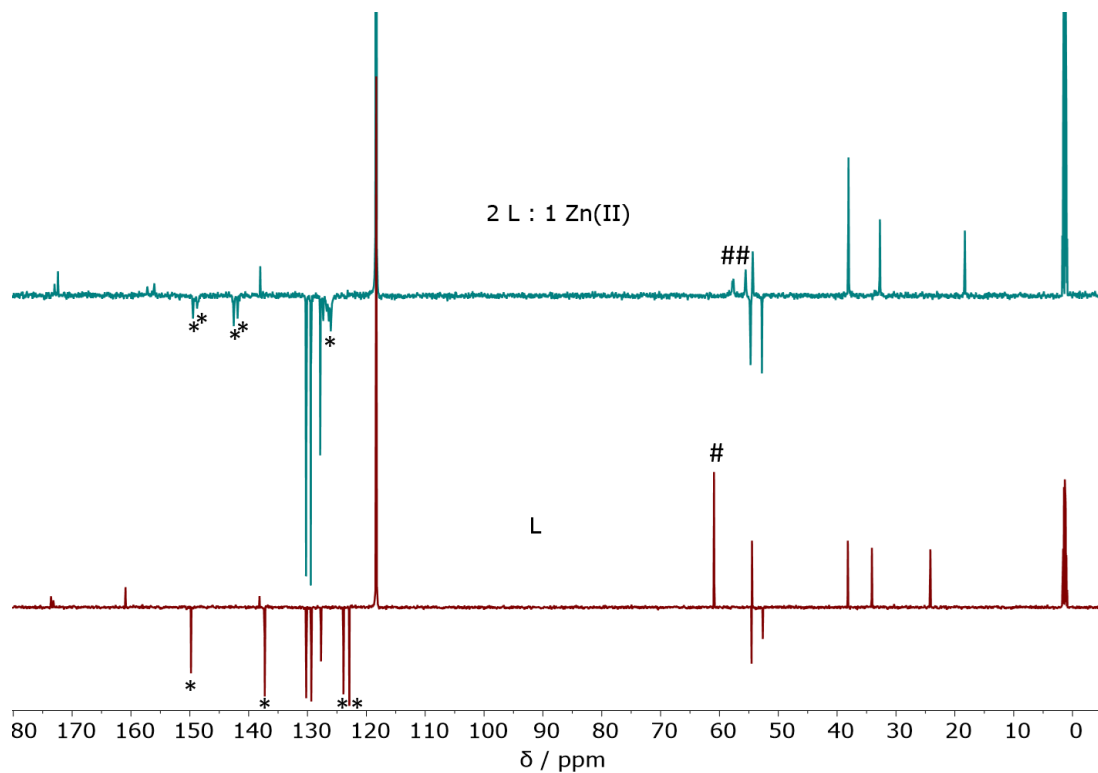


Figure S75. ^{13}C APT (acetonitrile- d_3) spectra of L and ML_2 for ligand **b3B**. Pyridyl (*) and chelator methylene (#) carbons are accented.

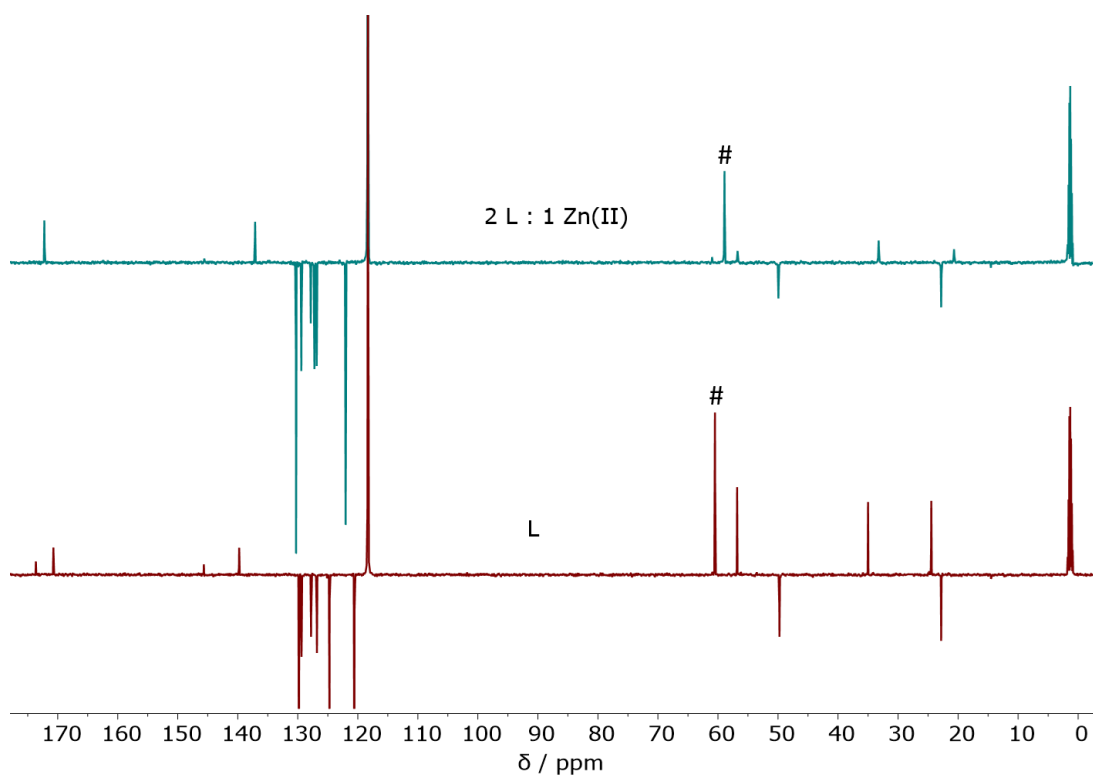


Figure S76. ^{13}C APT ($\text{acetonitrile-}d_3$) spectra of L and ML_2 for ligand **i3A**. Chelator methylene (#) carbons are accented.

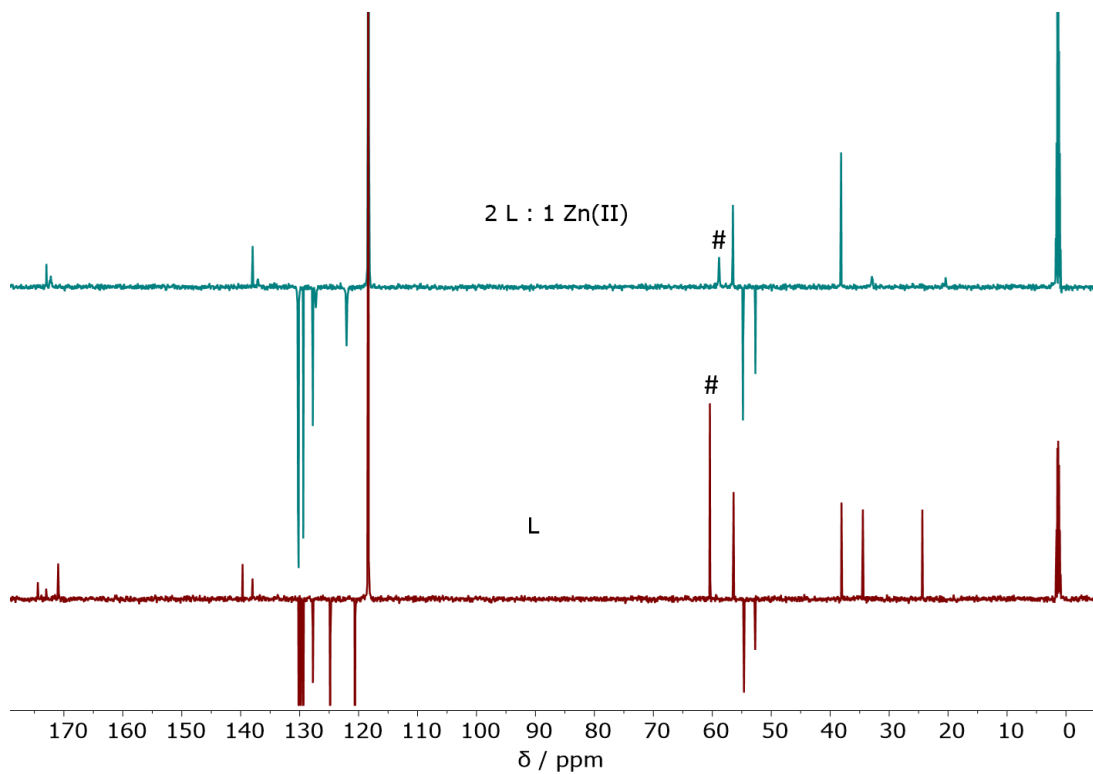


Figure S77. ^{13}C APT ($\text{acetonitrile-}d_3$) spectra of L and ML_2 for ligand **i3B**. Chelator methylene (#) carbons are accented.

9 NMR and UV-Vis measurements in DMSO and water

For these NMR measurements, ML complexes with zinc(II) triflate were prepared in acetonitrile, evaporated to dryness, then dissolved in 30 μL of deuterated DMSO and diluted with 600 μL of D_2O .

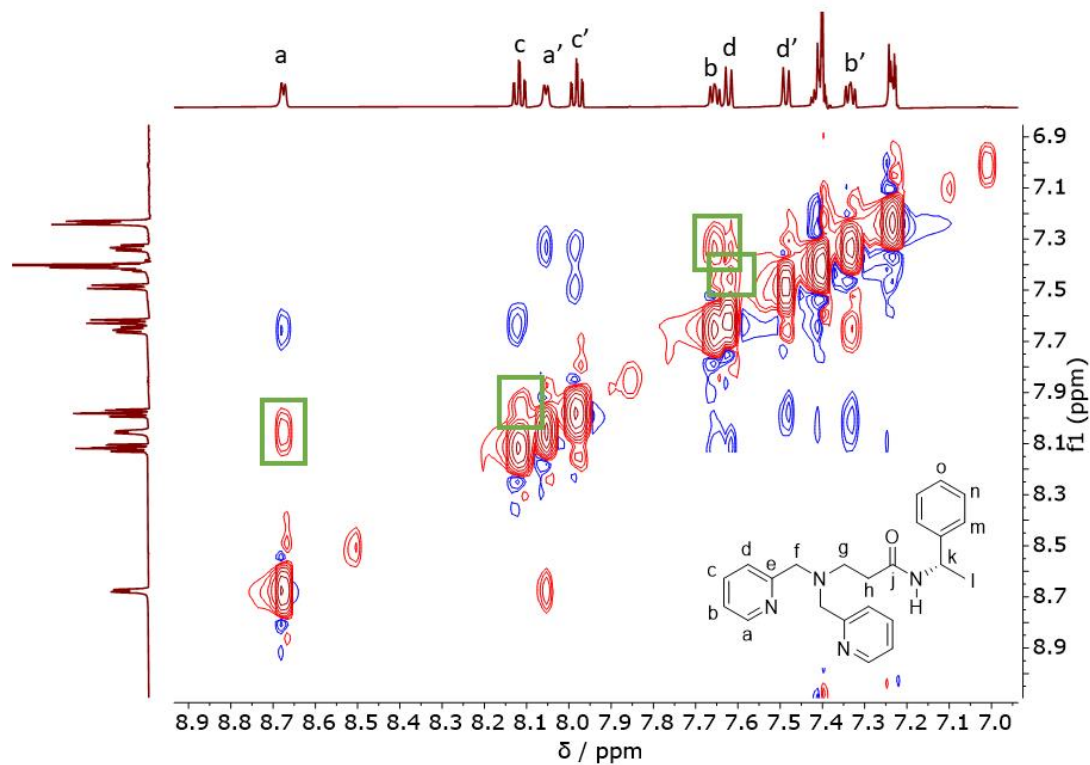


Figure S78. NOESY NMR of ML complex $[\text{Zn}(\text{b2A})]^{2+}$ (D_2O) (aromatic region). Chemical exchange peaks are denoted green.

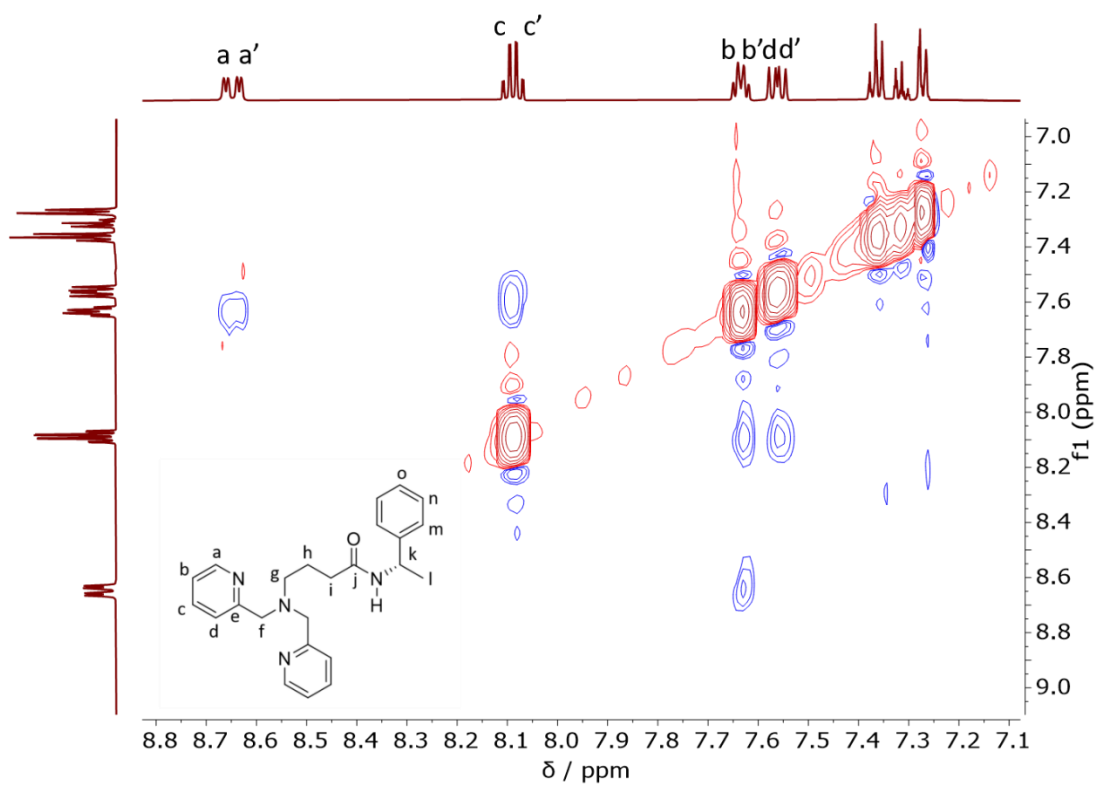


Figure S79. NOESY NMR of ML complex $[Zn(b3A)]^{2+}$ (D_2O) (aromatic region).

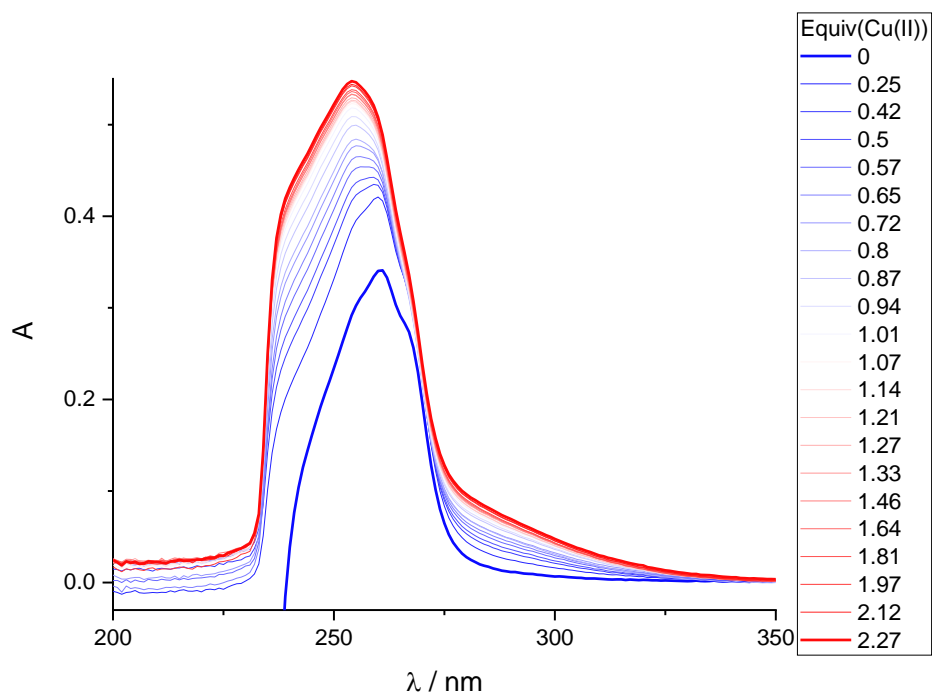


Figure S80. UV-Vis titration of **b2A** (57.1 μM) with CuCl_2 in a 20:1 water : DMSO mixture.

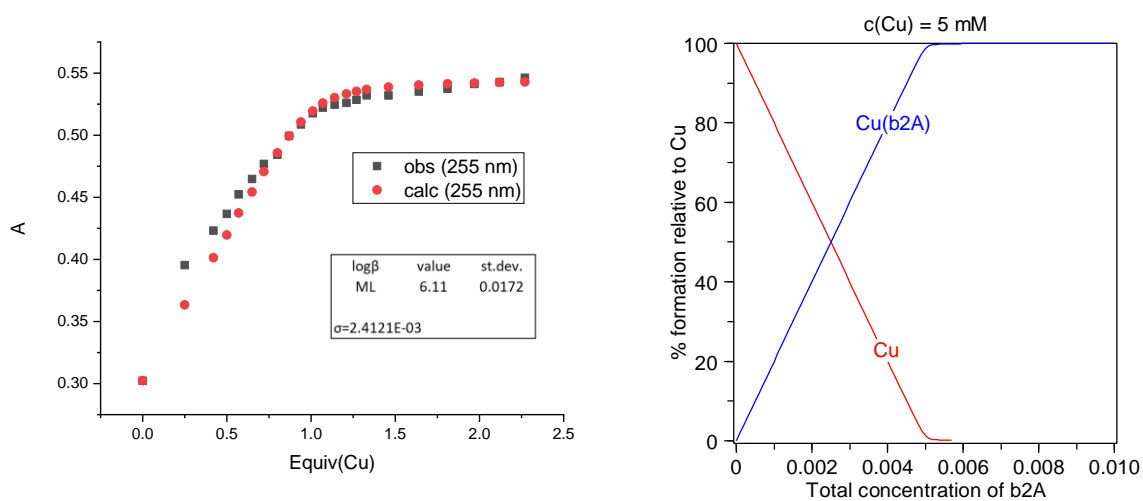


Figure S81. Curve fitting and species distribution for the titration of **b2A** (57.1 μM) with CuCl_2 in a 20:1 water : DMSO mixture. The species distribution is shown for 5 mM concentration of CuCl_2 as was used in the DNA cleavage experiments.

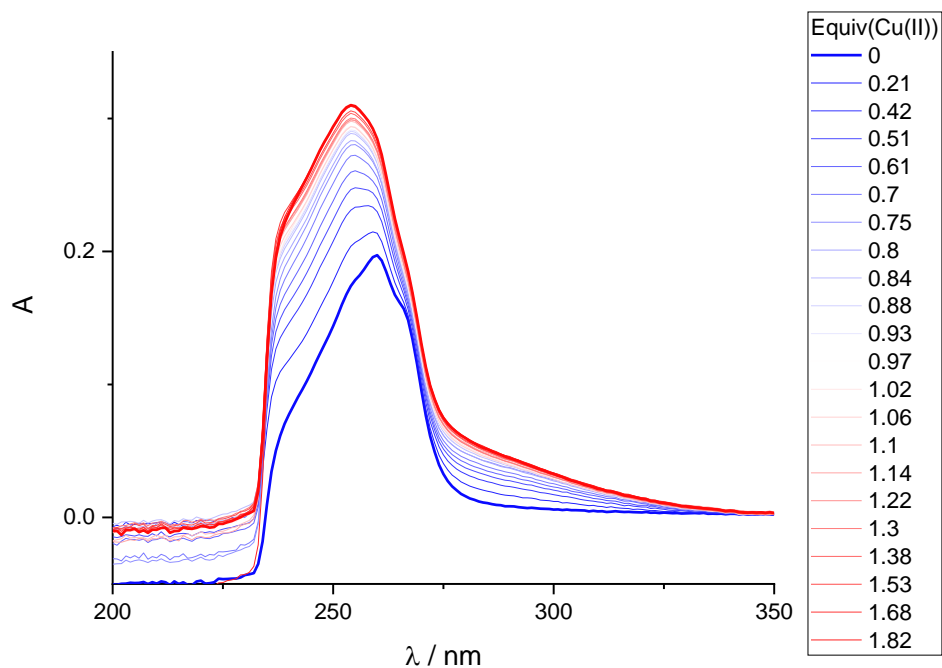


Figure S82. UV-Vis titration of **b3A** (28.6 μM) with CuCl_2 in a 20:1 water : DMSO mixture.

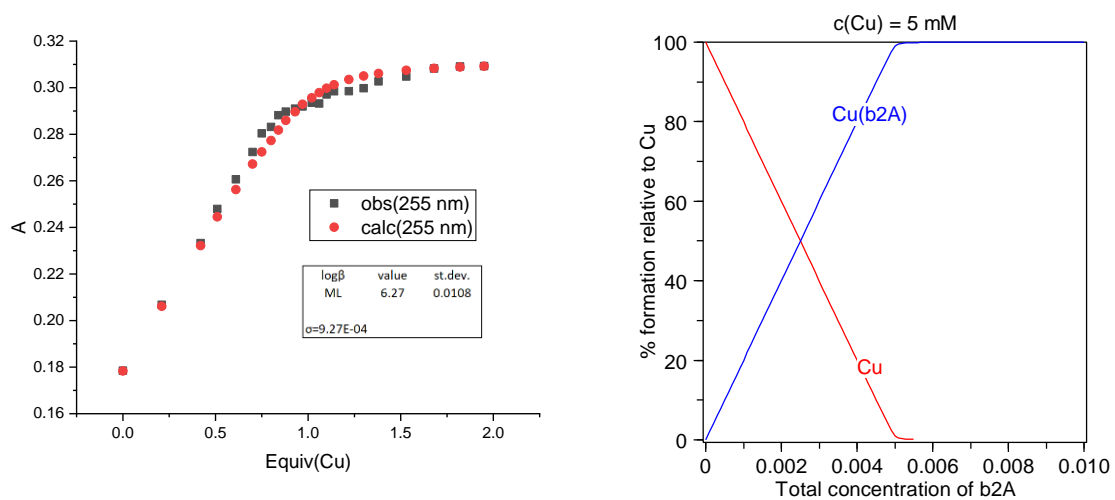
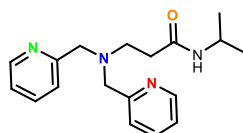
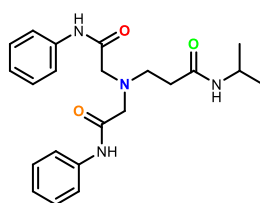
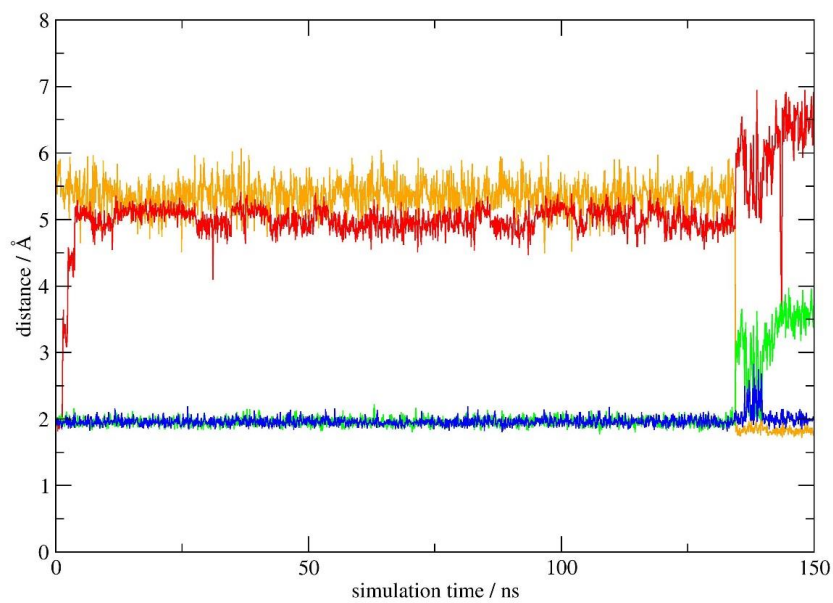


Figure S83. Curve fitting and species distribution for the titration of **b3A** (28.6 μM) with CuCl_2 in a 20:1 water : DMSO mixture. The species distribution is shown for 5 mM concentration of CuCl_2 as was used in the DNA cleavage experiments.

10 Computational analysis



b2A' ligand



i2A' ligand

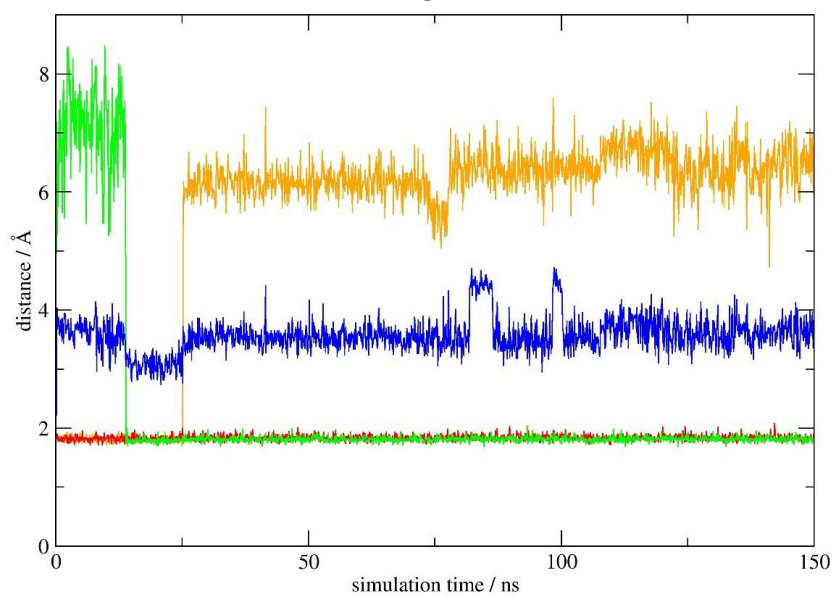


Figure S84. Evolution of distances between selected ligand atoms and Zn(II) cation in the matching ML complexes in the acetonitrile solution during MD simulations. In both cases, Cl⁻ anions are used as counterions, which both coordinate Zn(II) cations during simulations.

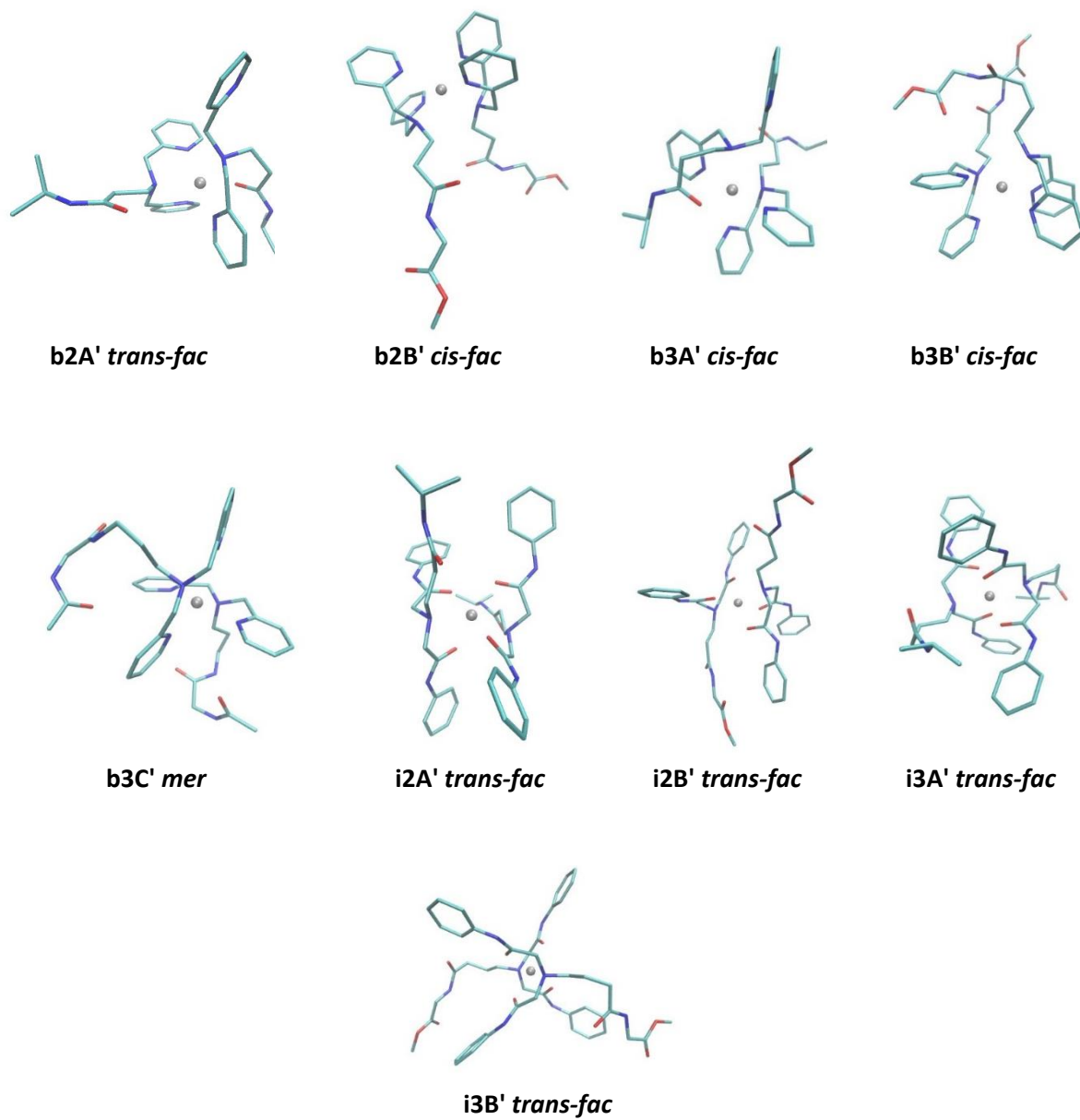


Figure S85. Structures of the most stable ML_2 isomers involving Zn(II) cations and selected ligands as obtained by the (SMD)/M05-2X/6-31+G(d)/LanL2DZ+ECP model.

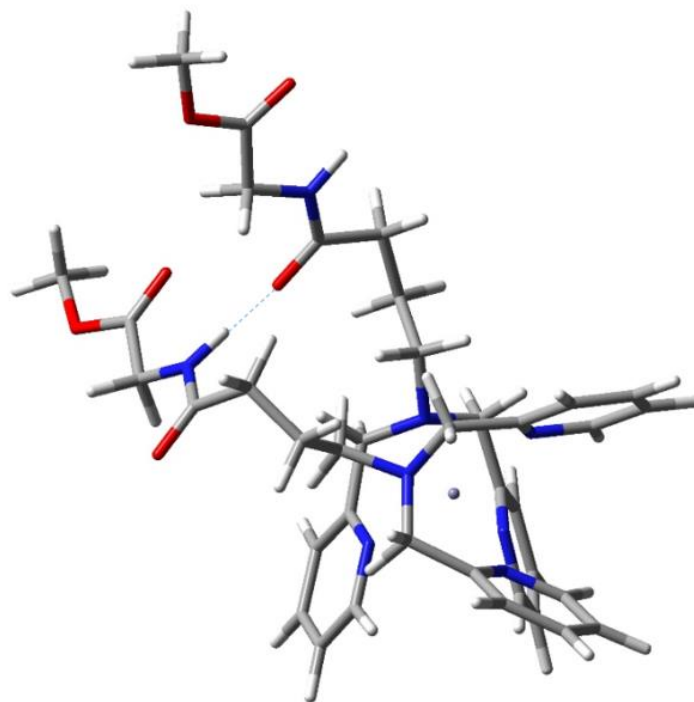


Figure S86. Optimized structure of the *cis-fac* $[\text{Zn}(\mathbf{b3B}')_2]^{2+}$ complex with the indicated hydrogen bonding contact among the side chain amide groups as obtained by the (SMD)/M05-2X/6-31+G(d)/LanL2DZ+ECP model. During MD simulations, these hydrogen bonding interactions are recorded in 18% of the simulation structures.

11 DNA cleavage

Acetonitrile and *N,N*-dimethylformamide were tested as weakly coordinating solvents^{7,8} for preparation of stock solutions, but retention of the reaction mixture in the gel was observed in these experiments. Therefore, DMSO was used for the preparation of stock solutions.

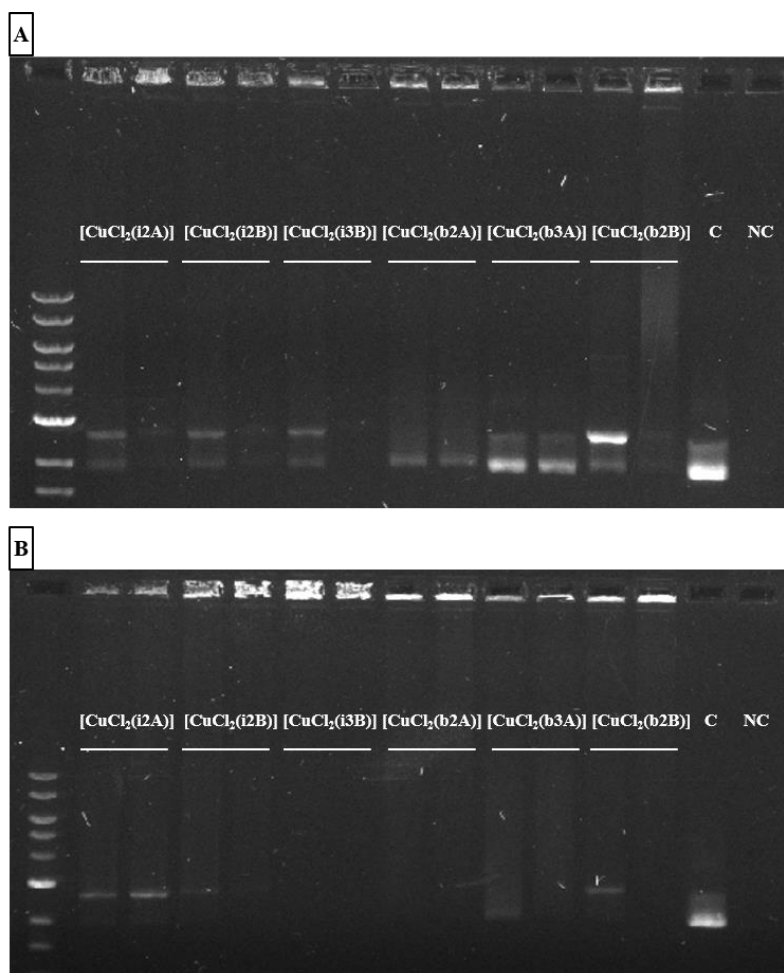


Figure S87. **(A)** Agarose gel (0.5% in TAE buffer) electrophoresis patterns of pUC19 DNA (20 ng/ μ L) incubated with designated complexes dissolved in acetonitrile in 2.5 (first lane) and 5 mM (second lane) concentrations. C1 represents the native pUC19 plasmid incubated in reaction buffer; NC represents the reaction buffer alone. **(B)** Agarose gel (0.5% in TAE buffer) electrophoresis patterns of pUC19 DNA (20 ng/ μ L) incubated with designated complexes dissolved in *N,N*-dimethylformamide (DMF) at 2.5 and 5 mM concentrations. C represents the native pUC19 plasmid incubated in reaction buffer; NC represents the reaction buffer alone; all samples were incubated for 1 h at 37 °C.

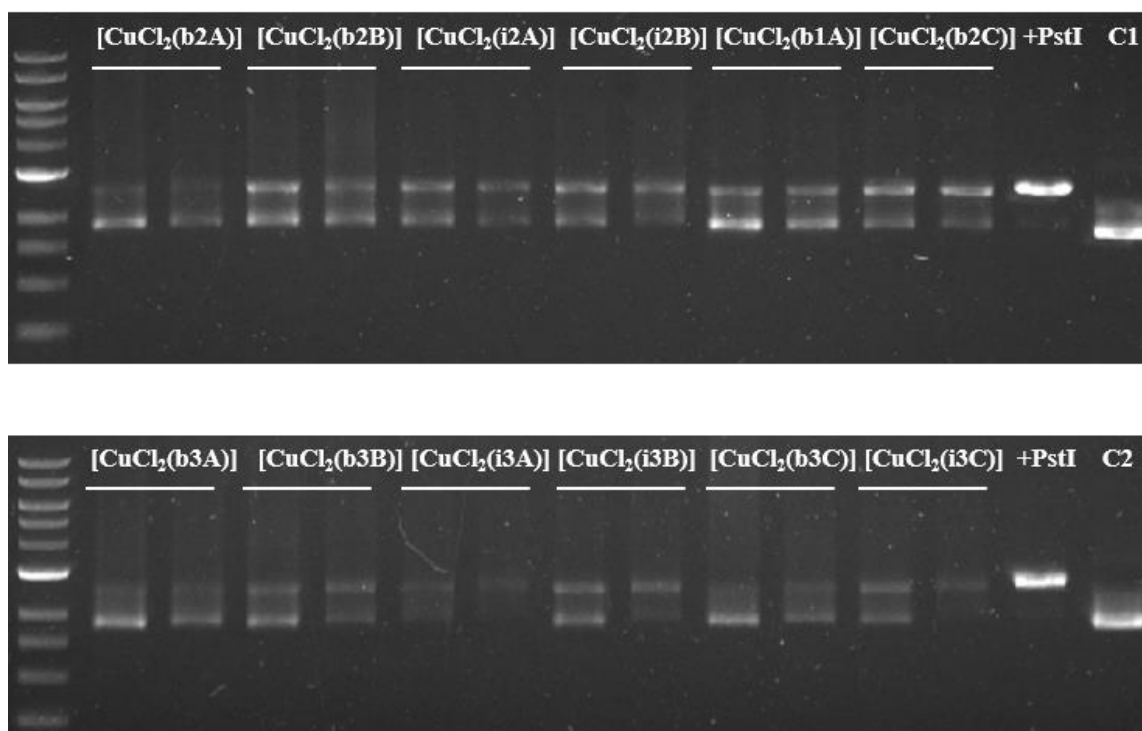


Figure S88. Agarose gel (0.5% in TAE buffer) showing cleavage of pUC19 DNA (20 ng/ μ L) incubated with 2.5 (first lane) and 5 mM (second lane) complexes **[CuCl₂(b2A)]** - **[CuCl₂(i3C)]** in 25 mM Tris buffer/50 mM NaCl, pH 7.4. DNA ladder with a distinct high intensity band of 3 kb is followed by reactions of pUC19 with the complexes, followed by control reactions; +PstI reaction represents the native pUC19 plasmid linearized by PstI endonuclease; C1 represents the native pUC19 plasmid incubated with reaction buffer and complex solvent (DMSO); C2 represents the native pUC19 plasmid incubated with reaction buffer and [CuCl₂]; all samples were incubated for 1 h at 37°C.

In reactions with the tested complexes, most prominent examples being plasmid DNA incubations with **[CuCl₂(i3A)]** and **[CuCl₂(i3C)]**, the intensity of the supercoiled DNA bands was diminished without a significant increase in the linear DNA portion, with visible smears of DNA (Figure S83). Such smears have been observed in literature and are attributed to unwinded and partially unwinded plasmid conformations due to DNA charge neutralization, covalent DNA cross-linking, or both effects combined, resulting in conformational changes, as well as to the possibility of degradation of all DNA forms to smaller fragments.⁸⁻¹⁰

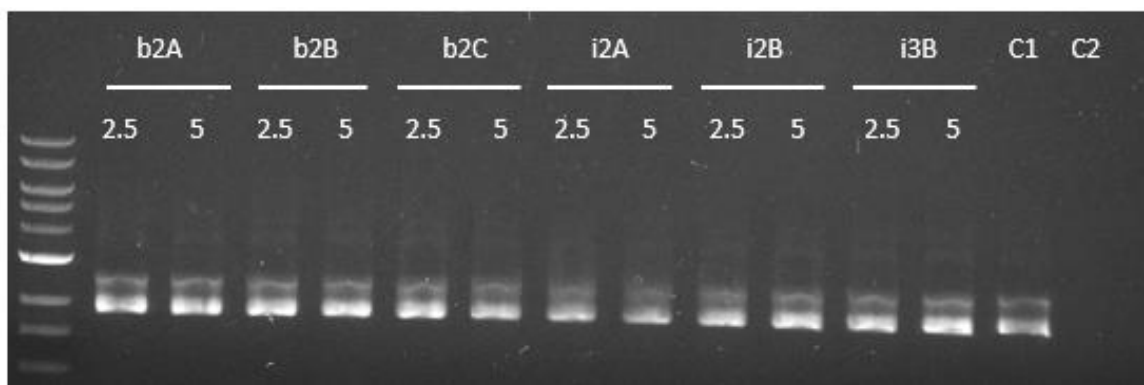


Figure S89. Agarose gel (0.5% in TAE buffer) electrophoresis patterns of pUC19 DNA (20 ng/ μ L) incubated with 2.5 mM and 5 mM of selected bpa and imda ligands in 25 mM Tris buffer/50 mM NaCl, pH 7.4. C1 - native pUC19 plasmid in reaction buffer, C2 – blank reaction buffer; all samples were incubated for 1 h at 37°C.

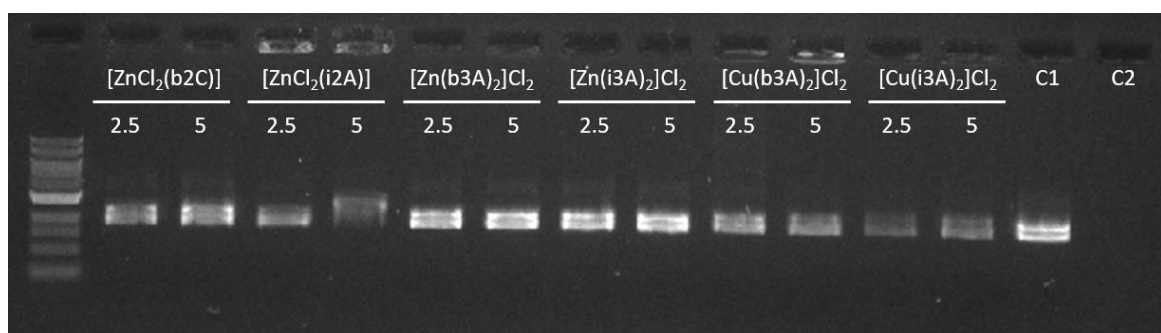


Figure S90. Agarose gel (0.5% in TAE buffer) electrophoresis patterns of pUC19 DNA (20 ng/ μ L) incubated with 2.5 mM and 5 mM of selected metal complexes in 25 mM Tris buffer/50 mM NaCl, pH 7.4. C1 - native pUC19 plasmid in reaction buffer, C2 – blank reaction buffer; all samples were incubated for 1 h at 37°C. Retention of the reaction mixture in the gel was observed for [ZnCl₂(i2A)] and [Cu(i3A)₂]Cl₂, possibly due to precipitation of the complex in the reaction buffer.

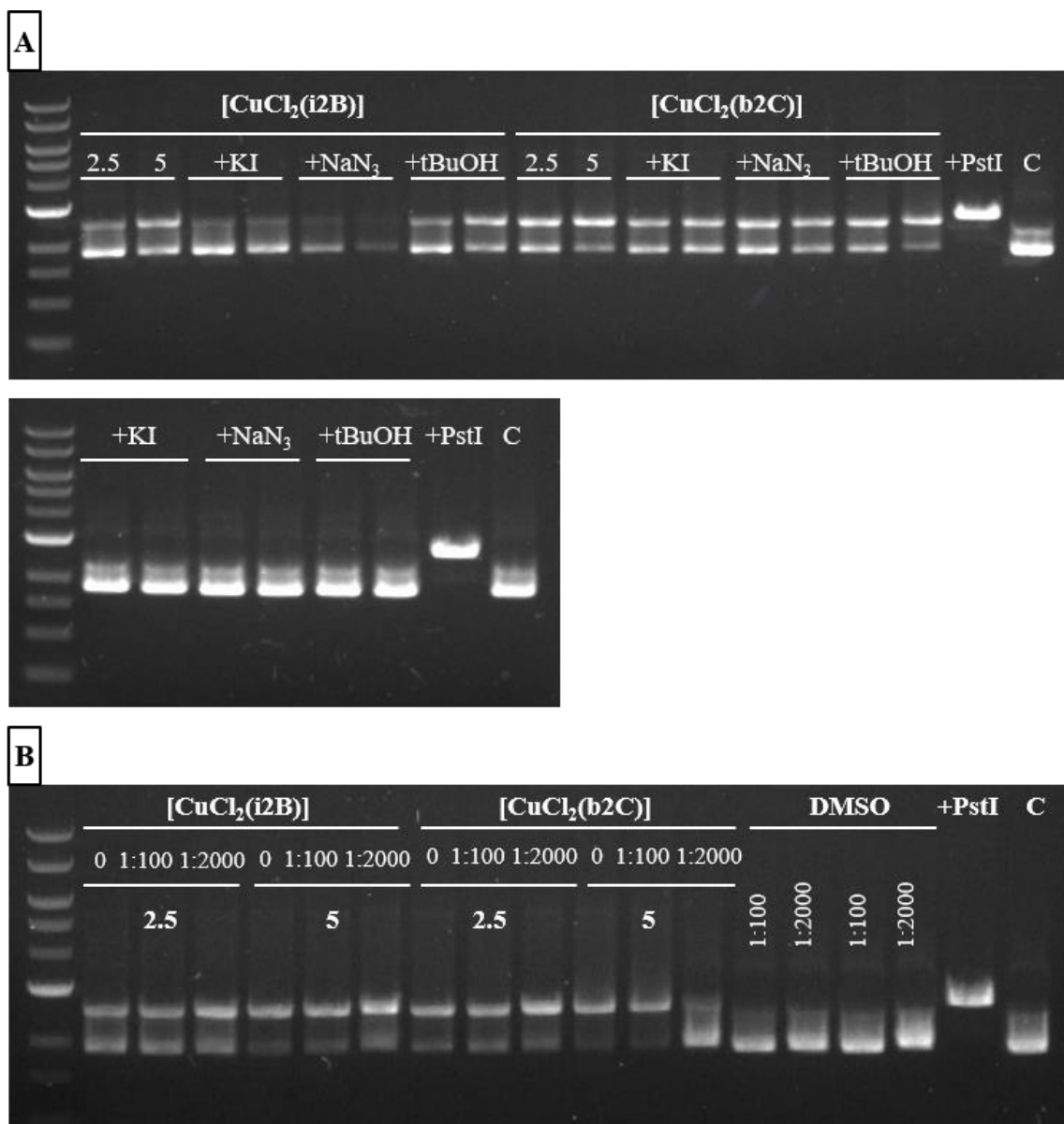


Figure S91. **(A)** Agarose gel (0.5% in TAE buffer) electrophoresis patterns of pUC19 DNA (20 ng/ μ L) incubated with 2.5 and 5mM complexes **[CuCl₂(i2B)]** and **[CuCl₂(b2C)]**, followed by electrophoresis patterns of the same reactions with the addition of different radical scavengers (KI, NaN₃ and tBuOH) in equimolar ratios to the complexes (1:1). +PstI reaction represents the native pUC19 plasmid linearized by PstI endonuclease. C represents the native pUC19 plasmid incubated in reaction buffer. The lower gel shows electrophoresis patterns of pUC19 DNA (20 ng/ μ L) incubated with radical scavengers (KI, NaN₃ and tBuOH) alone. **(B)** Electrophoresis patterns of pUC19 DNA (20 ng/ μ L) incubated with 2.5 and 5 mM complexes **[CuCl₂(i2B)]** and **[CuCl₂(b2C)]**, followed by electrophoresis patterns of the same reactions with the addition of excess DMSO (1:100 and 1:2000), followed by control reactions with just pUC19 and excess DMSO (1:100 and 1:2000 for both conditions). +PstI reaction represents the native pUC19 plasmid linearized by PstI endonuclease; C represents the native pUC19 plasmid incubated in reaction buffer. All samples were incubated in 25 mM Tris buffer/50 mM NaCl, pH 7.4, for 1 h at 37 °C.

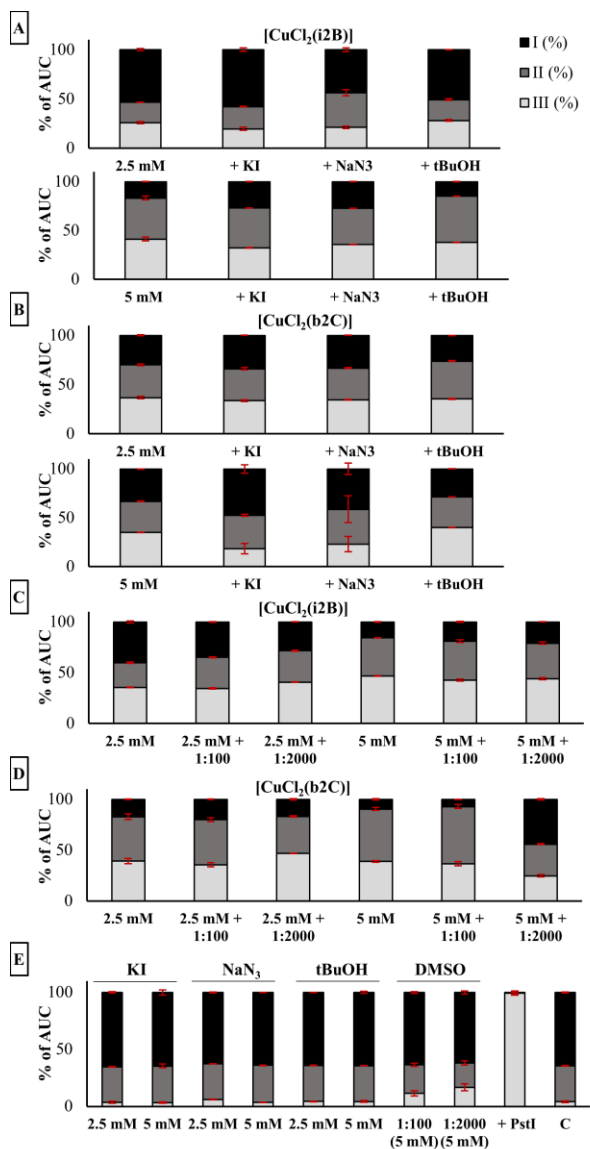


Figure S92. The results of pUC19 DNA cleavage catalyzed by $[\text{Cu}(\text{i}2\text{B})\text{Cl}_2]$ (A) and $[\text{Cu}(\text{b}2\text{C})\text{Cl}_2]$ (B) with the addition of different radical scavengers (KI, NaN_3 and tBuOH) in equimolar ratios (1:1). The results of pUC19 DNA cleavage catalyzed by $[\text{Cu}(\text{i}2\text{B})\text{Cl}_2]$ (C) and $[\text{Cu}(\text{b}2\text{C})\text{Cl}_2]$ (D) with the addition of excess DMSO (1:100 and 1:2000). (E) Control reactions of pUC19 DNA incubated with radical scavengers (KI, NaN_3 , tBuOH, DMSO) alone. +PstI represents the native pUC19 plasmid linearized by PstI endonuclease; C represents the native pUC19 plasmid incubated in the reaction buffer. All samples were incubated in 25 mM Tris buffer/50 mM NaCl, pH 7.4 for 1 h at 37 °C. The representative electrophoresis gels are shown in Figure S84.

12 Characterization of the precursors and ligands

12.1 ^1H NMR spectra of precursors Boc2A-Boc3C:

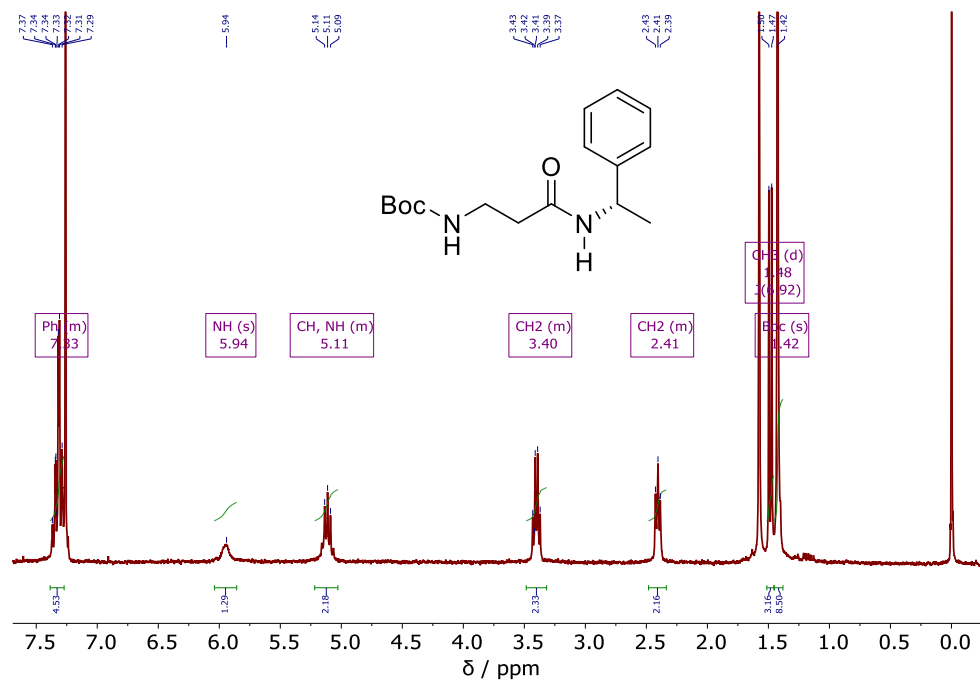


Figure S93. ^1H NMR (300.13 MHz, CDCl_3) of Boc2A

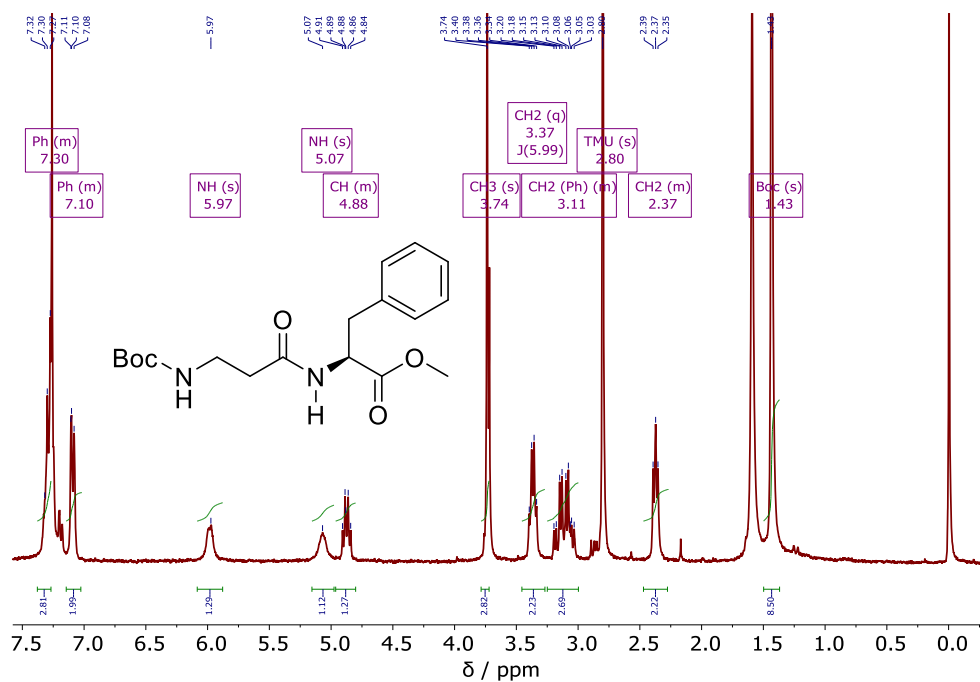


Figure S94. ^1H NMR (300.13 MHz, CDCl_3) of Boc2B

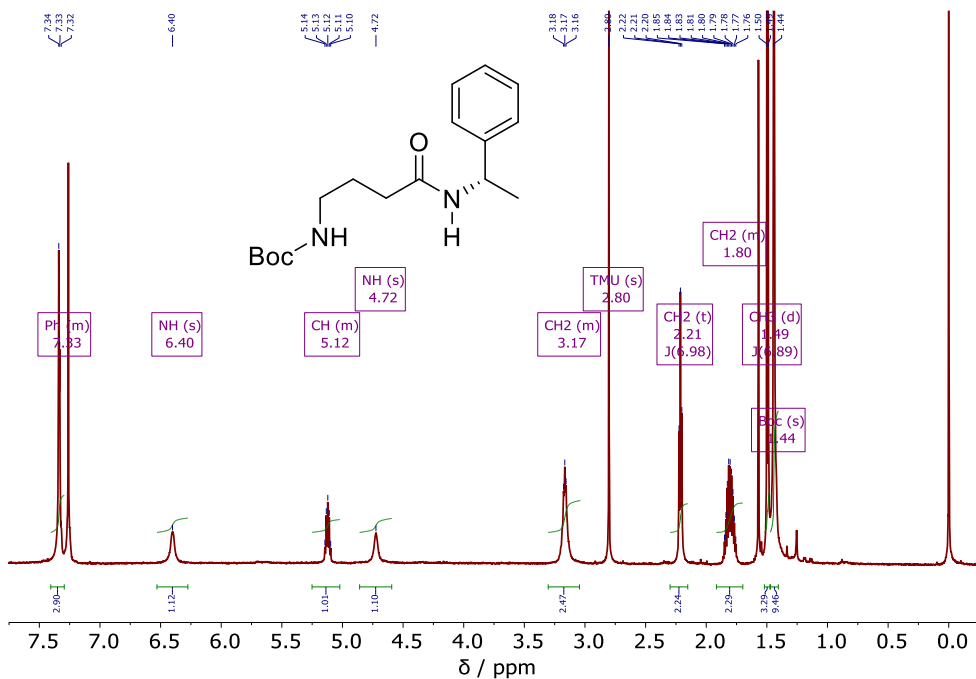


Figure S95. ¹H NMR (600.13 MHz, CDCl₃) of Boc3A

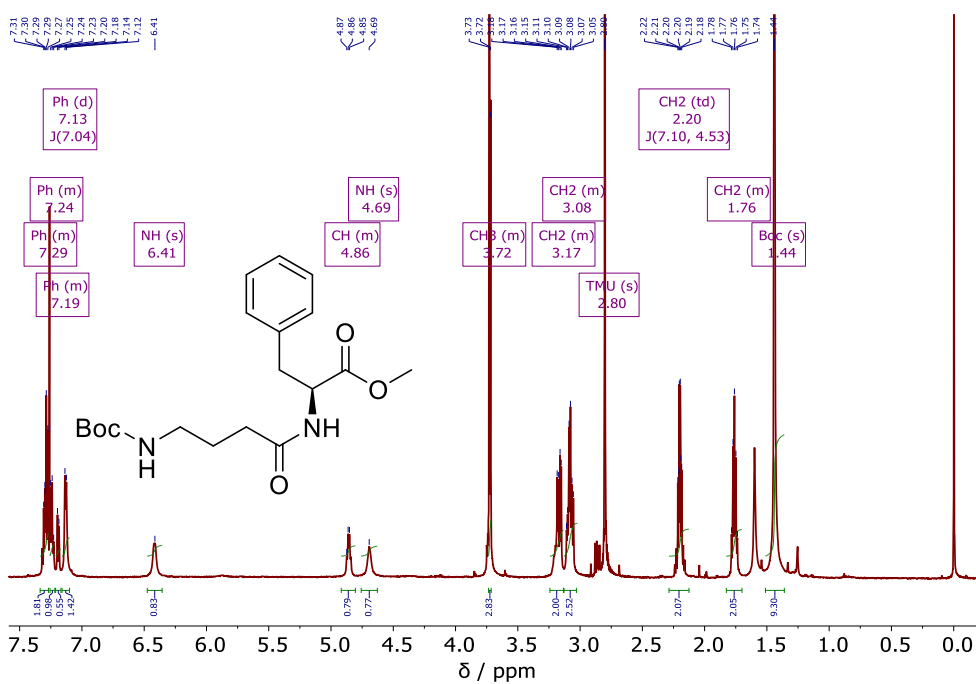


Figure S96. ¹H NMR (600.13 MHz, CDCl₃) of Boc3B

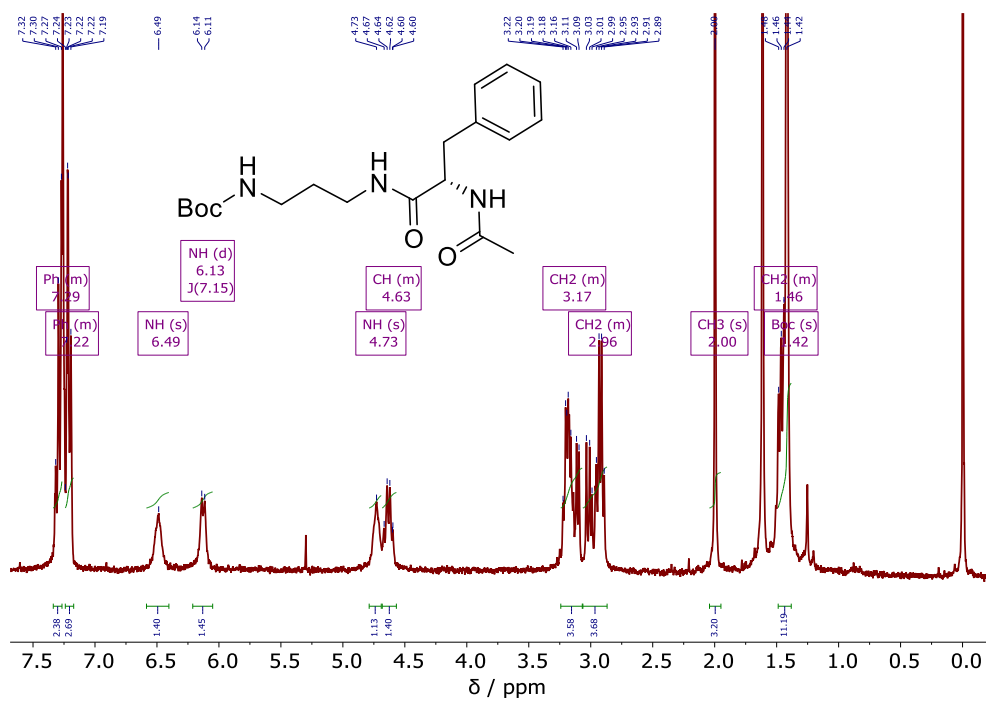


Figure S97. ¹H NMR (300.13 MHz, CDCl₃) of Boc3C

12.2 ¹H and ¹³C NMR spectra of ligands b1A-i3C:

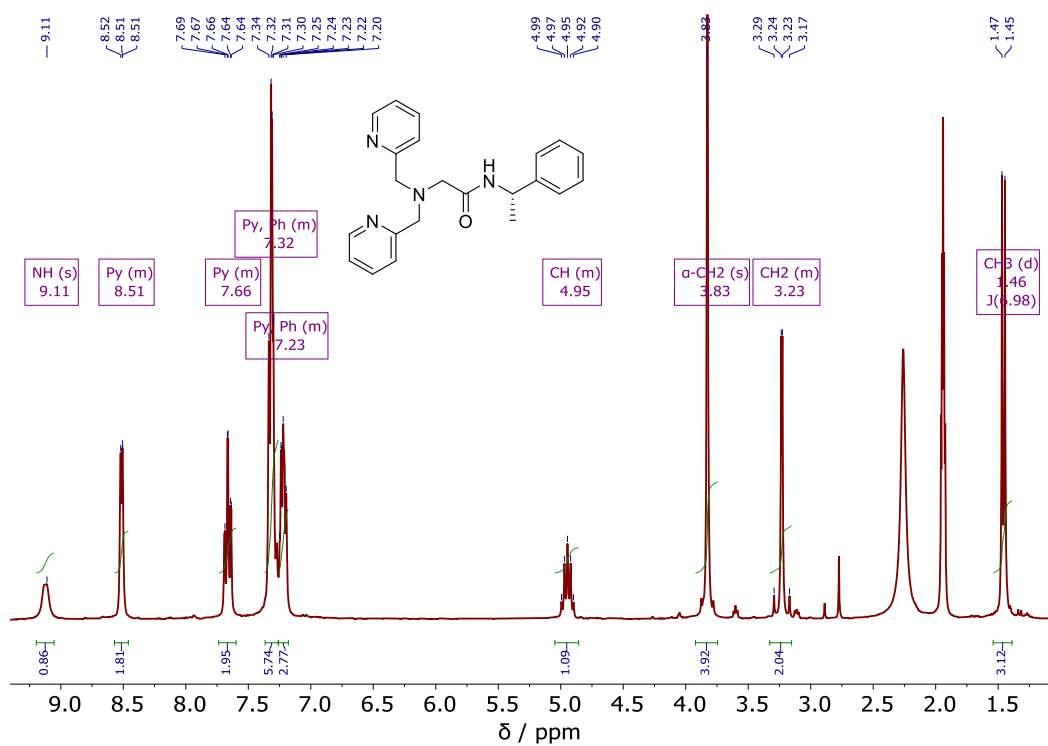


Figure S98. ¹H NMR (300.13 MHz, CD₃CN) of **b1A**

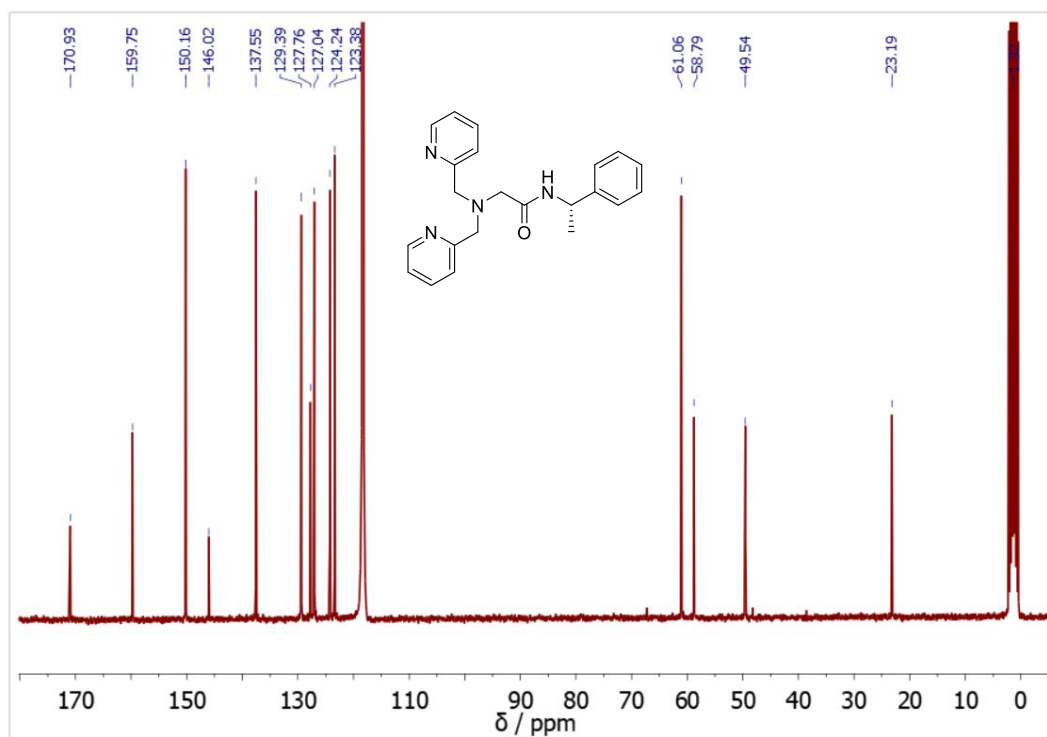


Figure S99. ¹³C NMR (75.47 MHz, CD₃CN) of **b1A**

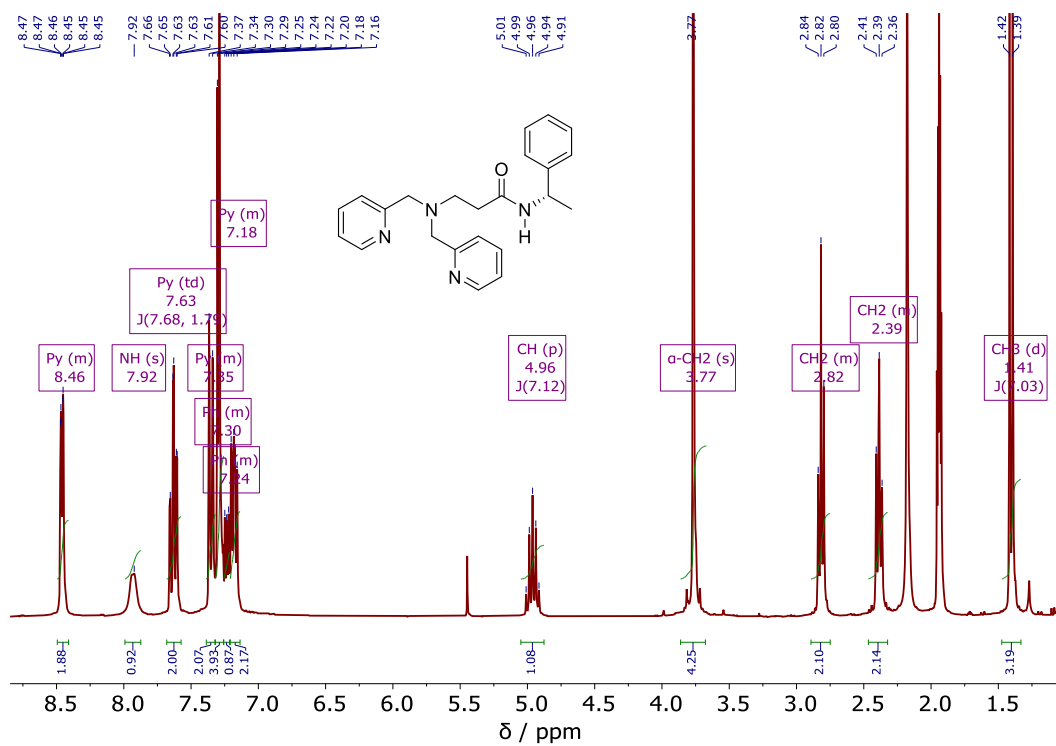


Figure S102. ^1H NMR (300.13 MHz, CD_3CN) of **b2A**

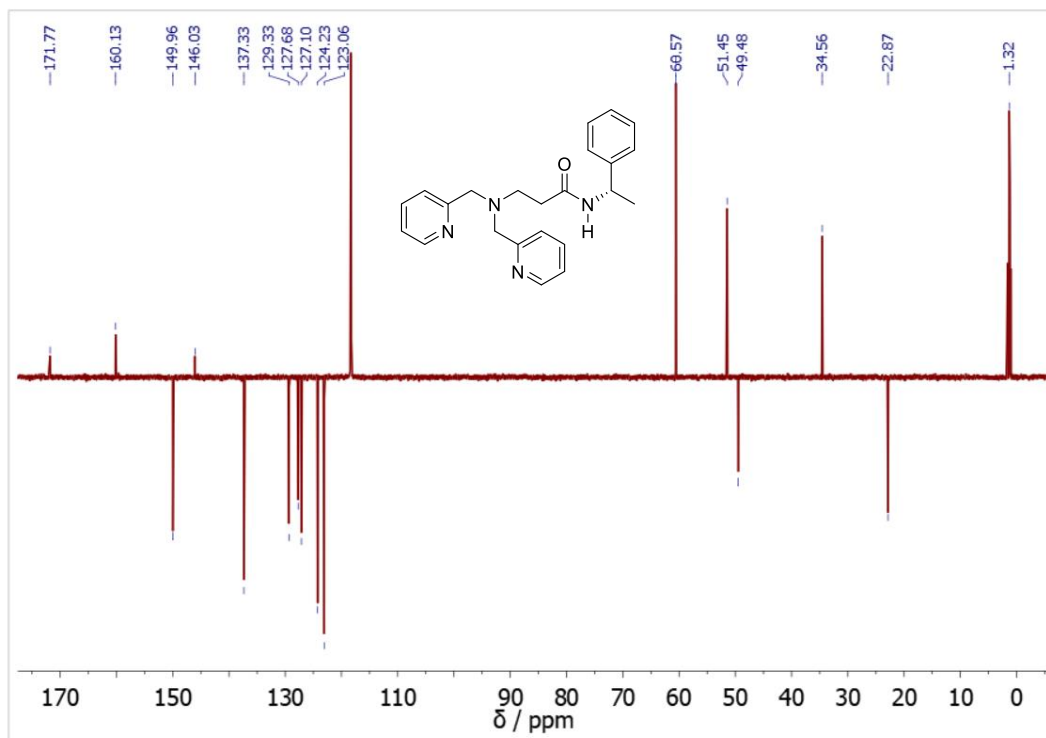


Figure S103. APT ^{13}C NMR (150.90 MHz, CD_3CN) of **b2A**

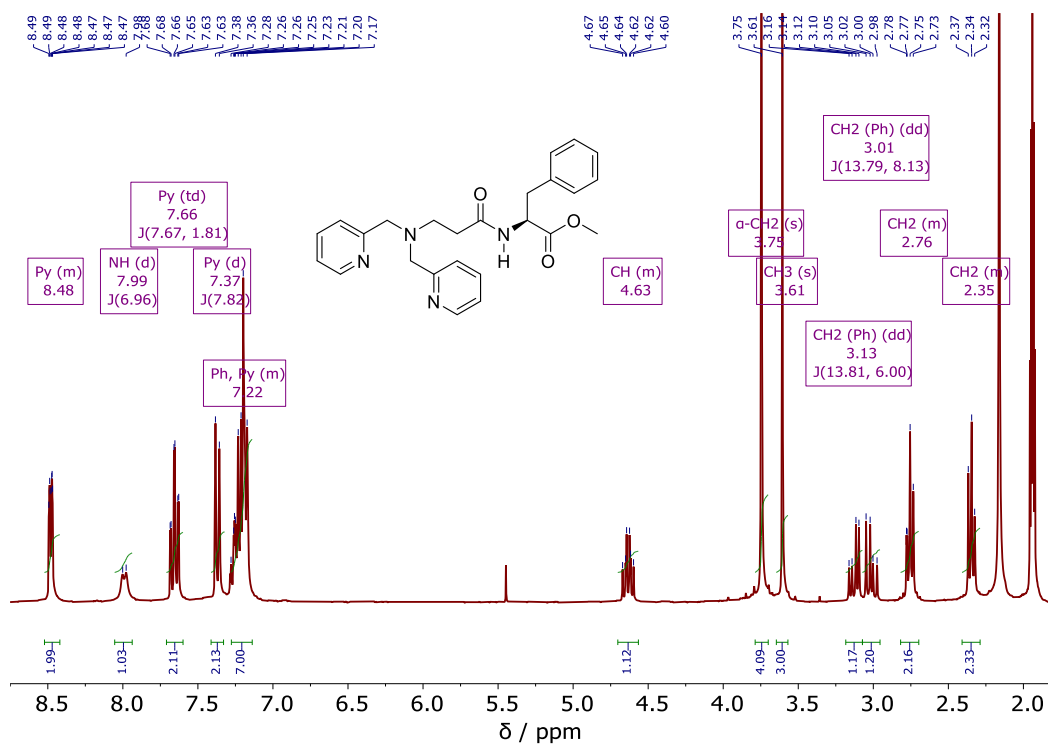


Figure S104. ^1H NMR (300.13 MHz, CD_3CN) of **b2B**

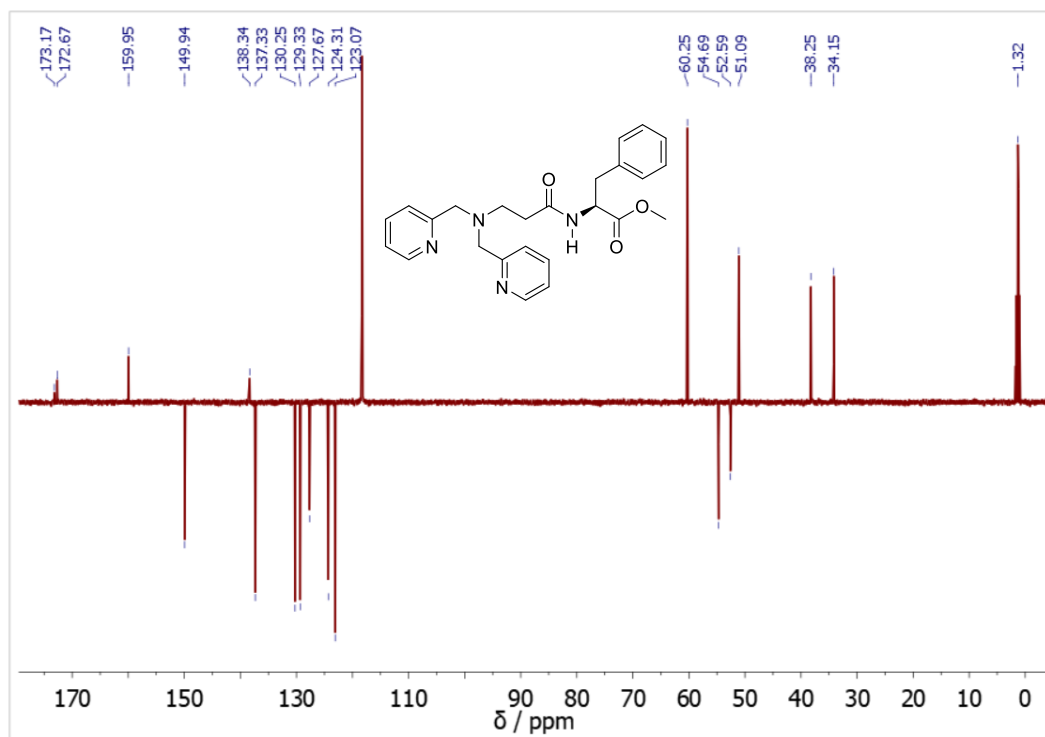


Figure S105. APT ^{13}C NMR (150.90 MHz, CD_3CN) of **b2B**

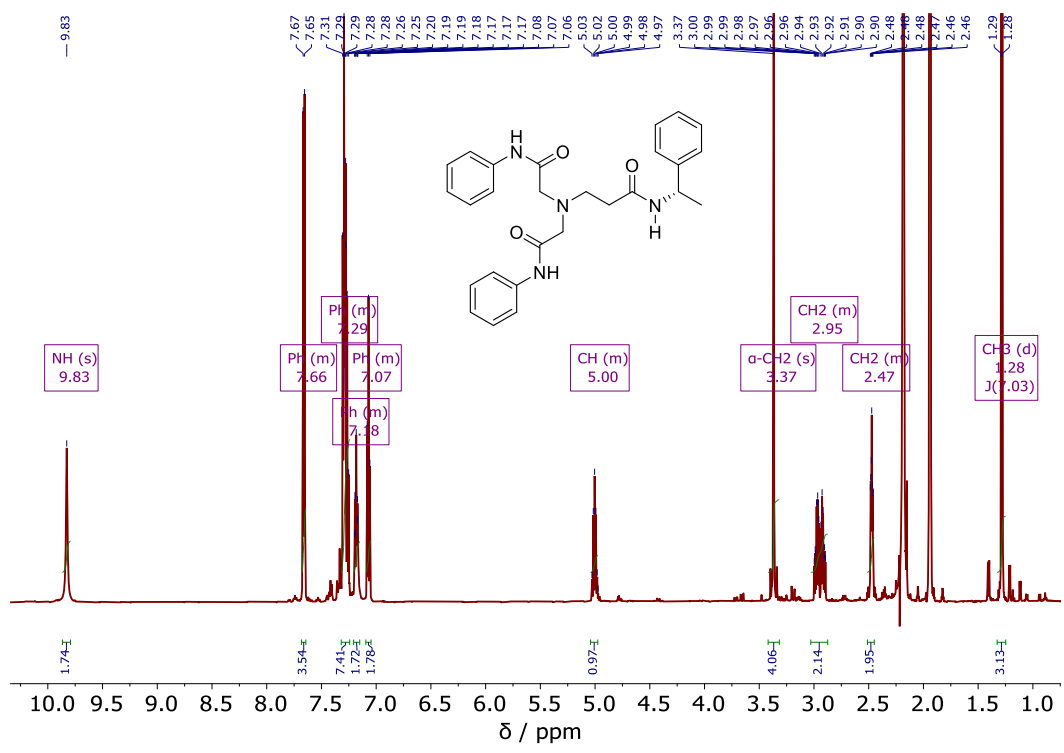


Figure S106. ¹H NMR (600.13 MHz, CD₃CN) of **i2A**

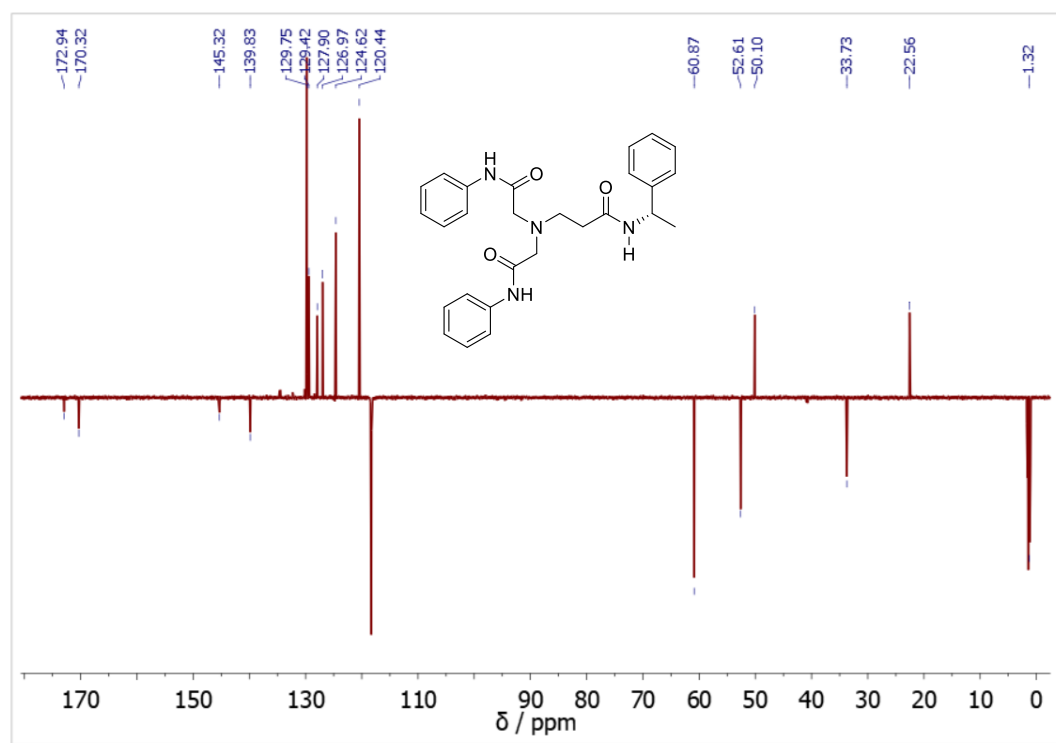


Figure S107. APT ¹³C NMR (150.90 MHz, CD₃CN) of **i2A**

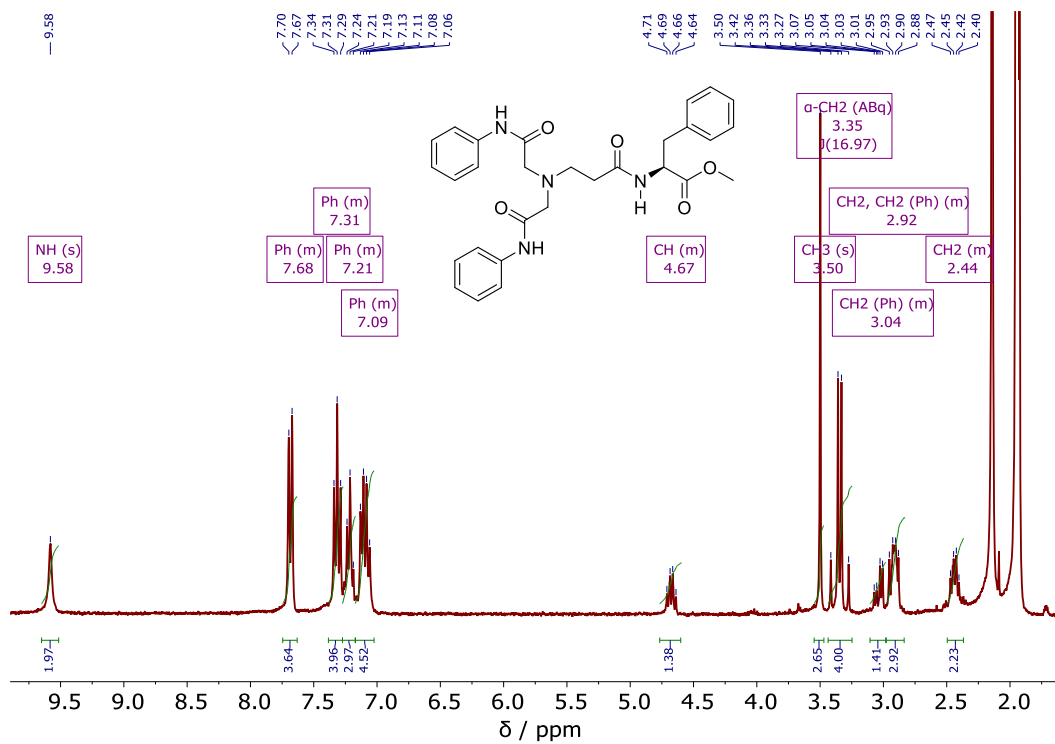


Figure S108. ¹H NMR (300.13 MHz, CD₃CN) of **i2B**

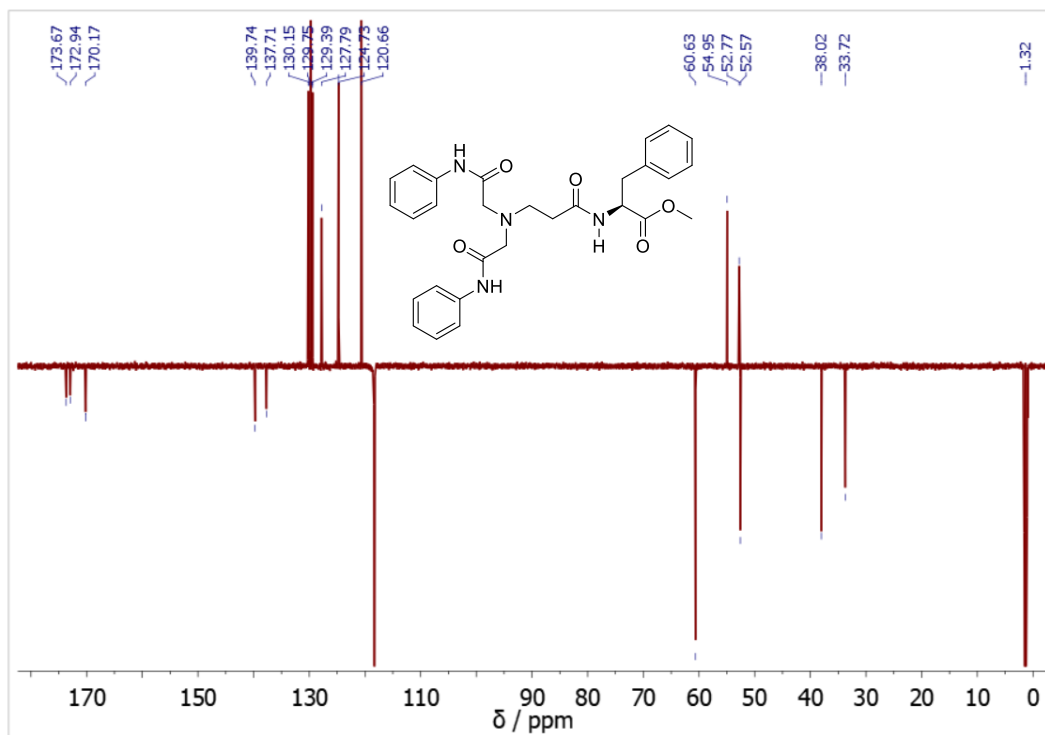


Figure S109. APT ¹³C NMR (150.90 MHz, CD₃CN) of **i2B**

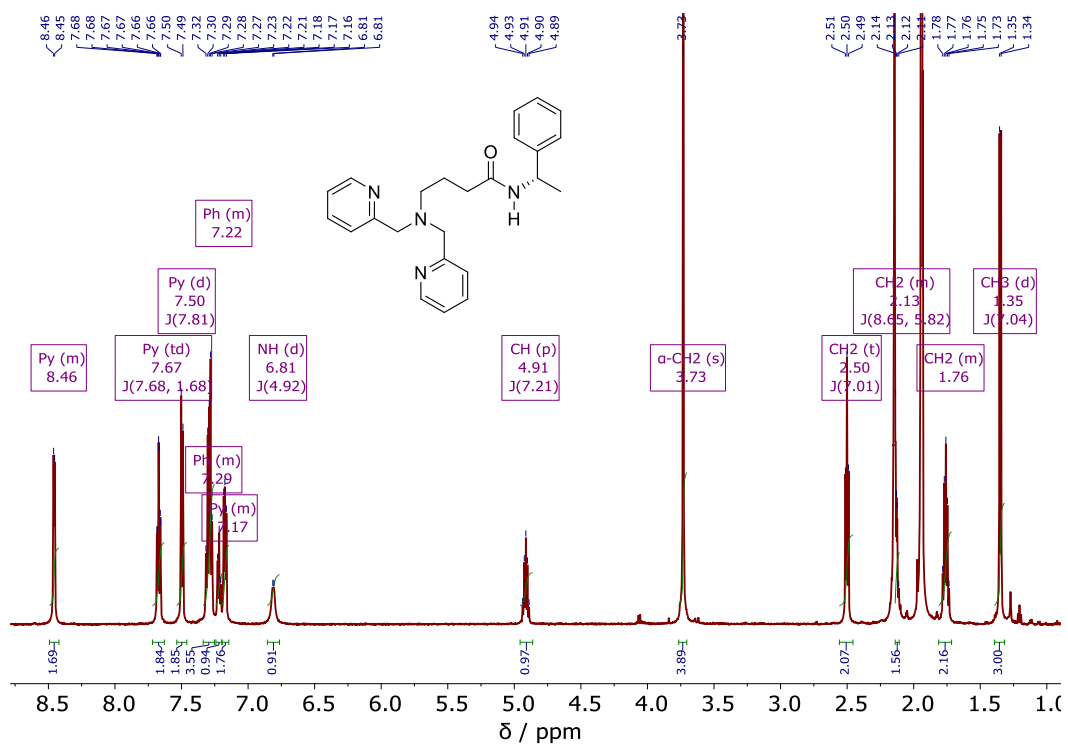


Figure S110. ^1H NMR (600.13 MHz, CD_3CN) of **b3A**

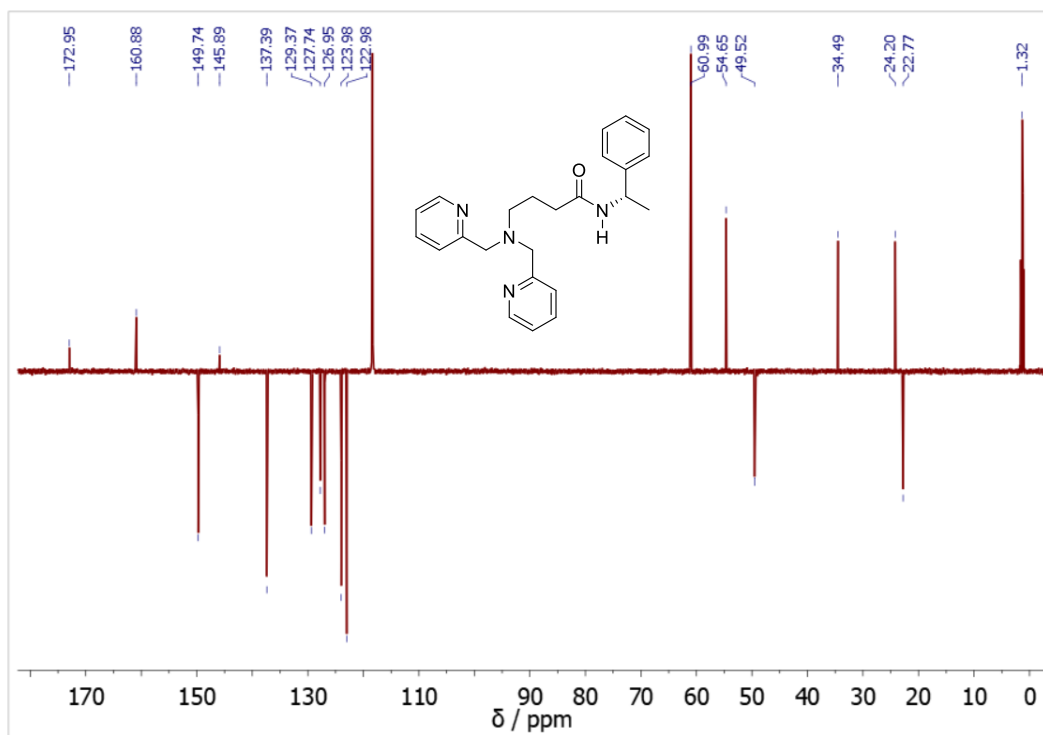


Figure S111. APT ^{13}C NMR (150.90 MHz, CD_3CN) of **b3A**

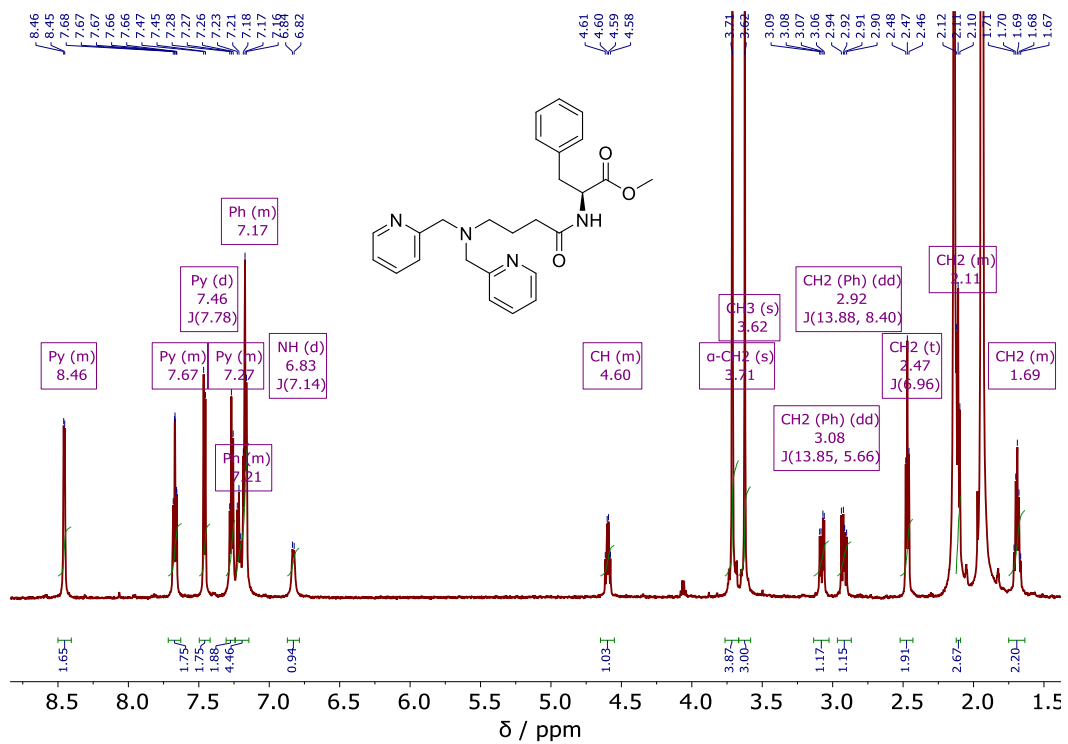


Figure S112. ^1H NMR (600.13 MHz, CD_3CN) of **b3B**

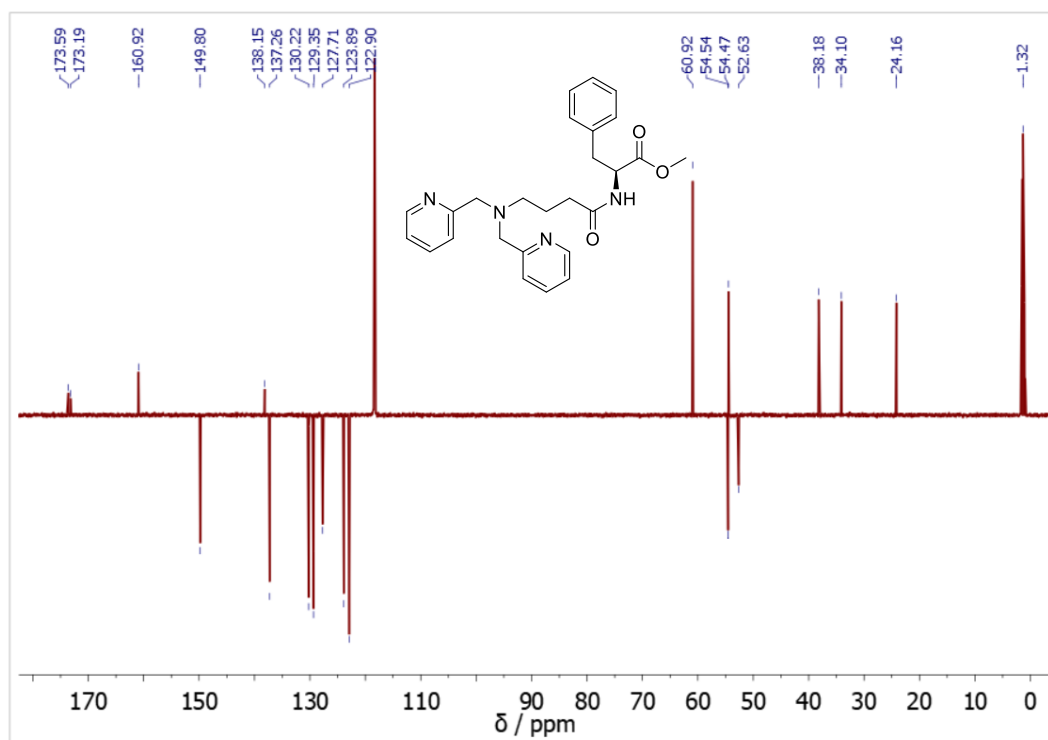


Figure S113. APT ^{13}C NMR (150.90 MHz, CD_3CN) of **b3B**

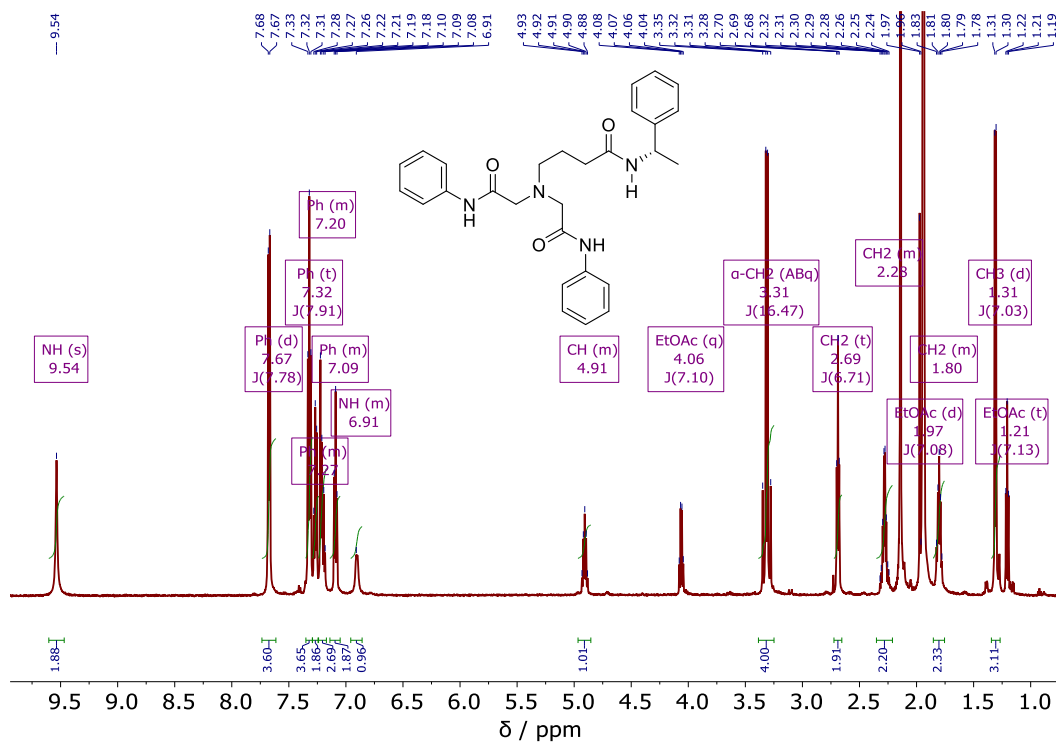


Figure S114. ¹H NMR (600.13 MHz, CD₃CN) of **i3A**

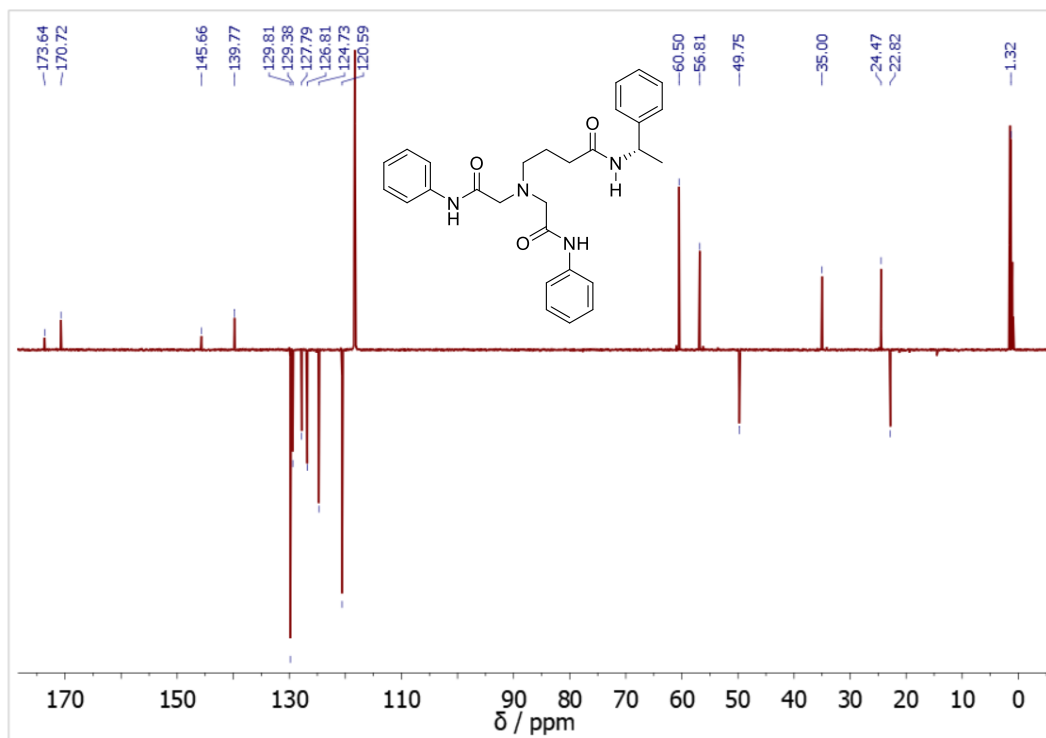


Figure S115. APT ¹³C NMR (150.90 MHz, CD₃CN) of **i3A**

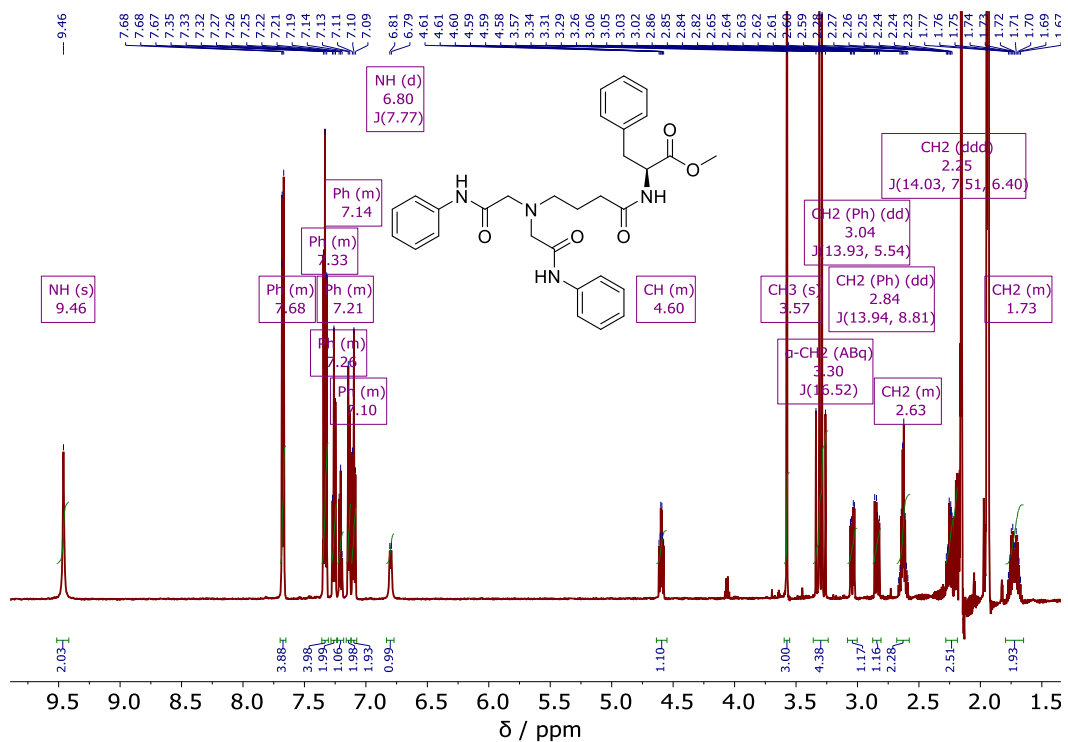


Figure S116. ¹H NMR (600.13 MHz, CD₃CN) of **i3B**

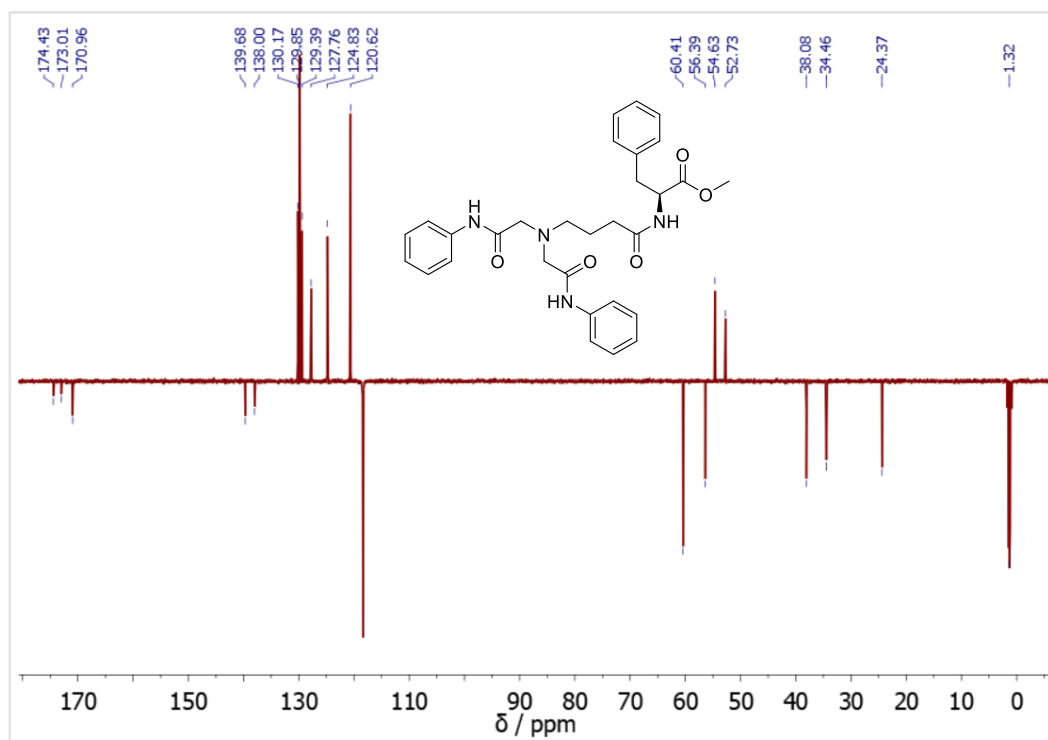


Figure S117. APT ¹³C NMR (150.90 MHz, CD₃CN) of **i3B**

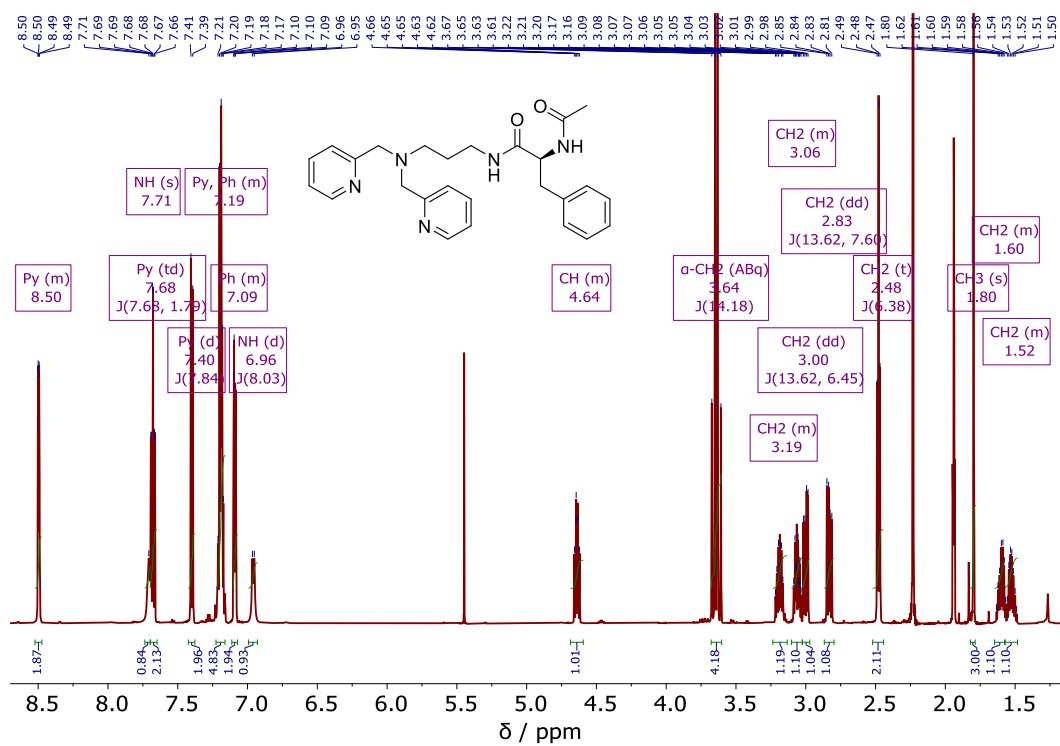


Figure S118. ¹H NMR (600.13 MHz, CD₃CN) of **b3C**

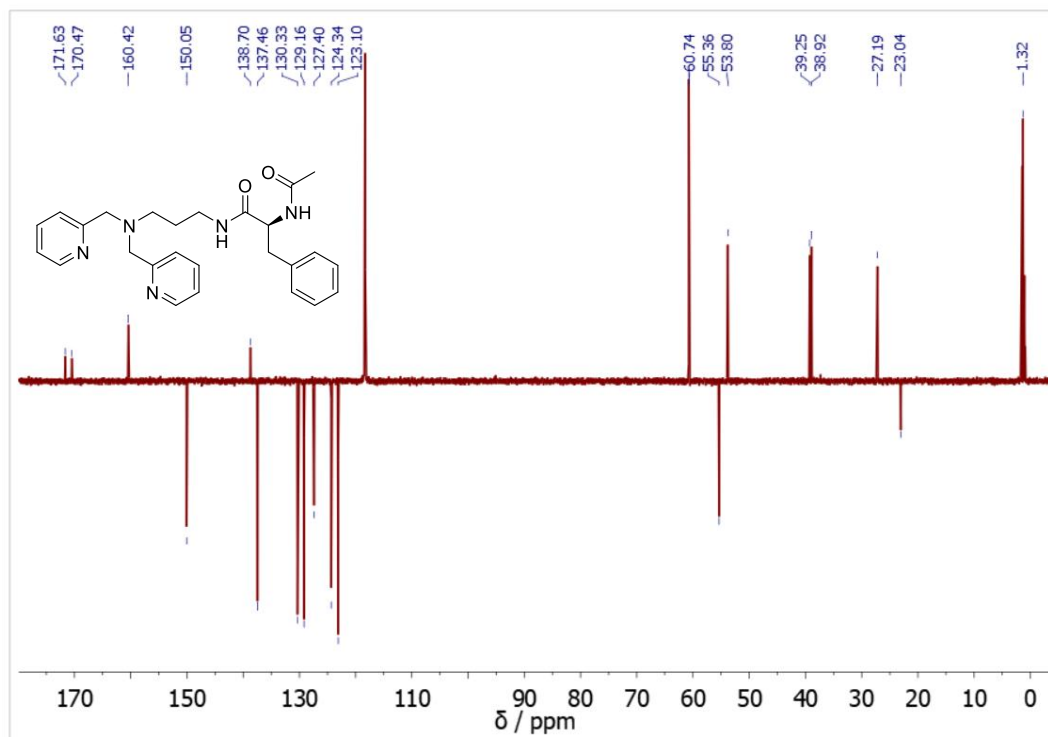


Figure S119. APT ¹³C NMR (150.90 MHz, CD₃CN) of **b3C**

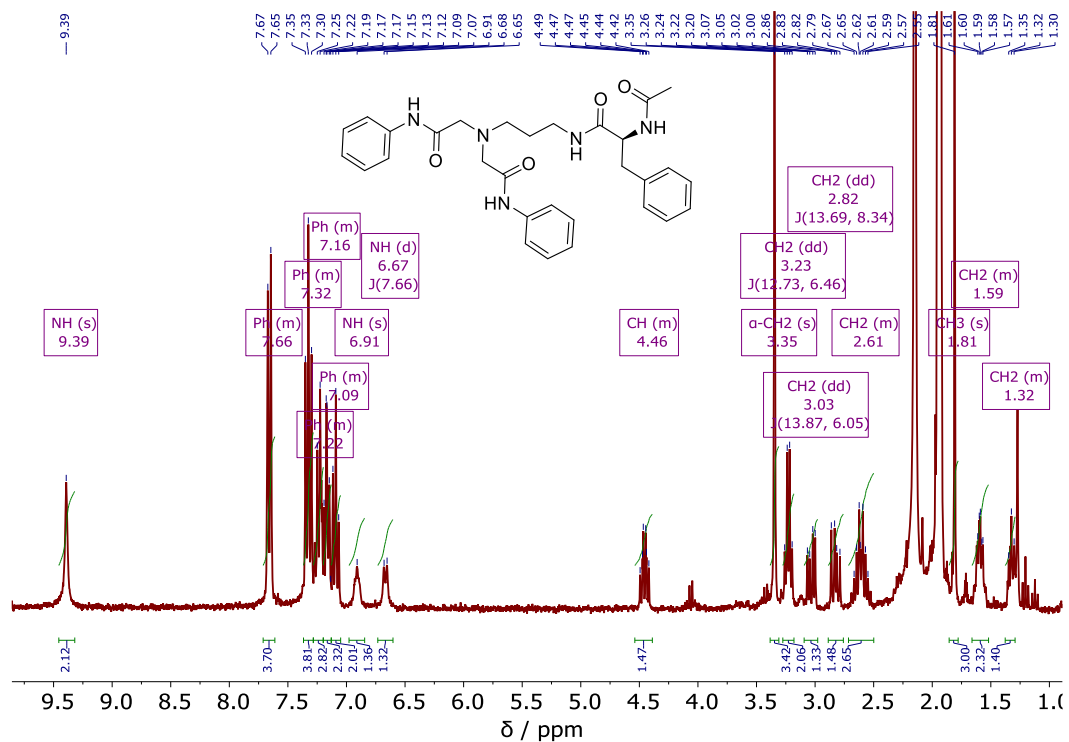


Figure S120. ¹H NMR (300.13 MHz, CD₃CN) of **i3C**

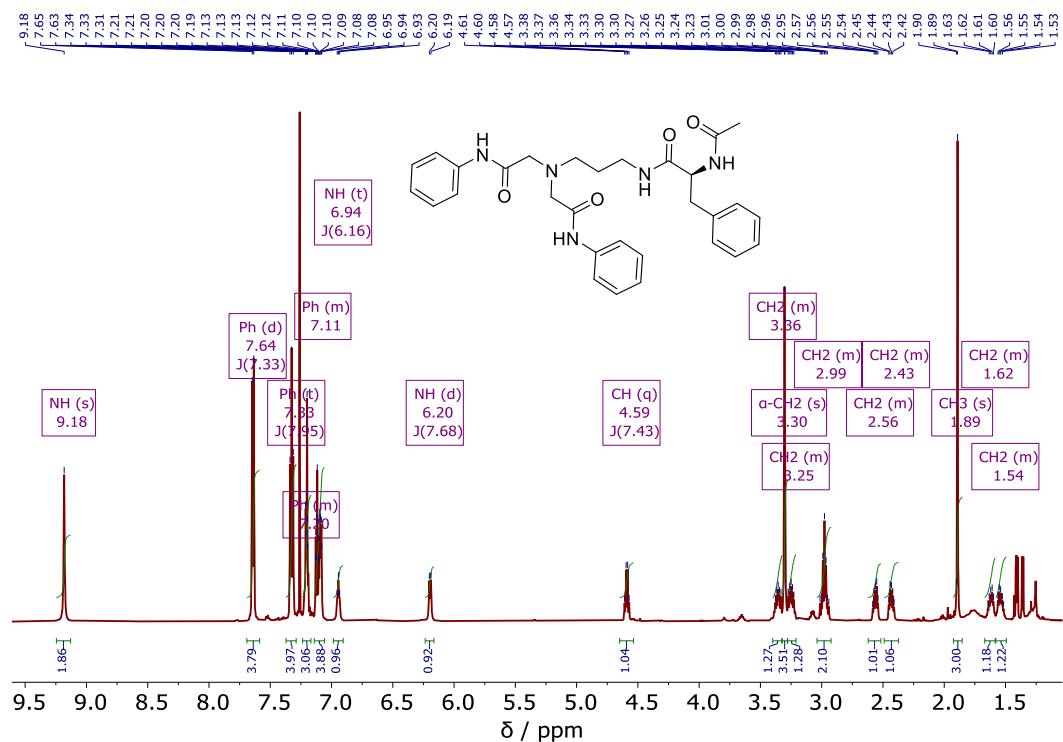


Figure S121. ¹H NMR (300.13 MHz, CDCl₃) of **i3C**

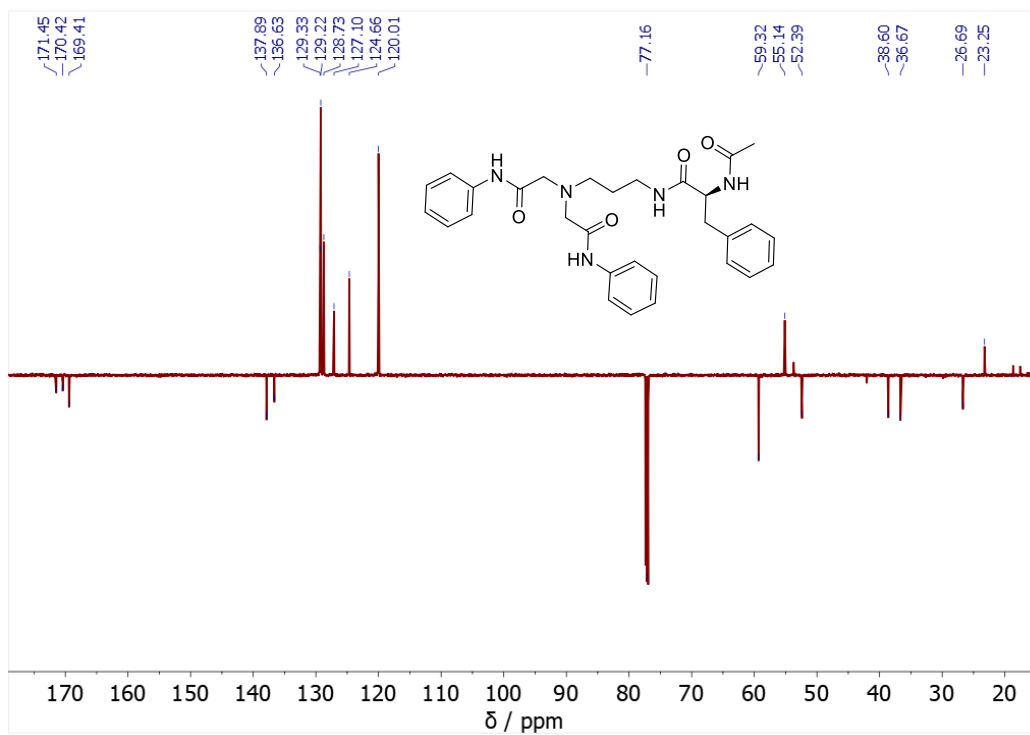


Figure S122. APT ¹³C NMR (600.13 MHz, CDCl₃) of **i3C**

12.3 ESI-MS spectra of ligands

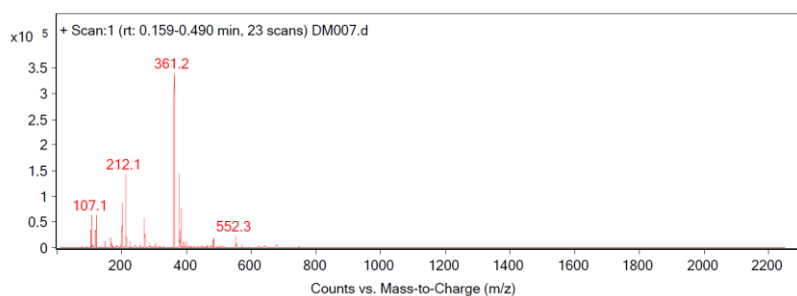


Figure S123. ESI-MS of **b1A**

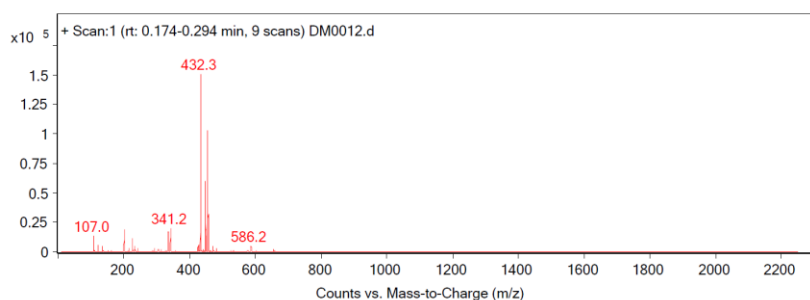


Figure S124. ESI-MS of **b2C**

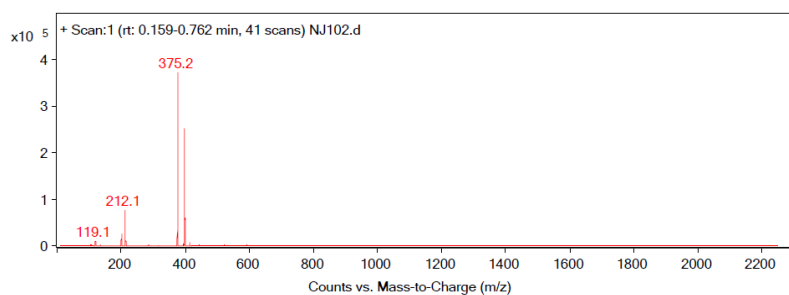


Figure S125. ESI-MS of **b2A**

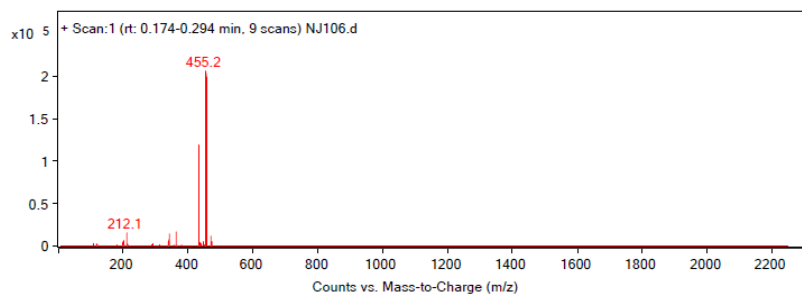


Figure S126. ESI-MS of **b2B**

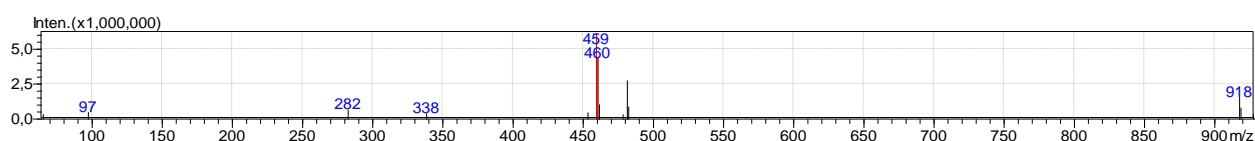


Figure S127. ESI-MS of **i2A**

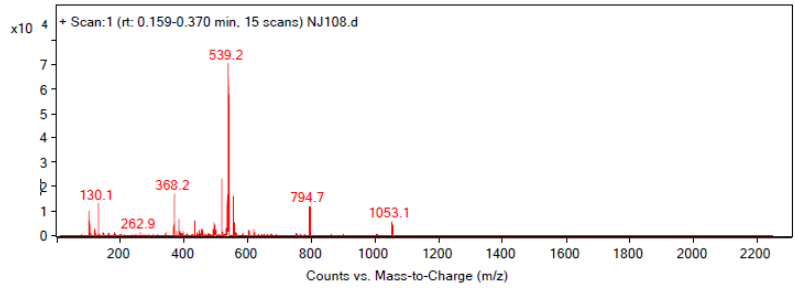


Figure S128. ESI-MS of **i2B**

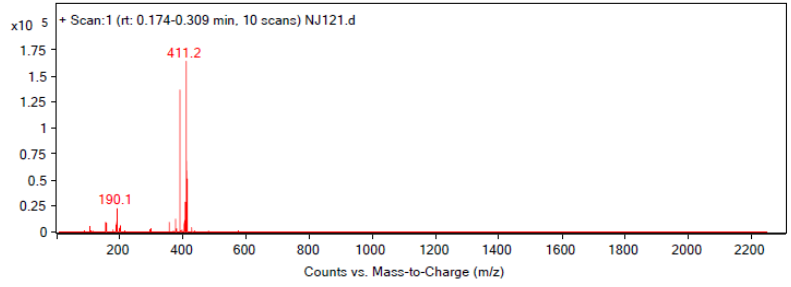


Figure S129. ESI-MS of **b3A**

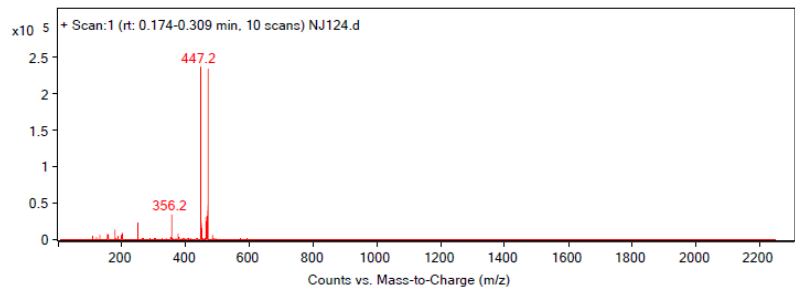


Figure S130. ESI-MS of **b3B**

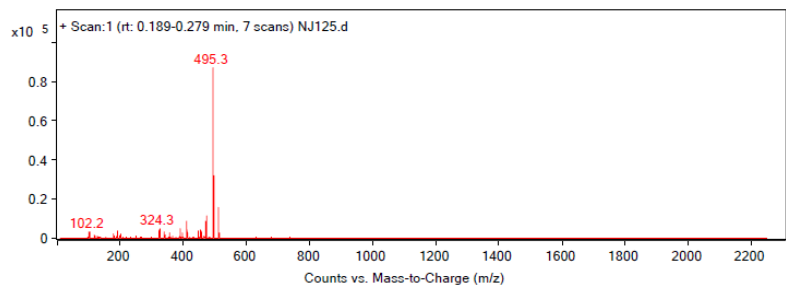


Figure S131. ESI-MS of **i3A**

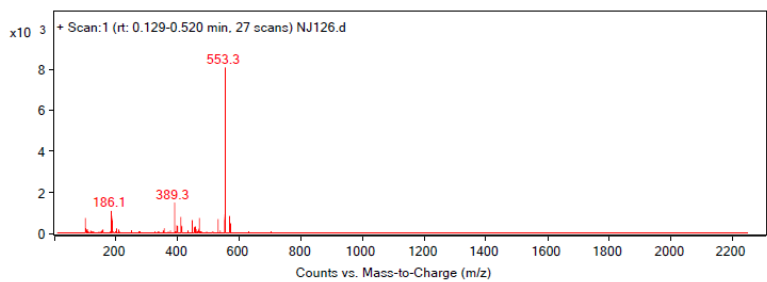


Figure S132. ESI-MS of **i3B**

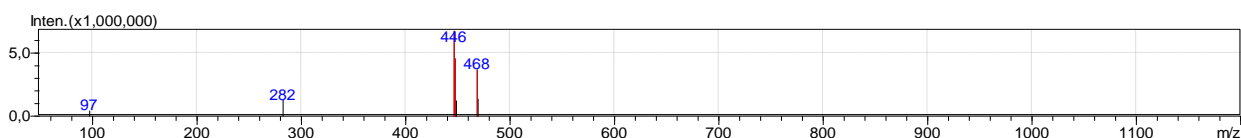


Figure S133. ESI-MS of **b3C**

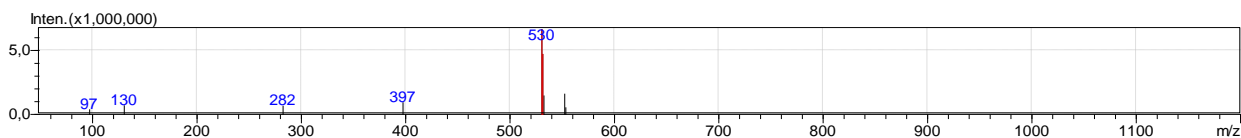


Figure S134. ESI-MS of **i3C**

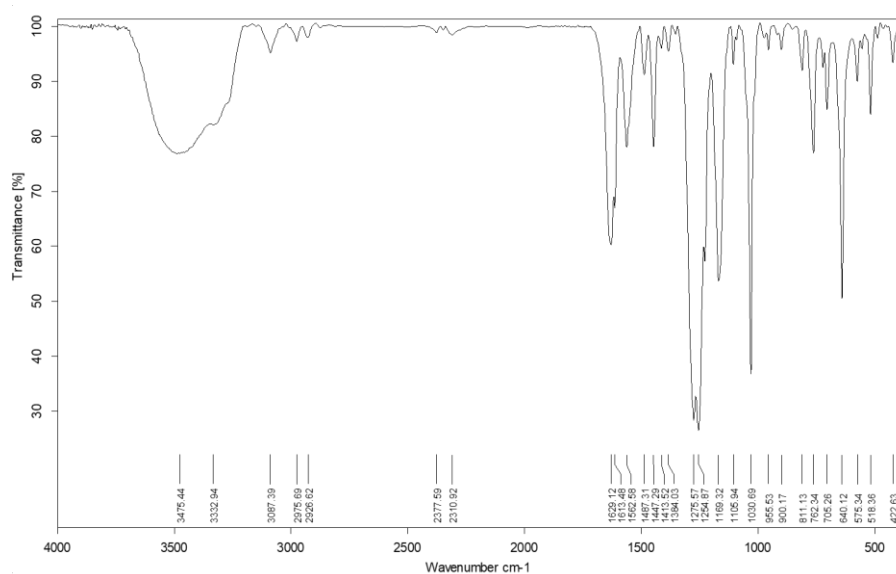


Figure S135. IR (KBr) spectrum of **b2A-Cu**

13 References

- 1 M. H. Abraham, R. J. Abraham, W. E. Acree, A. E. Aliev, A. J. Leo and W. L. Whaley, *J. Org. Chem.*, 2014, **79**, 11075–11083.
- 2 S. H. Gellman, G. P. Dado, G. B. Liang and B. R. Adams, *J. Am. Chem. Soc.*, 1991, **113**, 1164–1173.
- 3 Z. Kokan, B. Perić, M. Vazdar, Ž. Marinić, D. Vikić-Topić, E. Meštrović and S. I. Kirin, *Chem. Commun.*, 2017, **53**, 1945–1948.
- 4 B. H. Toby and R. B. Von Dreele, *J. Appl. Crystallogr.*, 2013, **46**, 544–549.
- 5 C. Andreini, G. Cavallaro and S. Lorenzini, *Bioinformatics*, 2012, **28**, 1658–1660.
- 6 A. C. Nielander, J. M. McEnaney, J. A. Schwalbe, J. G. Baker, S. J. Blair, L. Wang, J. G. Pelton, S. Z. Andersen, K. Enemark-Rasmussen, V. Čolić, S. Yang, S. F. Bent, M. Cargnello, J. Kibsgaard, P.

- C. K. Vesborg, I. Chorkendorff and T. F. Jaramillo, *ACS Catal.*, 2019, **9**, 5797–5802.
- 7 R. Diaz-Torres and S. Alvarez, *Dalton Trans.*, 2011, **40**, 10742–10750.
- 8 S. S. Massoud, C. C. Ledet, T. Junk, S. Bosch, P. Comba, R. Herchel, J. Hošek, Z. Trávníček, R. C. Fischer and F. A. Mautner, *Dalton Trans.*, 2016, **45**, 12933–12950.
- 9 A. Terenzi, C. Ducani, L. Male, G. Barone and M. J. Hannon, *Dalton Trans.*, 2013, **42**, 11220–11226.
- 10 S. S. Massoud, F. R. Louka, A. F. Tusa, N. E. Bordelon, R. C. Fischer, F. A. Mautner, J. Vančo, J. Hošek, Z. Dvořák and Z. Trávníček, *New J. Chem.*, 2019, **43**, 6186–6196.